DEVELOPMENT OF A MULTI-ELEMENT X-RAY EXCITATION PROBE FOR THE MEASUREMENT OF SPATIAL DISTRIBUTIONS OF ENERGETIC IONS, ATOMS, AND MOLECULES

BY
ANGELO M. FERRARI

A DISSERTATION PRESENTED TO THE GRADUATE SCHOOL
OF THE UNIVERSITY OF FLORIDA IN PARTIAL FULFILLMENT
OF THE REQUIREMENTS FOR THE DEGREE OF
DOCTOR OF PHILOSOPHY

UNIVERSITY OF FLORIDA

1991

Copyright 1991

By

Angelo M. Ferrari

To Raquel

ACKNOWLEDGMENTS

Many people have helped me with their wisdom, their encouragement, or their love to reach this stage in my academic and professional career. Among them are my teachers, my friends, and my dear family. It would be impossible for me to thank all of them individually without fear of leaving out someone that justly deserves to be included in the list. Therefore, I will limit myself to mentioning those who most recently and most directly have given me their support in the work related to this dissertation.

First, I acknowledge the interest that the members of my committee have shown in my work, in particular that of its chairman, Dr. Samim Anghaie. His constant support and almost unlimited availability for enlightening discussions have been key factors in my successful completion of this dissertation.

I have learned much from informal conversations with my fellow students. Two of them deserve special mention since they also helped me in the performance of many of the measurements required for this work: Robert Williams and Leo Bitteker. My sincere thanks go to them.

I am in debt to my old friends and colleagues Edward Fairstein, Peter Thieberger, and Sergio Pissanetzky for more reasons that I can possibly mention.

The love and patience of my wife Raquel and of my children, Lucia, Mario, and Pablo, kept me going at times when my energy seemed to evaporate.

I appreciate the financial support of the Electric Power Research Institute (EPRI) through a grant to the University of Florida. In particular, I thank Dr. David H. Worledge of the EPRI Nuclear Power Division for his vision in facilitating the support of the project of which this work is a part.

Finally, I also acknowledge the financial support of Drs. Donald Price and Thomas Walsh of the University of Florida Research Foundation and of the Division of Sponsored Research.

TABLE OF CONTENTS

Page

ACKNOWLEDGEMENTS iv

LIST OF TABLES ix

LIST OF FIGURES xii

ABSTRACT xvi

CHAPTERS

1 INTRODUCTION 1

2 MOTIVATION AND BACKGROUND 5

2.1 Motivation 6
2.1.1 The Self-Collider Fusion Reactor 6
2.1.2 Diagnostic Instrumentation Requirements of the SCFR 19
2.2 Background: Existing Methods of Particle Density Distribution Measurement 20
2.2.1 Beam-current Measurements 21
2.2.2 Secondary Emission Measurements 24
2.2.3 Other Methods of Particle Beam Characterization 25
2.2.4 Applicability of Existing Methods to the SCFR Diagnostic Requirements . . . 26

3 THE MULTI-ELEMENT X-RAY EXCITATION PROBE METHOD . 27

3.1 Operation of the Multi-Element X-ray Excitation Probe System 28
3.2 Targets for Use with the Multi-Element Probes 30
3.3 Applicability of the Method to the SCFR Diagnostic Needs 32
3.4 Other Applications for X-ray Excitation Probes 35

4 PRODUCTION AND DETECTION OF X-RAYS FROM TARGETS BOMBARDED BY ENERGETIC PARTICLES 37

4.1 Introduction 38
4.2 Stopping of Energetic Ions by Matter 38
4.3 Production of Characteristic X-rays 45

4.4 Absorption of X-rays in the Target Material . 61
4.5 Detection of X-rays 62
4.6 The Specific Detected Photon Yield 64

5 IMPLEMENTATION OF THE MULTI-ELEMENT PROBE METHOD 68

5.1 Construction and Assembly of Probes 70
  5.1.1 Laminiform Probes 70
  5.1.2 Filiform Probes 70
  5.1.3 Selection of Materials for Probe Construction 77
5.2 The X-ray Detector 77
  5.2.1 Non-Continuous Use 79
  5.2.2 Sufficient Resolution 80
  5.2.3 Reasonable Efficiency 82
  5.2.4 Physical Configuration 83
5.3 The Very Low Noise Preamplifier 85
5.4 The Linear Amplifier 97
  5.4.1 Amplification 98
  5.4.2 Pulse Shaping and Noise Filtering 101
  5.4.3 Pole-Zero Cancellation 111
  5.4.4 Baseline Restoration 112
5.5 The Multi-Channel Pulse-Height Analyzer . . . 114
  5.5.1 Determination of the Required MCA Specifications 117
  5.5.2 Specifications of the Selected Analyzer 121
5.6 System Integration 121

6 MEASUREMENT OF SPATIAL PARTICLE DISTRIBUTIONS USING THE MULTI-ELEMENT X-RAY EXCITATION PROBE . 124

6.1 Calibration Facility 126
  6.1.1 The Van de Graaff Accelerator and the Beam Line Used in the Measurements . . . 126
  6.1.2 Energy and Current Calibration of the Van de Graaff Accelerator 131
6.2 Calibration of the X-ray Spectrometer 162
6.3 Calibration of X-ray Excitation Probes 164
  6.3.1 General Method of Probe Calibration . . . 166
  6.3.2 Calibration of Probes with Laminiform Targets 174
  6.3.3 Calibration of Probes with Filiform Targets 175
  6.3.4 Calibration of Probes Using Partially Ionized Beams 194
6.4 Measurements of Beam Profiles and Position Using Multi-Element X-ray Excitation Probes . 195
6.5 Measurement of Beams Neutralized with Carbon Foils 196

7 CALCULATION OF SPECIFIC DETECTED PHOTON YIELDS . . 207

7.1 Calculation of the Specific Detected Photon Yield for Targets Bombarded with Protons in the Energy Range from 0.5 to 2.5 MeV 208
7.1.1 Calculation of Y_{sd} for Thick Laminiform Targets 208
7.1.2 Calculation of Y_{sd} for Filiform Targets . 215
7.2 Calculation of Specific Detected Photon Yields for Thin Gold Wires Excited by High-Energy Protons 223

8 CONCLUSIONS 225

APPENDICES

A FABRICATION OF THIN SEAMLESS ALUMINUM WINDOWS . . . 230

B SPECIFICATIONS AND CALIBRATION CERTIFICATE OF THE K485 CURRENT METER 249

C DATALOG FORM 252

D APPLICATION OF X-RAY PROBES TO SCFR MEASUREMENTS 254

REFERENCES 258

BIOGRAPHICAL SKETCH 265

LIST OF TABLES

4-1 X-ray production cross sections for protons in tungsten, calculated with Equation 4-4 58

5-1 Target materials used in the laminiform probes . . 73

5-2 Reduced list of metals suitable as targets in x-ray excitation probes 78

6-1 Resonances in the $^{27}Al(p,\gamma)^{28}Si$ Reaction (between 800 and 1200 keV) 137

6-2 Energy levels of ^{28}Si 139

6-3 Data for the determination of k at the 922.6 keV resonance 143

6-4 Data for the determination of k at the 937.2 keV resonance 144

6-5 Data for the determination of k at the 991.88 kev resonance 145

6-6 Data for the determination of k at the 1025.0 keV resonance 145

6-7 Data for the determination of k at the 1118.4 keV resonance 146

6-8 Summary of the determinations of k and calculation of the average value 152

6-9 Calibration of the K261 current source 159

6-10 Main energy peaks of the calibration sources . . . 161

6-11 Switching magnet settings for north line 169

6-12 Charge-to-protons conversion factors 173

6-13 Measurements of Y_{sd} for laminiform Nb targets (K-series) 176

6-14 Measurements of Y_{sd} for laminiform Mo targets (K-series) 177

6-15 Measurements of Y_{sd} for laminiform Pd targets (K-series) 178

6-16 Measurements of Y_{sd} for laminiform Ta targets (L-series) 179

6-17 Measurements of Y_{sd} for laminiform W targets (L-series) 180

6-18 Interpolated values of Y_{sd} for laminiform targets (K-series) 181

6-19 Interpolated values of Y_{sd} for laminiform targets (L-series) 182

6-20 Materials and sizes of wires used in filiform probes 184

6-21 Correction factors for current-integrator readings for 2.5 MeV protons striking Mo and Pt wire targets at 45° 187

6-22 Measurements of Y_{sd} for filiform (d = 127 μm) Mo targets (K-series) 188

6-23 Measurements of Y_{sd} for filiform (d = 127 μm) Pd targets (K-series) 189

6-24 Measurements of Y_{sd} for filiform (d = 127 μm) W targets (L-series) 189

6-25 Measurements of Y_{sd} for filiform (d = 127 μm) Au targets (L-series) 189

6-26 Interpolated values of Y_{sd} for filiform (d = 127 μm) targets (K-series) 190

6-27 Interpolated values of Y_{sd} for filiform (d = 127 μm) targets (L-series) 191

6-28 Measurements of Y_{sd} for filiform Mo targets at E_o = 2.5 MeV (K-series) 193

6-29 Measurements of Y_{sd} for filiform Pt targets at E_o = 2.5 MeV (L-series) 193

6-30 Principal x-ray lines of the target materials used in the measurement of beam profiles . . . 195

7-1 Normalized target penetration (t/R) vs. normalized proton energy (E/E_o) 212

7-2 Depth intervals and proton energies used in Equation 7-2 214

7-3 Interpolation multipliers 215

A-1 Percent transmission of photons by beryllium . . 232

A-2 Percent transmission of photons by aluminum . . 233

A-3 Percent transmission of photons by Mylar 237

LIST OF FIGURES

Page

2-1 Examples of exoergic nuclear reactions which could be produced with colliding beams 7

2-2 Approximate diagram of the field lines of the superconducting magnets used in the SCFR 9

2-3 Complete array of the superconducting magnets used in the SCFR and approximate diagram of the field lines 10

2-4 Representation of the trajectories of the particles in the SCFR showing the focusing effects of the axial and radial field components 11

2-5 Particle density as a function of the radial distance 12

2-6 SCFR concept with direct energy conversion system 13

2-7 Methods of particle injection in the SCFR 17

3-1 Illustration of the principle of operation of the multi-element x-ray excitation method . . 29

4-1 Stopping and range of protons in tungsten 42

4-2 Energy loss of a proton beam with initial energy E_o = 1 MeV as it penetrates a thick tungsten target, graphed from data of Andersen and Ziegler. Curve is a fifth order polynomial fit. Vertical segments are standard deviations calculated with Bohr's formula . . 44

4-3 Characteristic x-ray nomenclature 49

4-4 Examples of characteristic x-ray spectra 50

4-5 K-series x-ray production cross sections computed with Reuter's formula and Reid's program 53

4-6 L-series x-ray cross sections plotted from published data 54

4-7 Energy distribution of protons of initial energy E_o = 1 MeV vs. average energy <E(t)>, as they penetrate a thick tungsten target. The areas under the curves are equal 56

4-8 Geometry for Equation 4-13 66

5-1 Longitudinal section of test chamber showing target holder 71

5-2 Aperture-type holder 72

5-3 Fork-type holder 74

5-4 Jig for assembling filiform probes 75

5-5 Definition of resolution 81

5-6 High-purity germanium detector 86

5-7 Charge-sensitive preamplifier 90

5-8 Pulsed optical feedback charge-sensitive preamplifier 95

5-9 Differentiating network 106

5-10 Integrating network 107

5-11 System block diagram 122

6-1 Simplified diagram of the experimental beam line 128

6-2 Diagram of the target-detector geometry 132

6-3 Experimental arrangement for energy calibration of the Van de Graaff accelerator 138

6-4 Gamma-ray spectrum of ^{28}Si acquired with a 5-inch x 5-inch NaI(Tl) detector. The horizontal scale (energy) ranges from 0 to approximately 14 MeV. The vertical scale (counts) is logarithmic . 140

6-5 Correspondence between steps in the gamma-count graph with resonances in the ^{27}Al(p,γ)^{28}Si reaction 142

6-6 Determination of k at the 922.6 keV resonance . 147

6-7 Determination of k at the 937.2 keV resonance . 148

6-8 Determination of k at the 991.88 keV resonance . 149

6-9 Determination of k at the 1025.0 keV resonance . 150

6-10 Determination of k at the 1118.4 keV resonance . 151

6-11 Block diagram of the K261 current source 156

6-12 Illustration of the virtual ground type of current-measuring instrument 157

6-13 Photon energy spectrum of calibration source . . 163

6-14 Typical spectrometer calibration graph 165

6-15 Specific detected photon yields of laminiform targets 183

6-16 Correction factor for tilted wires 186

6-17 Specific detected photon yields of filiform targets of 0.127 mm diameter 192

6-18 Measurement of beam profile (I) (beam direction: into the page) 197

6-19 Measurement of beam profile (II) (beam direction: into the page) 198

6-20 Measurement of beam profile (III) (beam direction: into the page) 199

6-21 Measurement of beam profile (IV) (beam direction: into the page) 200

6-22 Measurement of beam profile (V) (beam direction: into the page) 201

6-23 Measurement of beam profile (VI) (beam direction: into the page) 202

7-1 Illustration of the method used to determine the values of Δt_i used in Equation 7-2 210

7-2 Universal graph of proton energy vs. target penetration 213

7-3 Specific detected photon yields for thick laminiform targets 216

7-4 Geometry for filiform targets 218

7-5 Specific detected photon yields (K-series) for 0.127 mm filiform targets 220

7-6 Specific detected photon yields (L-series) for 0.127 mm filiform targets 221

7-7 Specific detected photon yield as a function of wire diameter 222

7-8 Specific detected photon yield and energy loss vs. energy for 0.001 mm gold wires bombarded with high-energy protons 224

A-1 Construction of 0.004" Mylar windows 235

A-2 Setup for pressure-testing of Mylar windows . . 236

A-3 Exploded view of Mylar window modified with aluminum disc 239

A-4 Fabrication of aluminum blanks 240

A-5 Jig for machining thin aluminum windows (material: cold rolled steel) 241

A-6 Alignment of the jig 243

A-7 Mounting the blank on the jig 245

A-8 Measuring the baseline with the depth gauge before beginning the cutting operation 246

A-9 Window cutting operation 247

B-1 Specifications of the K485 current meter 250

B-2 Calibration certificate of the K485 current meter 251

C-1 Datalog form 253

Abstract of Dissertation Presented to the Graduate School
of the University of Florida in Partial Fulfillment of the
Requirements for the Degree of Doctor of Philosophy

DEVELOPMENT OF A MULTI-ELEMENT X-RAY EXCITATION PROBE FOR THE MEASUREMENT OF SPATIAL DISTRIBUTIONS OF ENERGETIC IONS, ATOMS, AND MOLECULES

By

Angelo M. Ferrari

December, 1991

Chairman: Dr. Samim Anghaie
Major Department: Nuclear Engineering Sciences

The multi-element x-ray excitation probe is a new device to measure spatial distributions of energetic particle fields such as ions, atoms, and molecules using the characteristic x-ray spectra of multi-element targets to determine location of the point of measurement, and the intensity of the spectral lines to determine the particle flux. The probe consists of several thin wires or other small targets of different elements mounted on a supporting frame. The probe is placed in the field of energetic particles which interact with the atoms of the targets, causing the emission of characteristic x-rays. The radiation produced by the targets is detected in a high-purity germanium detector located in the vicinity of the probe. The signals generated by the detector are processed and stored in a computer-based x-ray spectrometer. The high

resolution inherent to this instrument provides x-ray spectra with sharply defined lines which are used to identify the element which generated them and, therefore, their location of origin. Because in the case of particle-excited targets the production of characteristic x-rays is directly proportional to the number of particles that directly interact with the wire, the integral of the characteristic x-ray spectrum is a direct measurement of the particle flux at the given location. In this manner, if the location of the different targets is known with respect to a given frame of reference, and the probes have been calibrated with beams of known intensities, the information provided by the characteristic x-ray spectrum can be directly reduced to the quantity of interest: particle flux vs. location.

Multi-element x-ray excitation probes have a potentially wide range of applications, from the characterization of particle accelerator beams to the determination of densities in fields of energetic particles with quasi-stationary orbits.

Some of the probes built to perform the proof-of-principle experiments have been used to measure proton beam profiles with resolutions of approximately 10 μm and to detect less than 10^5 protons per square millimeter per second.

A theoretical model is developed which describes the basic principles of operation of the probe (characteristic x-ray production). This theoretical model is based on well-established theories of interaction of energetic particles with matter. This allows a priori calculations of the expected results, at least within one order of magnitude for absolute values and within substantially narrower limits for relative measurements.

CHAPTER 1
INTRODUCTION

The multi-element x-ray excitation probe is an instrument used in the measurement of spatial distributions of energetic particles such as ions, atoms, and molecules. The probe consists of an array of targets of several elements (usually, but not necessarily, in the form of thin metallic wires arranged in a parallel configuration) placed in the field of energetic particles whose spatial distribution is to be measured. The particles that strike the targets excite its atoms and these, in turn, emit characteristic x-rays. A high-resolution photon spectrometry system records their spectrum. The location of the emission is determined by the characteristic spectrum and the number of particles striking each target by the intensity of the x-ray lines. By calibration of the probes in controlled experimental conditions it is possible to establish a quantitative relationship between position and particle flux.

One important feature of the multi-element x-ray excitation probe method is that it is based on well-established principles of low-energy photon spectrometry used in a novel manner.

In the past, high resolution x-ray spectrometry has been used mainly in the field of elemental analysis. In this application, the quantities to be measured are the amounts or concentrations of the elemental constituents of a sample. The sample is excited with photons or charged particles, and the energy spectrum emitted by the sample yields the desired information. In contrast, in the method developed in the present work the composition of the sample (probe) is well known, and the obtained x-ray spectrum is used to characterize the particle-beam used in the excitation.

Another important aspect of the new method is that it is applicable not only to measurements involving particle-beams discussed in Chapters 2 and 3, but also to the determination of particle distributions of other ordered energetic particle systems described in Chapter 2, such as the Self-Collider Fusion Reactor (SCFR) under development at the University of Florida.

A third significant feature of the method is the possibility of building probes that are essentially transparent to the beam. This is particularly true for highly energetic particle beams, as discussed in Chapter 7.

Finally, the potential for its application to the measurement of multi-dimensional particle distributions is mentioned in Chapter 8.

The material presented here is organized as follows:

In Chapter 2, the diagnostic needs of the SCFR, which were the original motivating force for the development of the x-ray excitation probe, are discussed. To place these diagnostic needs in their proper context, a description of the SCFR precedes them. Also in Chapter 2, a review of existing methods for particle distribution methods is included. This review highlights the desirability for a novel approach in the case of the SCFR experiments.

In Chapter 3, the multi-element x-ray excitation method and its applicability to the SCFR diagnostic requirements are described in detail. This leads to the discussion of other potential applications of the newly developed probe to other experimental situations, such as characterization of accelerator beams, particle-beam optics, neutral particle beams, etc.

In Chapter 4, a study of the interaction of energetic particles with matter and the production of characteristic x-rays is presented. This is done with the purpose of arriving at the definition of the concept of specific detected photon yield Y^{sd}, which is later used in the calculation of particle density distributions from the information contained in the characteristic x-ray spectra of the probes. Some of the expressions derived in this chapter are also used in Chapter 7 for the calculation of Y_{sd} in those cases in which the probes cannot be calibrated experimentally.

In Chapter 5, the physical implementation of the multi-element x-ray excitation system is presented. The fabrication of the probes is described, and the specifications of the x-ray spectrometer necessary to perform the measurements are discussed.

In Chapter 6, a presentation of the experimental work performed for the development, calibration, and application of the multi-element x-ray excitation probes is made. This includes a description of the experimental facility used in the measurements, the calibration procedure of the Van de Graaff accelerator, the calibration of probes using totally and partially ionized beams, measurements of proton beam profiles, and measurements of neutralized particle beams.

In Chapter 7, the concept of specific detected photon yield developed in Chapter 4 is applied to the calibration of probes. Calculations are shown for targets that were previously used in Chapter 6 and for targets that could not be calibrated experimentally.

In Chapter 8, the general conclusions derived from this development work are presented, and possible new areas for further development of the method are mentioned.

CHAPTER 2
MOTIVATION AND BACKGROUND

In several areas of experimental particle physics, atomic and molecular beam studies, accelerator design, and applied accelerator technology, it is necessary or desirable to know the particle flux distribution over a given area or in a given volume. The need for new methods and systems to measure such distributions is discussed later in this chapter when existing methods are reviewed. However, a few applications can be mentioned at this time to illustrate this need. For instance, the map of particle flux over the cross section of an accelerator or microprobe beam can be used in the design and adjustment of particle optics systems. Also, measurements of distribution of atomic and molecular beams are useful in the study of neutralization methods. Other situations in which the quantitative knowledge of particle flux distribution is advantageous are diagnostic applications in some nuclear fusion experiments involving colliding beams. The diagnostic requirements of one of such experimental fusion projects,[1] the University of Florida Self-Collider Fusion Reactor (SCFR) [1,2], motivated the development of the method and system presented here. In the first part of this chapter, the SCFR and its diagnostic needs are discussed. In the second part, existing methods of particle distribution measurement are described.

---

[1] In this work, the word fusion indicates any of several exoergic nuclear reactions.

2.1 Motivation

2.1.1 The Self-Collider Fusion Reactor

The SCFR is a beam-confinement fusion system currently under development at the University of Florida. In this system, fusionable particles injected by an electrostatic accelerator into a reaction chamber describe rosette-shaped trajectories that are contained within a bi-concave thin disk under the influence of strong axially and radially focusing magnetic fields. The purpose of this arrangement is to create a high density of particles moving in colliding trajectories within a small volume near the center of the distribution. This situation establishes a favorable environment for the occurrence of fusion reactions such as (d,d), (d,t), (d,^{3}He), and (p,^{11}B) (Figure 2-1). To coerce the particles into the desired trajectories, it is necessary to realize a magnetic field with the following characteristics:

1. It must have cylindrical geometry (the axis of symmetry is called the z-axis).
2. It must increase from nearly zero at the z-axis to a high intensity near the periphery.

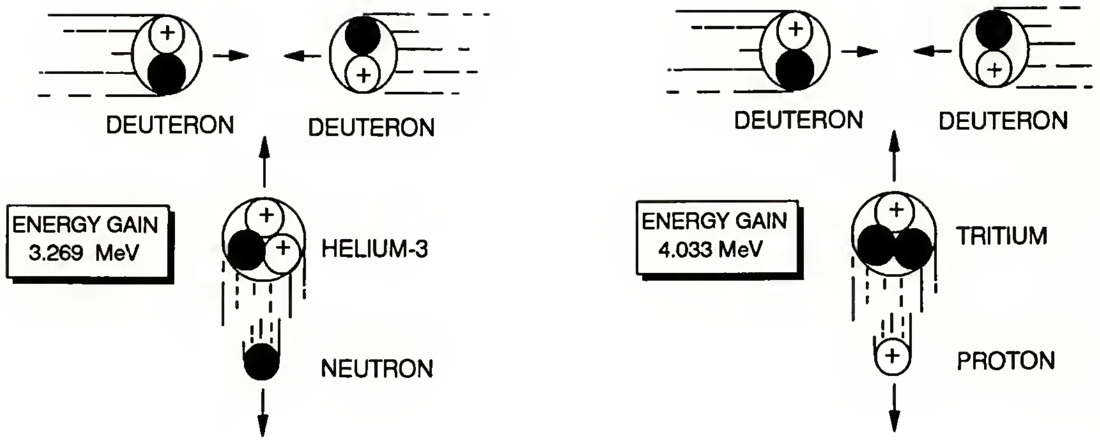

a. $^2H + ^2H \rightarrow ^3He + n$

b. $^2H + ^2H \rightarrow ^3H + p$

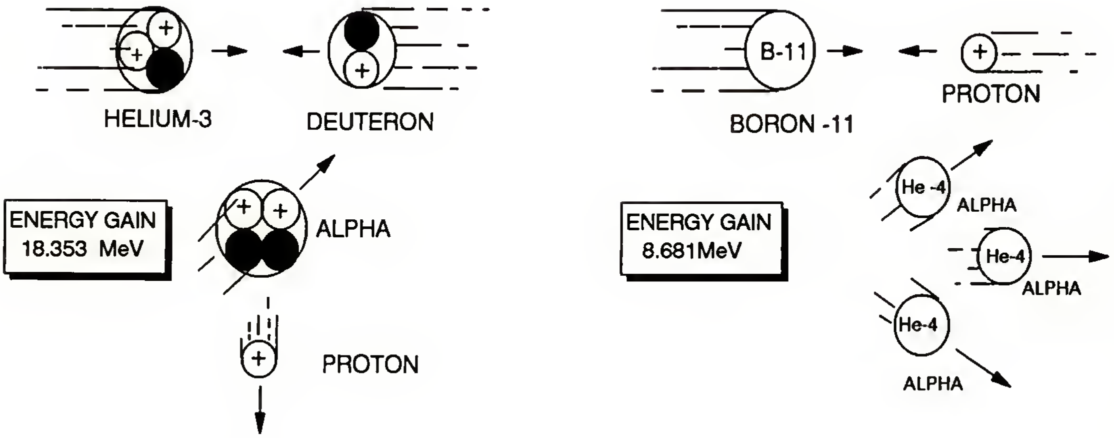

c. $^3He + ^2H \rightarrow \alpha + p$

d. $^{11}B + p \rightarrow 3\alpha$

Figure 2-1. Examples of exoergic nuclear reactions which could be produced with colliding beams

3. Also, it must have a small radial component near the periphery.

Figures 2-2 and 2-3 show the building up of this field configuration by using superconducting solenoid arrays, and Figure 2-4 illustrates the approximate shapes of the trajectories. Attention is called to the fact that, as shown in Figure 2-3, the combination of the three superconducting solenoids creates a magnetic field with a radial as well as an axial component near the periphery of the reaction chamber. This radial component is necessary for axial focusing of the trajectories.

Computer simulations have been performed to determine the shape of the self-colliding trajectories, and, based on those simulations, calculations of the particle density distribution and of the probability of the occurrence of fusion reactions have been carried out [3]. The particle density distribution calculations show that the concentration of particles will vary as $1/r_2$, where r is the distance from the point of intersection of the trajectories (Figure 2-5); and the results of calculations of the probability of fusion calculations indicate that it should be possible to realize a system with positive energy balance. A number of fusion reactions are possible candidates for the proposed system, and some of those being considered are shown in Figure 2-1. One of the most attractive is the $(p,{}^{11}B)$ reaction which yields three alpha

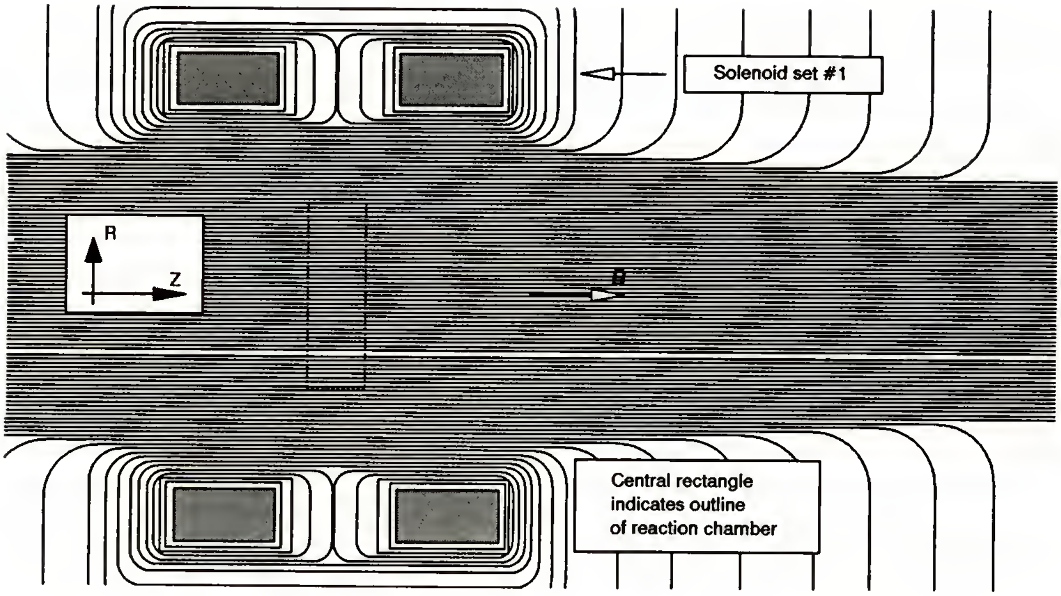

a. Fiel of solenoid set #1 only

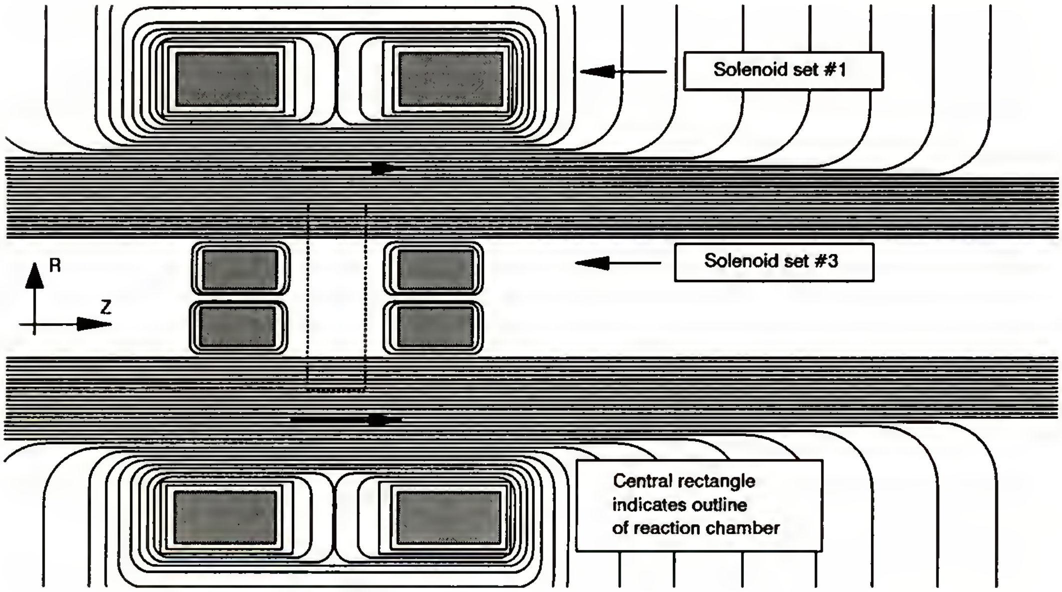

b. Resultant field of solenoids #1 and #3

Figure 2-2. Approximate diagram of the field lines of the superconducting magnets used in the SCFR

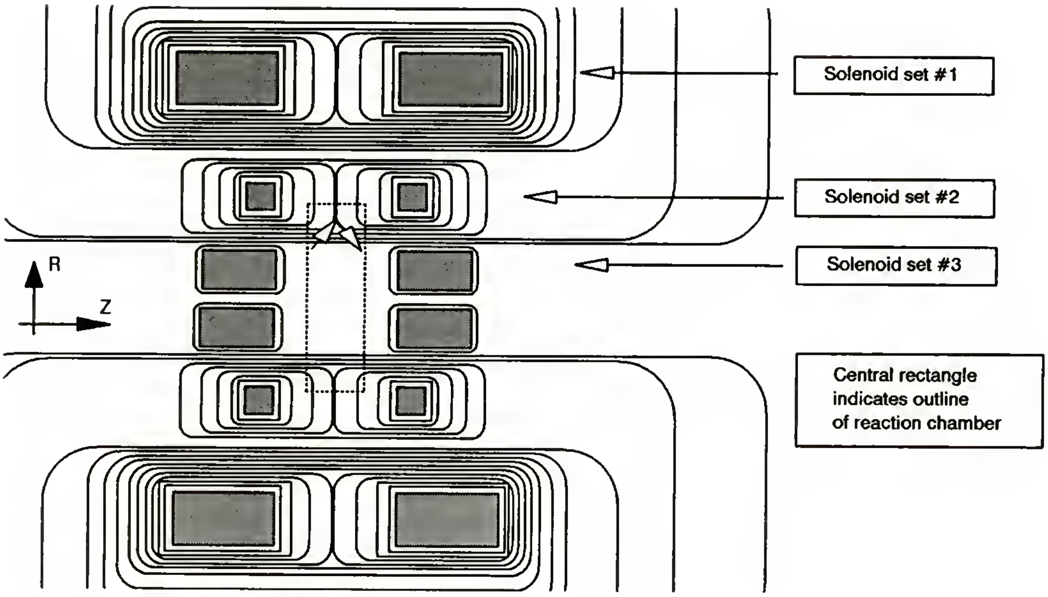

Figure 2-3. Complete array of the superconducting magnets used in the SCFR and approximate diagram of the field lines

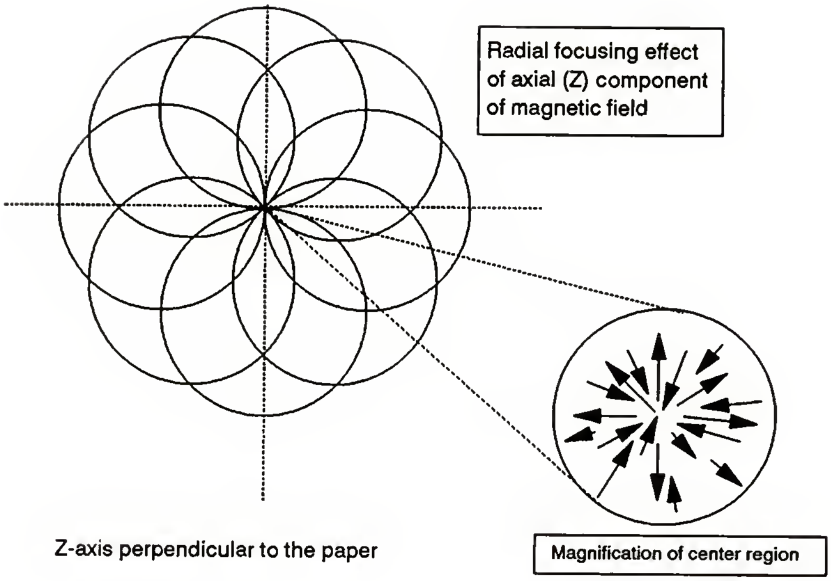
Radial focusing effect of axial (Z) component of magnetic field
Z-axis perpendicular to the paper
Magnification of center region

a. View on the radial plane

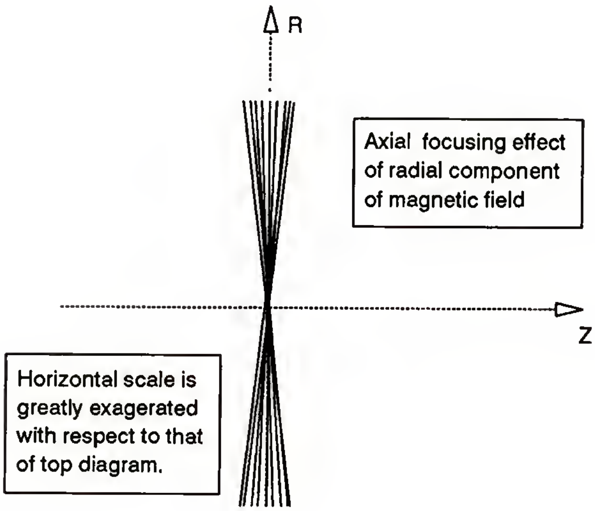
R
Axial focusing effect of radial component of magnetic field
Z
Horizontal scale is greatly exagerated with respect to that of top diagram.

b. View on a plane through the z-axis

Figure 2-4. Representation of the trajectories of the particles in the SCFR showing the focusing effects of the axial and radial field components

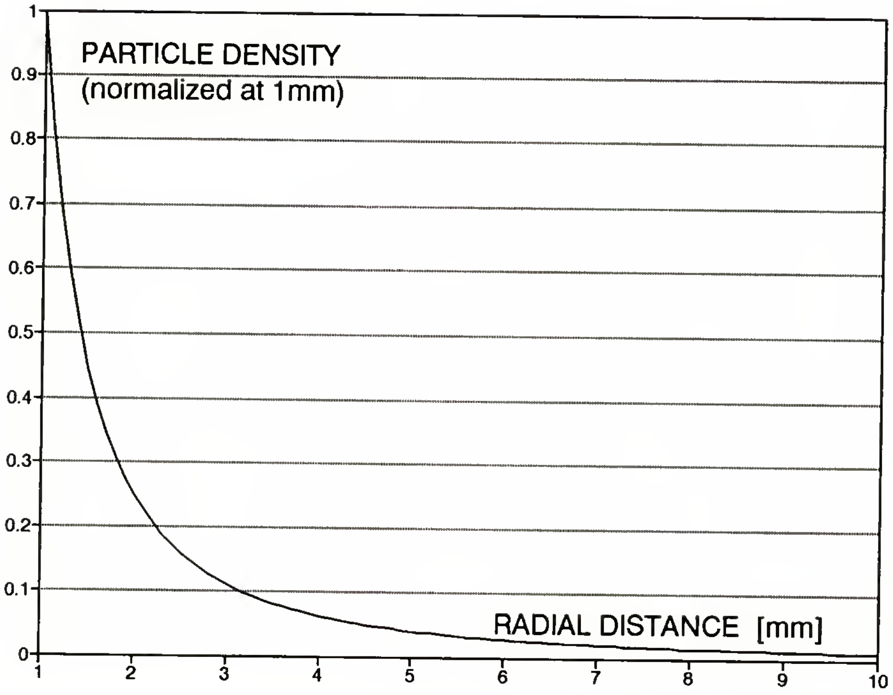

Figure 2-5. Particle density as a function of the radial distance

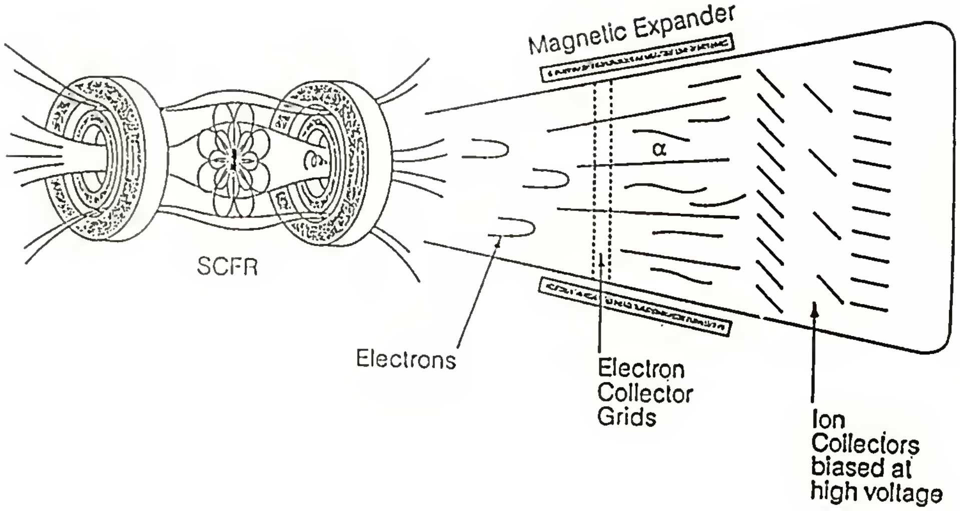

Figure 2-6. SCFR concept with direct energy conversion system

particles, a net energy gain of 8681 keV per reaction, has a cross section of almost one barn at 650 keV (energy of protons striking a stationary ^{11}B target), and is completely aneutronic.

Whatever the reaction selected, the charged fusion products will leave the reaction chamber spiraling around the z-axis, under the influence of the axial magnetic field. Figure 2-6 shows a simplified diagram of a kinetic-to-electric direct conversion scheme which has been proposed to extract power from the system without any intermediate thermal conversion stage.

The SCFR differs significantly from proposed generators based on the production of energy by the fusion of randomly colliding particles in a confined thermonuclear plasma. In those systems it is necessary to reach a critical state (ignition) of temperature and pressure at which a sufficiently high fusion rate is attained to generate the energy necessary to maintain the conditions of criticality. At that point the reactor continues to operate without further addition of external energy. In this conventional mode of operation it is necessary to prevent the extinction of the reaction. This is accomplished by appropriate design. On the other hand, in the SCFR there is neither criticality nor ignition. In principle, the reactor can operate at any power level as long as energetic particles continue to be injected into the reaction chamber in sufficient quantities.

A fraction of these particles will undergo fusion and generate energy. As mentioned before, it is theoretically possible to design a system that will generate more energy than it consumes. In this sense, the SCFR is an energy amplifier rather than a generator.

In summary, the SCFR has the advantages of being inherently stable (no energy output unless there is some energy input), of scaling very well (a relatively small system should be substantially as efficient as a much larger one), and, by the proper selection of fusionable particles, of being essentially aneutronic.

Three distinct subsystems can be identified in the SCFR: particle injection, particle fusion, and energy extraction. The particle injection subsystem consists of the particle accelerators, the beam optics, and the components specifically required for injecting the beams of fusionable particles into the reaction chamber. The particle fusion subsystem consists of the reaction chamber itself and of the superconducting magnets necessary to create the desired magnetic field configuration. The energy extraction system consists of the means for collecting the energetic particles generated in the fusion reactions, the system for converting the kinetic energy of these particles into usable electrical energy, and, in some cases, the subsystem for breeding new fusionable particles.

One of the first engineering problems that must be solved in the SCFR is the difficulty of injecting charged particles at the center of a magnetic field configuration such as the one previously described. Direct injection is not realizable because the charged particles would be deflected by the strong magnetic field in the annular region close to the periphery of the reaction chamber and would not be able to describe the desired quasi-stationary trajectories. Two solutions are proposed for this problem: One is off-center injection, the other is beam neutralization.

The first method consists in directing the beam of charged particles off-center so that the magnetic field bends it into an orbit that passes through the geometric center of the reaction chamber (Figure 2-7a). By design, the magnetic field keeps the particle in this center-intersecting trajectory. The beam neutralization method consists in converting the charged particles into neutral species (atoms or molecules) before injecting them directly into the center of the reaction chamber, and then providing means of reionizing them within the volume of acceptance for quasi-stationary orbits (Figure 2-7b). In principle, off-center injection is the most desirable method because of its simplicity and efficiency (theoretically, all the particles in the beam can be directed to the center). However, experimental constraints sometimes preclude the use of this method, and beam neutralization becomes the only available option. In the early stages of the SCFR project,

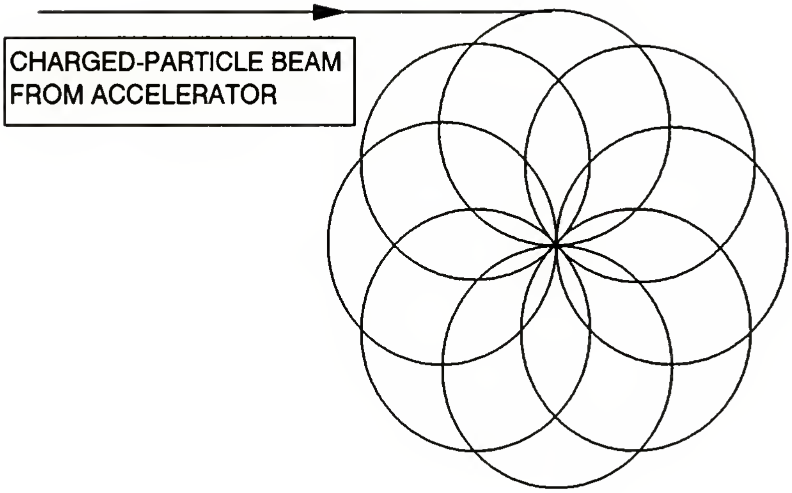

a. Off-center injection

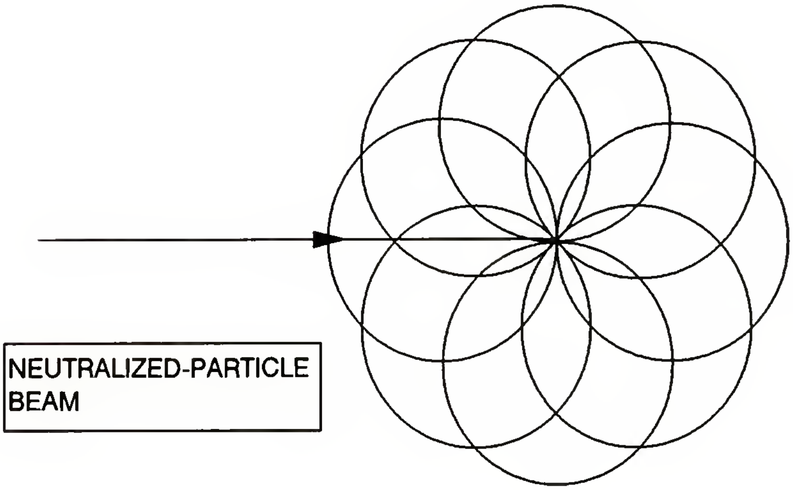

b. Neutral beam injection

Figure 2-7. Methods of particle injection in the SCFR

it will be necessary to use an existing superconducting magnet system previously designed for other applications. There are restrictions in the access to the central space of this magnet in its present form that make it impossible to inject a beam at the necessary distance from the center to achieve off-center injection. Modification of the magnet to allow for off-center injection is one of the options currently being considered, but beam neutralization remains a distinct possibility [4].

In the first series of proof-of-principle experiments, protons will be used as the orbiting particles to test the magnetic field configuration. If the method of beam neutralization is used, a beam of neutral hydrogen atoms will be obtained by directing an H_2^+ beam through a thin carbon film. By interacting with the carbon lattice, some of the H_2^+ ions will be dissociated into H^+ ions and H atoms. These ions, as well as the remnant H_2^+ ions, will be deflected from the beam with a sweeping magnet, and the H atoms will proceed to the center of the reaction chamber. Some of the H atoms will be ionized through collisions with existing electrons as they travel through the reaction chamber; a few of them will become ions at, or very near, the center of the chamber. These ions will be trapped by the magnetic field and will describe the quasi-stationary orbits. The atoms that are not ionized, or that are ionized at other locations within the chamber, will be lost. Once the process of ionization begins, a gradual buildup will take place because of the preferential ionizations in the center. Eventually, the system reaches a steady state in which the charge density at the center remains constant. This is because the number of particles that are injected equals the number of particles that undergo fusion reactions or that are lost through mechanisms discussed in Reference 2. The particle fusion subsystem consists of a reaction chamber and the superconducting magnets that provide the field necessary to maintain the particles in the center-intersecting quasi-stationary trajectories.

The first stage of the SCFR experimental program is aimed at verifying the computer predictions of spatial particle-density distributions within the reaction chamber. These measurements are expected to yield valuable information necessary for the design on the magnetic field configuration and methods of particle injection to be used in subsequent stages of the project.

2.1.2 Diagnostic Instrumentation Requirements of the SCFR

In the different phases of the SCFR project (proof-of-principle, prototype design and testing, optimization of fusion rate, extraction of energy, and optimization of energy production), it will be necessary to perform measurements of a number of system variables. In the early stages, some of these measurements will be the verification of the magnetic field configuration and of the existence of quasi-stationary orbits, the measurement of particle flux distribution, the verification of the existence of fusion reactions, and the measurement of fusion products. In particular, during the proof-of-principle experiments the following diagnostic needs must be addressed:

1. Measurement of beam profiles and mapping of accelerator beam cross section to optimize particle beam optics to achieve a beam sharply focused at the center of the reaction chamber.
2. Measurement of the efficiency of the neutralization system to optimize its performance.
3. Measurement of the efficiency of the reionizing process in the reaction chamber.
4. Measurement of the charged-particle flux distribution in the reaction chamber.

These diagnostic needs require instrumentation capable of measuring beams before and after neutralization and probes that are minimally intrusive in the reaction chamber. The method for the measurement of spatial particle distributions that has been developed and that is presented here was motivated by these diagnostic needs and addresses all of these requirements.

2.2 Background: Existing Methods of Particle Density Distribution Measurement

The existing methods of particle density distribution measurements may be divided into two broad categories: plasma diagnostics and particle-beam diagnostics. Systems for plasma diagnostics will not be discussed here because they are not directly related to the subject matter of this work. On the other hand, a description of current methods for particle-beam diagnostics highlights the needs for novel approaches to this measurement problem and provides the background necessary for the discussion of the method developed in this work.

Several techniques are or have been used for the characterization of particle-beams in accelerators, microprobes, and colliding-beam systems. These include beam current, secondary emissions, particle backscattering, and induced charge measurement methods. Typical devices used in the implementation of these methods are described below.

2.2.1 Beam-current Measurements

Probably the most common method of determining particle-beam intensity and profile consists in measuring the current from beam-intercepting electrodes [4-13]. These will be generically referred to as current probes.

The systems based on this method are usually implemented with single- or dual-wire probes moved across the beam to obtain one- or two-dimensional profiles in a sequence of measurements [5-13]. Also, stationary two-dimensional wire arrays have been used [14]. Some of the most representative systems based on current probes described in the literature are discussed below.

Nielsen and Skilbird designed a beam-profiling instrument which had two 0.2 mm-thick tungsten wires (needles) at 90°, separately driven by oscillators. The needles scanned the beam at approximately 25 cps in either direction [13]. Currents down to the level of 10^{-9} A were measured with this system. This is equivalent to approximately 10^{10} singly charged ions per second.

Takacs devised a simple single-wire scanner system that had the ability of scanning the beam sequentially in two orthogonal directions [12]. The wire was bent at 90° and attached by its vertex at the tip of a rod of much greater length than the diameter of the beam cross section; the sides of the right angle formed by the wire were positioned at 45° with respect to the axis of the rod. The probe was placed on the beam path with the plane formed by the bent wire normal to the beam. The rod was driven back and forth on the wire plane causing both sides of the angle formed by the wire to intercept the beam on each complete cycle. The position of the probe was determined by a piezo-electric transducer. The current for each position of the probe was recorded, and the beam profile was reconstructed from these values.

Hortig built a single-electrode probe that consisted of a wire mounted at 45° with respect to the axis of a drive motor [11]. In one revolution the wire scanned the beam cross section in two directions. Also here, a two-dimensional mapping of the cross section was obtained from the acquired information.

Variations and improvements of these methods have been implemented by Stensgaard and Korbjerg [5], Meier and

Richter [6], Duport and Jaccard [7], Bond and Gordon [8], Wegner and Figenbaum [9], and Jagger, Page and Riley [10], among others.

Stover and Fowler have constructed probes in the form of orthogonal arrays of 16 x 16 wires, each wire connected to a current-measuring amplifier [14]. The plane of the array is placed perpendicular to the beam axis. Two-dimensional profiles are obtained with the probe at a fixed position.

In general, no great amount of information is given in the literature about the lower limit of detection of the wire probes. It appears that the probes were constructed for operation in relatively high intensity beams where the main concern was to protect the wires from being destroyed by heating rather than to measure extremely low particle flux. It is reasonable to assume, however, that the sensitivity of the probes will be limited by the capabilities of state-of-the-art of current-measuring instruments, by the noise introduced by insulator leakage, by particles of spurious origin striking the wire, and by the time available for the measurement.

All of the current probes require that the charged particles be fully stopped by the electrode(s). Therefore, no matter what the energy of the beam, the particles that contribute to the measurement are permanently removed from the beam.

2.2.2 Secondary Emissions Measurements

Another approach to particle beam characterization is to measure the secondary emissions from targets that intercept the beam partially or totally. Some of the techniques found in the literature are described below.

Martin and Goloskie have used a probe to measure aberrations of quadrupole lenses designed to focus 600 keV protons [15]. The probe consisted of a tungsten wire inserted in the beam path. The measured quantity was the charge of the backscattered protons.

Field described measurements of the beam sizes of the Stanford Linear Collider using the bremstrahlung from carbon filament probes [16].

Struve, Chambers, Lauer, and Slaughter have also implemented bremstrahlung probes. In their case, the targets were tantalum rods and tungsten powder [17].

A method for profiling proton beams by measuring the K_α radiation from copper deposited on an iron wire has been described by Jenson, Hill, and Mangenson [18].

Bosser et al. have constructed probes with thin carbon fibers that are scanned across the beam to obtain a one-dimensional profile of protons and anti-protons. Secondary particle emissions from the filaments are detected and counted by scintillator-photomultiplier tube assemblies, and the number of counts is used as a measurement of the beam intensity at the chord intercepted by the probe [19].

Odom et al. [20] have used thin film and grid probes to map beam cross sections by obtaining an image of it from the secondary emissions focused by charged-particle optics.

2.2.3 Other Methods of Particle Beam Characterization

A commonly used method of characterizing pulsed-accelerator beams is to measure the current transient created by the induced charge as the burst of particles passes between electrodes (stripline pick-ups). This method has been most recently discussed by Ross [21], by Kuske et al. [22], and by Webber et al. [23]. Electrostatic pick-up yields information on beam intensity and beam position.

In the case of electron beams, it is also possible to measure the synchrotron radiation if the beam is bent by magnetic fields. Kuske et al. [22] and Coombes and Neet [24] have made use of this method.

Images of beams' cross-sections can also be obtained by intercepting them with charge-coupled devices (CCD), as described by Beavis et al. [25], or with scintillation screens with or without shadowing grids, or with filament arrays [21, 24, 26, and 27].

Coombes and Neet have measured the emissions of the interactions of particles with Çerenkov cells to monitor linear accelerator beams [24].

In colliding beam systems, it is possible to derive some information about them from the bremstrahlung emitted at the point of collision [21].

2.2.4 Applicability of Existing Methods to the SCFR Diagnostic Requirements

Some of the existing methods could meet some of the diagnostic needs of the SCFR. For instance, several of the techniques described above could be used to adjust the particle optics system necessary to produce a beam spot of the required size at the center of the quasi-stationary orbits. Also, some of the instrumentation just discussed could be used to perform measurements in the neutral beams used in one of the SCFR methods of injection. However, the measurement of particle density distribution inside the reaction chamber poses particular challenges, such as the need for minimal interference with the orbiting particles and the desirability of performing simultaneous measurements at different locations, that are not easily met with the existing devices. As an example, the possibility of using thin wires at various points within the chamber to implement the current-measuring method does not appear feasible because the allowable wire size (of the order of 1 μm in diameter) would be smaller than the range of the energetic particles, and no charge would be deposited on the probes.

Therefore, a new method of charge particle distribution measurement that has potential advantages for some of the SCFR measurements, and that also may be applicable to other experimental situations, has been developed and is introduced in the next chapter.

CHAPTER 3
THE MULTI-ELEMENT X-RAY EXCITATION PROBE METHOD

The operation of the multi-element x-ray excitation probes for the measurement of spatial distributions of energetic ions, atoms, and molecules developed in this work is based on the one-to-one correlation existing between elements and their characteristic x-ray spectra as a means of obtaining position and particle flux information simultaneously from several locations within the distribution [28].

Targets bombarded by energetic particles, or excited by electromagnetic radiation, emit the characteristic x-ray spectra of their constituent elements. It follows that single-element targets such as pure-metals emit the characteristic spectrum of that element only. Also, the intensity of a spectrum is directly proportional to the number of particles or photons that excite the target. Therefore, if different pure-element targets are placed at various locations within a field of excitation agents, the energy of the generated x-ray lines yields information on their place of origin, and their intensity on the intensity of the excitation.

The production and detection of x-rays will be analyzed in the next chapter. Here, the general manner in which single- and multi-element probes can be used in experimental situations will be discussed, and the features that make them potentially applicable to measurements such as those required in the SCFR will be described.

3.1 Operation of the Multi-element X-ray Excitation Probe System

The principle of operation of the system briefly described above will be illustrated with a hypothetical example.

A beam of particles, such as the one shown in Figure 3-1 has a certain cross section, and the number of particles per unit area passing by two points within this cross section during an interval t is to be determined. For the purposes of this discussion, it will be assumed that the two points are at distances d_1 and d_2 from a reference axis. The application of the multi-element x-ray excitation probe method to this experimental situation is shown below.

Two targets in the form of small disks of equal cross-sectional area a made of the pure elements E_1 and E_2 are placed at the desired locations. The targets, excited by the particles, emit their characteristic x-ray spectra which are accumulated for the interval t. Assuming that the x-ray spectrometer has been properly calibrated in terms of energy, the spectral lines corresponding to each of the

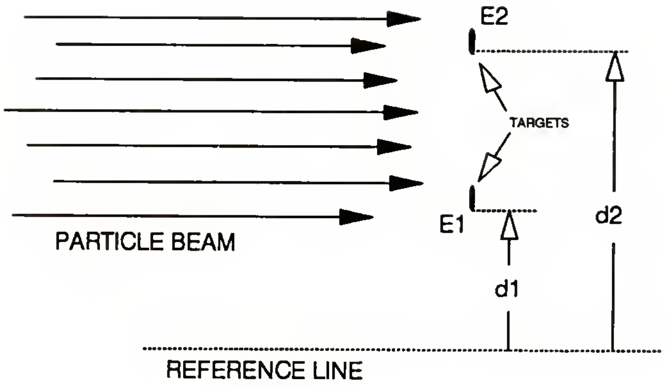

a. Location of the targets with respect to the beam

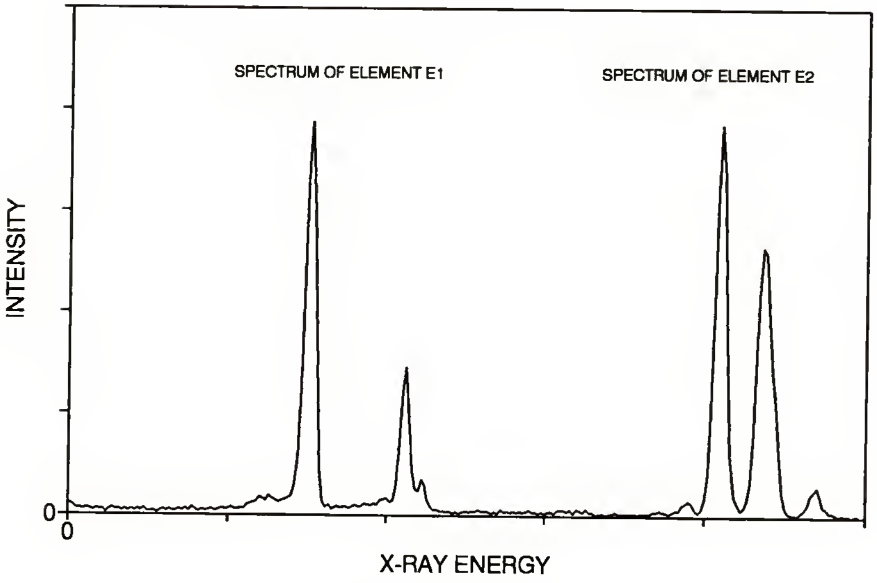

b. Characteristic x-ray spectra of the pure elements E_1 and E_2

Figure 3-1. Illustration of the principle of operation of the multi-element x-ray excitation method

targets are identified and the counts under the peaks of the respective spectra are integrated. Again, assuming that the targets have been calibrated according to the procedure to be discussed in Chapter 6, the number of particles intercepted by each of the disks is computed. Therefore, at the conclusion of the measurement it has been determined that the intensity of the beam is n_1 and n_2 particles per unit time per unit area at the distances d_1 and d_2, respectively, from the reference line. Simultaneous measurement of beam intensity at a larger number of locations only requires the use of a larger number of targets.

3.2 Targets for Use with the Multi-element Probes

In principle, there is no limit to the shapes and sizes of the targets that can be used with the multi-element x-ray excitation probes. In practice, the characteristics of the targets are dictated by the requirement of the measurement, the compatibility of the materials with the experimental environment, the availability of the pure materials in the required forms and sizes, and the feasibility of fabricating them to the required specifications.

In the experimental part of this work, only metallic targets in the form of foils and wires have been used, but there are several other possibilities. Some of these are mentioned below.

1. Small metallic disks attached to wires of a different metal. The support wire must have an x-ray spectrum that doesn't interfere with the spectra of the disks. For instance, iron wires (principal x-ray lines below 7 keV) could be used to support niobium, molybdenum, rhodium, palladium, silver, and cadmium disks (all elements with principal lines above 16 keV). Bonding techniques used in the semiconductor industry could be applied to the fabrication of the probes.
2. Alternately, short sections of the supporting wire could be electroplated with other metals.
3. If the target materials can be attached to the substrate by vacuum deposition, low-Z supports such as fused silica or carbon fibers could be used. In this case, the choice of target elements widens to include some of the metals with atomic numbers below 40 (Ti, V, Cr, Mn, Fe, Co, Ni, Cu, and Zn) which still have x-ray spectra with energies sufficiently high (>4.5 keV) to make possible the use of windowless detectors (see Chapter 5).
4. Disposable probes in the form of silicon chips with a mosaic (or other suitable pattern) of different elements could be mass produced with semiconductor fabrication techniques (chemical vapor deposition -CVD- or ion implantation, for

instance), calibrated with x-ray fluorescence systems, and then used to characterize ion-beam or x-ray lithography instruments. A derivative application of this technique could be found in single-event upset (SEU) studies of semiconductors: Fiduciary marks could be implanted on a large scale integrated (LSI) circuit chip and then used for precise registration of the probing microbeam.

5. At the expense of sacrificing some of the intrinsic simplicity of the probes, they could be attached to mechanical drives to generate two- and three-dimensional maps of particle distributions.

3.3 Applicability of the Method to the SCFR Diagnostic Needs

The method of particle density determination using multi-element x-ray probes is not limited to the measurements that need to be performed in the SCFR but is also applicable to other experimental situations as can be inferred from the previous discussion. However, since the SCFR diagnostic requirements initially motivated its development, some of the features of the method that help meet those requirements will be mentioned.

1. Passivity. The multi-element probes are passive. No leads need to be brought out of the reaction

chamber, as it is the case with current probes, for instance. This simplifies the insertion of the probes into the chamber which has very limited access.

2. Remote sensing. In most cases, the elements that are selected as target materials emit x-rays sufficiently energetic to be detected through thin windows. Therefore, it is not always necessary to mount the detector inside the chamber itself, as required with backscatter or secondary particle emission probes.

3. Low intrusiveness. Any probe inserted to intercept the particles affects their distribution. This is particularly true near the center of the chamber where particle density is expected to reach very high values. It is therefore desirable to use probes with physical dimensions as small as compatible with their ability to perform the measurement. A wire diameter of less than 1 μm is the maximum acceptable at distances of the order of 1 mm from the center of the distribution. Platinum and gold wires of this size are commercially available and could be used for this purpose. Current-measuring probes of this dimension would not be suitable because they would be smaller than the range of

the particles to be measured; they would collect no charge and yield no output.

4. Simplicity of implementation. Particle distributions can be measured at small or large number of locations with the x-ray probes with equal ease. Only the number of targets mounted on the probe need to be changed as necessary. Because of the probe passivity mentioned above, this is a relatively simple procedure. Probes with up to four different elements were implemented in the experimental part of this work, but there are approximately 12 metals that are compatible with the chamber environment, that have characteristic x-ray with sufficiently high energy to be detectable through windows, and that can be drawn into thin wires. Therefore, in principle, probes with this number of targets could be built. When many elements are used simultaneously, partial overlap of their spectra may occur. This, however, is not a serious problem as shown in Chapter 6 for the case of four-wire probes with partially overlapping spectra. There, a simple correction technique was used in the measurement of beam profiles. For cases were more complex spectral overlap is found, readily available spectral deconvolution software can be used.

5. Partially ionized and neutral particle detection. Atoms become ionized and molecules dissociated shortly after they collide with the target. From that point on they are ionic species, interact with the target material, and generate characteristic x-rays in the manner described in Chapter 4. Therefore, x-ray probes are equally applicable to the measurement of charged or neutral particles. This is a feature that they share with all secondary emission probes; however, this property combined with some of the other characteristics already mentioned makes the x-ray probes especially well-suited for the neutral-particle measurements needed in the SCFR. In Chapter 6, the application of the method to the measurement of partially ionized molecules (H_2^+) and neutral atoms (H) is reported.

3.4 Other Applications for X-ray Excitation Probes

The minimal intrusiveness, relative simplicity, and capability for multi-dimensional mapping of particle distributions are properties that could make multi-element x-ray excitation probes also attractive in applications other than those that motivated their development.

Some of the potential applications of multi-element x-ray excitation probes have already been mentioned, either in the discussion of the SCFR diagnostic requirements or in the description of possible probe configurations. Here, these applications are recapitulated and additional ones are mentioned.

1. Characterization of charged-particle beams in accelerators (particularly, in very high energy accelerators), ion microprobes, and colliding and self-colliding beam systems.
2. Adjustment of particle optics systems.
3. Alignment and quality control of semiconductor ion implanters, ion-beam lithography systems, and other production ion-beam equipment used in semiconductor fabrication and testing.
4. Specialized semiconductor testing, such as single-event upset (SEU) studies.
5. Characterization of experimental heavy-particle therapy systems.
6. Atomic and molecular beam studies.

CHAPTER 4
PRODUCTION AND DETECTION OF X-RAYS FROM TARGETS BOMBARDED BY ENERGETIC PARTICLES

The measurement of spatial distributions of particles using the characteristic x-ray excitation probes developed in this work requires that a correspondence be established between the measured x-ray intensity and the number of particles that strike the targets. This correspondence can be established experimentally by using particle beams of known intensity, or it can be calculated from the geometry of the probes and from published values of x-ray production cross sections. Later in this work, experimental determinations of the relationship between number of striking particles and x-ray intensity are described. In this chapter, an expression for the correspondence between the measured parameter (x-ray intensity) and the unknown variable (number of particles) is derived. This expression is later used (Chapter 7) to calculate particle flux with probes that were not experimentally calibrated and to cross-validate the results obtained from the experimental calibrations. The discussion begins with considerations regarding the interaction of energetic particles with matter and proceeds from that point.

4.1 Introduction

The acquisition of the characteristic x-rays spectrum of a target bombarded by a beam of energetic particles is the result of a process which consists of four distinct parts:

1. Stopping: The loss of energy of the beam in the target.
2. Production: The emission of characteristic x-rays by the target material.
3. Self-absorption: The attenuation of the photons by the target material.
4. Detection: The x-ray detection process itself in which variables such as solid angle, detector efficiency, attenuation by windows, and attenuation by the detector dead layer must be considered.

These four parts will be separately discussed, and the effect of earlier processes on following ones will be analyzed. Finally, the results of the individual steps will be brought together under a single mathematical expression.

4.2 Stopping of Energetic Ions by Matter

The phenomenon of stopping of heavy ions[1] by matter is a topic that has been extensively studied since H. Geiger and E. Marsden published the results of their experiments on the scattering of alpha particles by gold foils in 1909 and 1910 [29,30]. These experiments had been carried out under the direction of E. Rutherford for the purpose of testing the validity of J.J. Thomson's atomic model[1]. Thomson's model predicted that the scattering of heavy charged particles by thin metallic foils would be the resultant of many random individual collisions with the atomic electrons and would follow a narrow bell-shaped distribution about zero.

---

[1] In accordance with common usage, the term heavy ion applies to any charged particle heavier than the electron [29,30].

Although the most significant (if unexpected) result of Geiger and Marsden's experiments was that a few alpha particles underwent an anomalously high scattering, they also showed, as Thomson's model predicted, that most of the particles were indeed scattered with a very small angle.

The exceptional instances of large angle scattering are the most important from the standpoint of their impact on atomic physics because they led Rutherford to the postulation of the nuclear atom [33], but the multiple small angle scattering by the atomic electrons is the most significant mechanism from the standpoint of the stopping of heavy ions by matter. The dominance of this mechanism of interaction has been confirmed by all experiments to date.

---

[1] This was the so-called "plum pudding" model because it represented the atom as a positive charge uniformily distributed throughout the entire volume, with the discrete negatively charged electrons embeded at different points within it.

Conservation of energy and linear momentum in ion-electron encounters requires that small scattering angle corresponds to low energy transfer in each collision, so the energy loss of heavy ions is the result of a very large number of small energy loss events. The energy loss (stopping) of heavy ions in matter and the spread in the values of this energy loss are subjects of direct interest to the study of x-ray production.

The study of the mechanism of interaction of heavy ions with matter was initiated by N. Bohr in 1913-15 [34,35] and, although refinements continue to be made to this day [36,37], Bohr's basic results are still applicable [38].

In 1932, H. Bethe developed an expression for the stopping of heavy ions by matter, which is applicable to high energy projectiles ($E > \sim 400$ kev/amu) [39]. This expression is known as Bethe's formula and is shown below.

$$-\frac{dE}{dx} = \frac{4\pi e^4 z^2}{m_o v^2} NZ \left[\ln\frac{2m_o v^2}{I} - \ln(1-\beta^2) - \beta^2 \right] \qquad (4\text{-}1)$$

where dE = differential of particle energy

dx = differential of distance travelled by particle

z = charge of particle in electronic charge units

e = electronic charge

N = atomic density of the target material

Z = atomic number of the target material

m_o = rest mass of electron

v = velocity of the particle

β = v/c (c = velocity of light)

I = geometric mean of the excitation and ionization potential of the target atoms

Other formulas for the stopping of lower energy particles in dense materials have also been developed. Anderson and Ziegler have fitted these formulas to existing experimental data and have arrived at semi-empirical expressions for the stopping power and range for a number of heavy ions in pure elemental targets. They have published their results in a set of tables and graphs [40]. As an example, their curves for protons in tungsten are shown in Figure 4-1.

As mentioned above, the two quantities that will be of interest later, when the production of characteristic x-rays is discussed, are the energy loss of the heavy ions as they penetrate the target and their energy distribution about the average value at each point along their path. The energy loss as a function of penetrated distance is readily derived from the data of Anderson and Ziegler, and the variance of the distribution is given by the expression derived by Bohr for interaction of the particle with the orbital electrons in the Rutherford's atomic model (Equation 4-2) [35].

$$\xi^2 = 4\pi z^2 e^4 N Z t \qquad (4\text{-}2)$$

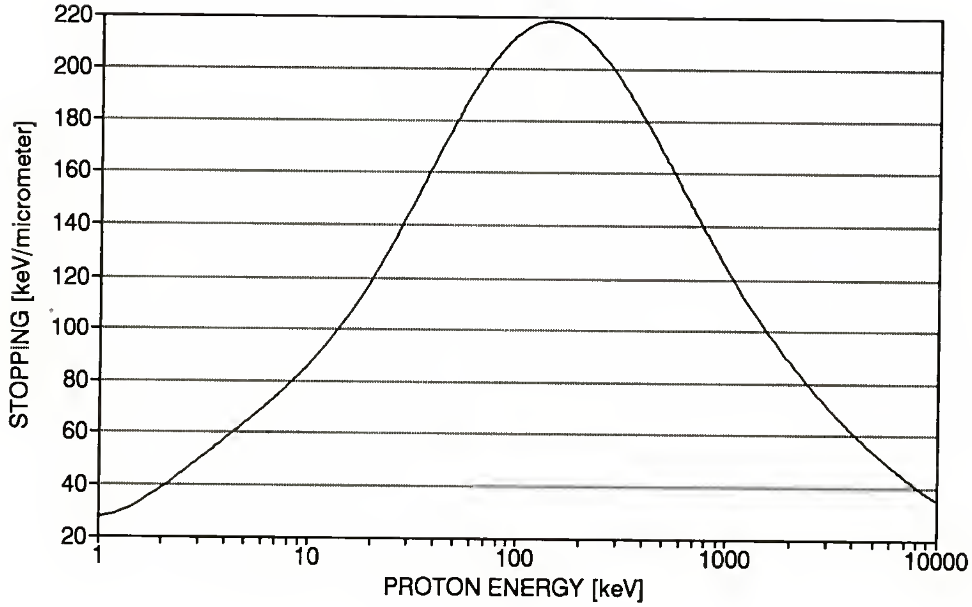

a. Stopping

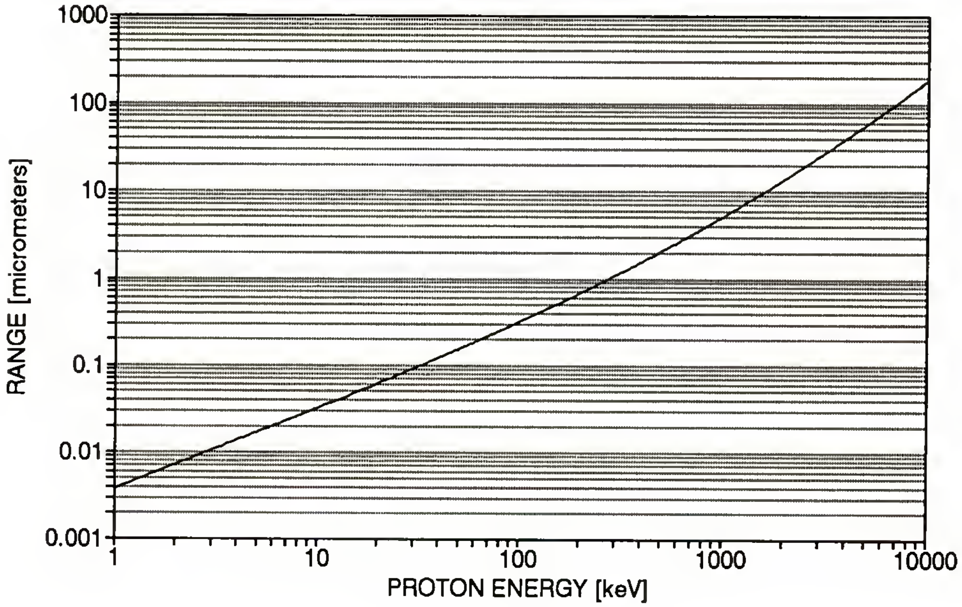

b. Range

Figure 4-1. Stopping and range of protons in tungsten

where ξ^2 = variance

t = thickness of material layer

and the other quantities are as indicated in Equation 4-1.

As an example, the graph of the energy of protons of initial energy E_o = 1 MeV vs. their penetration in a thick tungsten target is shown in Figure 4-2. In this graph, the energy loss was calculated from the range curves of Anderson and Ziegler, and the standard deviation of the distribution at several points (vertical bars) was computed with Equation 4-2.

As shown in the graph, the distribution of energies about an average value is quite narrow until the penetration equals a substantial fraction of the range; it doesn't become significantly broad until the particles have lost most of their initial energy. As will be discussed later, the x-ray production cross section is a very strong function of the particle energy; therefore, a very large percentage of the x-rays are produced in the first few layers of the target where the beam is essentially mono-energetic. It also will be shown later that this phenomenon, combined with the still relatively narrow distribution of energies close to the end of the range, leads to the conclusion that the beam can be considered strictly mono-energetic (no distribution about an average value) at each point along the range without introducing a significant error in the calculated value of x-ray production.

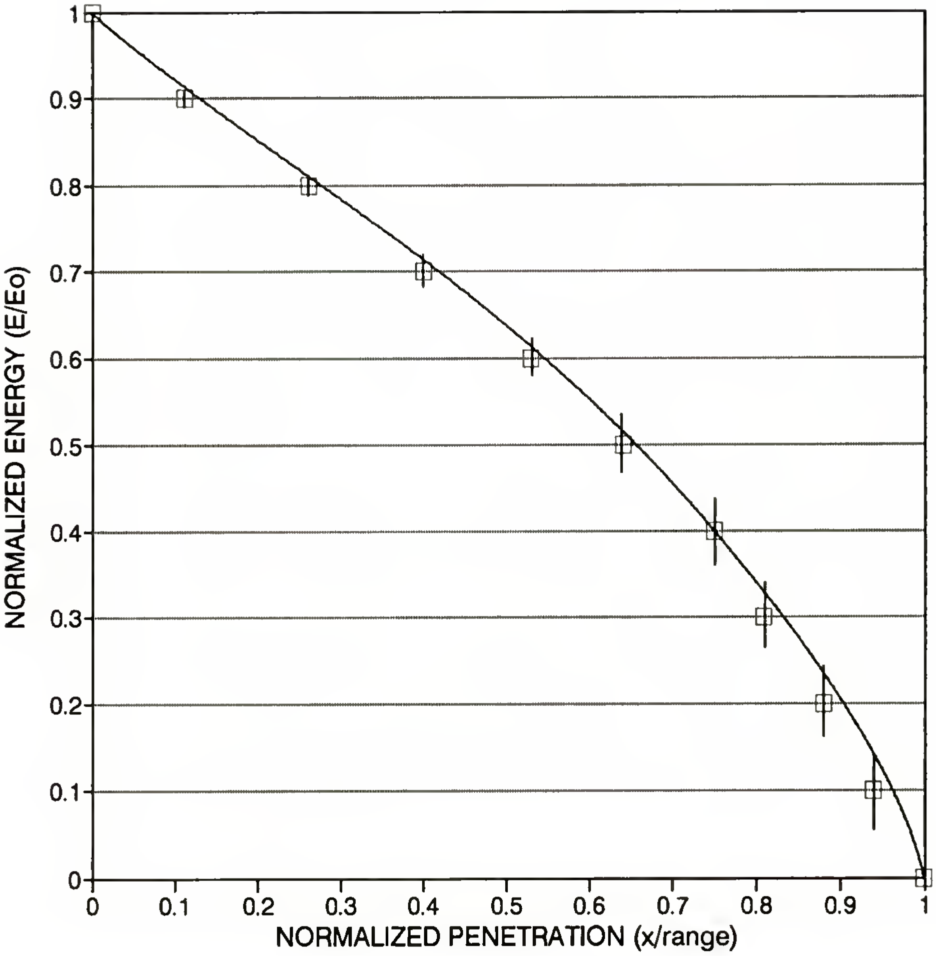

Figure 4-2. Energy loss of a proton beam with initial energy E_0 = 1 MeV as it penetrates a thick tungsten target, graphed from data of Andersen and Ziegler. Curve is a fifth order polynomial fit. Vertical segments are standard deviations calculated with Bohr's formula.

4.3 Production of Characteristic X-rays

In principle, the energy transferred to the atomic electrons by the energetic particles in the manner just described may result in excitation or ionization. In practice, the latter mechanism is strongly dominant; in discussing the production of characteristic x-rays there is no need to discuss the former. The probability of the occurrence of ionization is given by the ionization cross section, σ_i.

Most of the ionization events involve electrons from the outer atomic orbits and this results in the emission of low-energy photons (visible and ultraviolet). These are reabsorbed within the target material and their energy dissipated as heat. However, some of the ionization events involve the ejection of inner-orbit (K, L, or M) electrons. In this case, when the vacancies are refilled one of two phenomena may occur: emission of characteristic x-rays or emission of Auger electrons. These two processes are competitive. The emission of characteristic x-rays is the topic that will be discussed in this section.

Since the binding energies of the atomic electrons are well defined, the characteristic x-ray energies, which are equal to the differences in binding energies between electrons at different levels, also have precisely defined values. In addition, because the energy levels are unique for each atomic species, the emitted x-rays also have energies uniquely associated with each element. The term characteristic indicates this fact.[1]

Usually, in each element there are several possible transitions that result in the emission of x-rays. When the atoms of the element are ionized by the energetic ions, a number of x-rays of well defined energies will be produced. The set of these x-rays is the characteristic x-ray spectrum of the element. While some individual spectral line of a particular element may be quite close to a line from the same or another element and this may make them difficult to resolve, the characteristic spectrum of an element taken as a whole is easily distinguishable from that of a different element. In this respect, characteristic x-ray spectra may be considered to be the signatures or fingerprints of the elements to which they belong. This has led to the present situation in which, just as it was the case for over one hundred years with its optical counterpart, x-ray spectrometry is now a routinely used method of elemental analysis. The widespread application of x-ray spectrometry as an analytical tool was the progress made in semiconductor devices in the 1950s and 60s. This resulted (among many other things) in the development of two components that launched a new era in non-destructive testing technology:

---

[1] The qualifier characteristic will be generally omitted in the rest of this work since this the only kind of x-ray discussed here. If bremstrahlung needs to be mentioned, it will be explicitly so indicated.

the lithium-drifted silicon photon detector and the low-noise field-effect transistor. In later sections, these and other aspects of x-ray spectroscopy instrumentation will be discussed in greater detail.

For the sake of completeness it must be mentioned that, besides the heavy ions discussed here, other modes of target excitation are widely used in x-ray spectroscopy. These include excitation with the bremstrahlung from x-ray tubes, with low energy gamma rays, with characteristic x-rays from other elements, and with electron beams. Each of these modes has its particular advantages and shortcomings, and all have specific applications for which they are best suited. The excitation with heavy ions discussed in this work is usually known by the acronym PIXE, which stands for particle-induced x-ray emission.

At this point a digression will be made to discuss the notation used in x-ray spectroscopy.

Characteristic x-rays are usually identified by symbolic expressions such as $K_{\alpha 1}$, $M_{\beta 2}$, etc. In this notation, known as the Sigbahn notation, the first capital letter indicates the atomic orbit in which the vacancy is being filled [41,42]. All the x-rays that result from filling vacancies in the first orbit (principal quantum number, n = 1) are called K-series x-rays, in the second orbit (n = 2), L-series x-rays, etc. Within a series, the lines appear bunched into groups. The lines of some groups are more intense than those from other groups. The intensity of the group as a whole is indicated by the Greek subindices (α indicates the most intense group, β the next one, etc.). The numeric subindex indicates the relative intensity of a line within a group (increasing numbers indicate successively decreasing intensities). Because this notation uses two classification criteria simultaneously (atomic energy levels and spectroscopy intensity) it is somewhat confusing. In addition, it is not used in a fully consistent manner. Therefore, the International Union of Pure and Applied Chemistry (IUPAC) has proposed an alternate nomenclature ([42], p. 120). In the present work the Sigbahn notation will be used exclusively because of its present widespread acceptance. Figure 4-3 gives an example of how this notation is applied. Figure 4-4 shows examples of characteristic x-ray spectra acquired with a high-purity germanium (HPGe) spectrometer.

The probability of production of characteristic x-rays is given by the x-ray production cross section σ_x, which is related to the ionization cross section σ_i by the fluorescence yield (usually denoted by ω); σ_x is a function of the excitation method, the target material, and the specific x-ray line being considered. For example, the value of the cross section for the production of K x-rays by tungsten when excited with the continuous radiation of an x-ray tube is different from the cross section for the production of the same x-rays when the target is bombarded by 1 MeV protons.

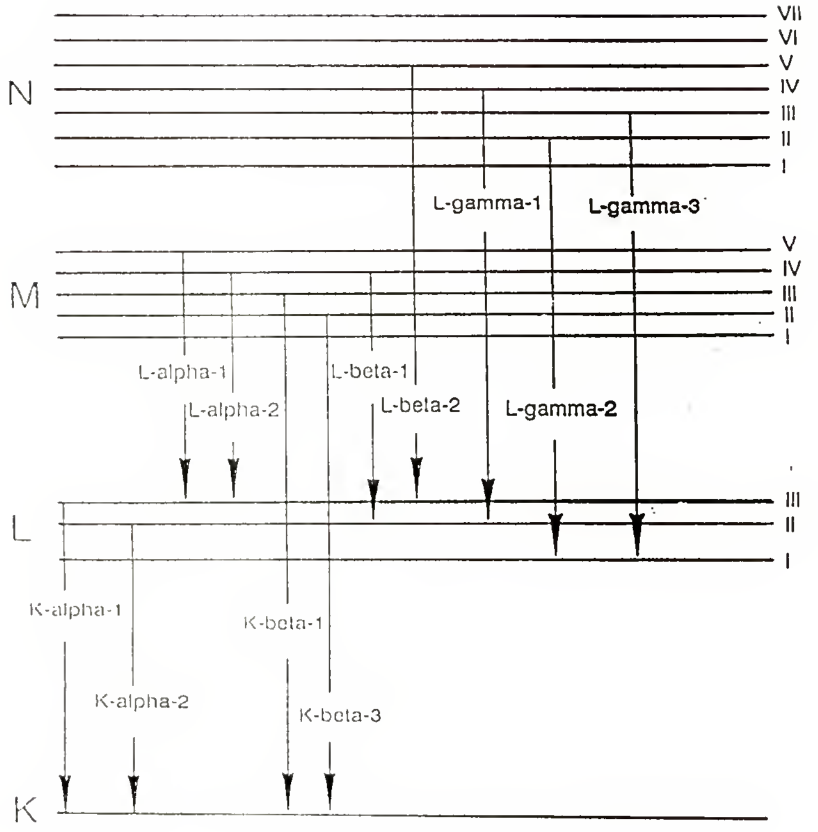

Figure 4-3. Characteristic x-ray nomenclature

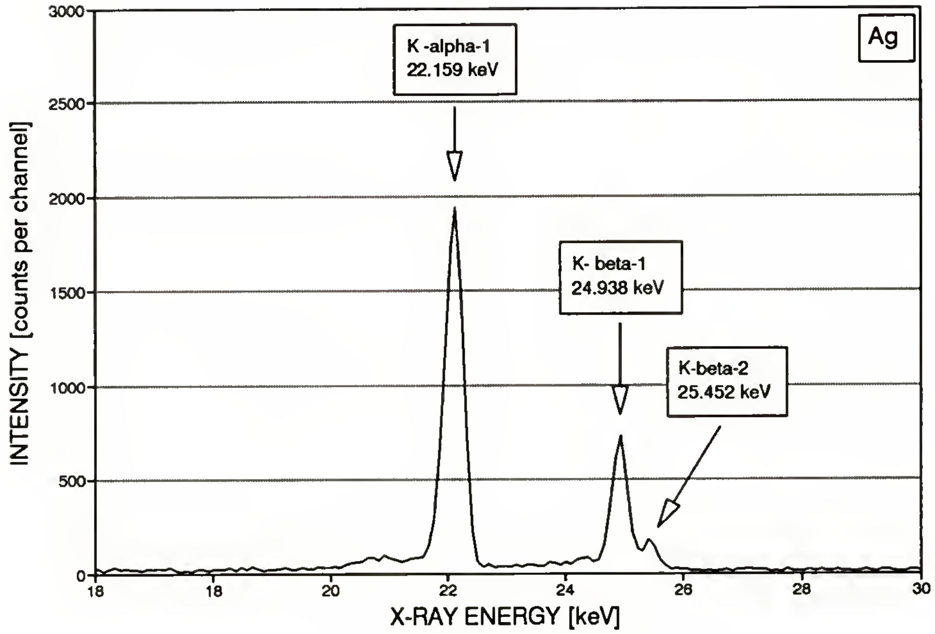

a. K-lines of silver

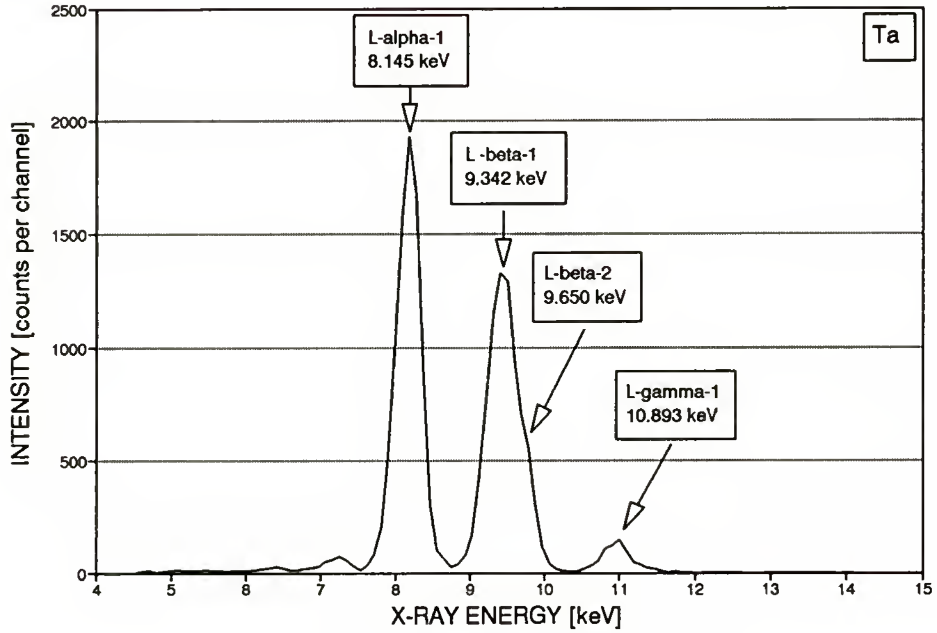

b. L-lines of tantalum

Figure 4-4. Examples of characteristic x-ray spectra

To minimize the possibility of confusion, it is customary to use as subindex for σ the same letter as that of the series being considered: the cross section for K-series x-rays is indicated by σ_K, for L-series x-rays by σ_L, etc.

Measured values of the x-ray production cross section for most elements, means of excitation, and a number of excitation energies can be found in the literature [43,53]. For the purposes of this work, only those cross sections pertaining to excitation with heavy ions are of interest, and unless otherwise indicated, the term cross section will be used only in this sense.

Besides the available experimental data, there are a number of theoretical approaches to the calculation of x-ray production cross sections [54-58]. Garcia et al. have calculated and tabulated values of $u_K{}^2\sigma_K/Z_l{}^2$ vs. E/λ_K, where u_K is the K-shell electron binding energy, σ_K is the K-series x-ray production cross section, Z_l is the atomic number of the target, and λ is the mass of the projectile in amu [54]. Reuter et al. have fitted a logarithmic function to the tabulated data [58]; their expression is given below as Equation (4-3).

$$\log_{10}\left(\frac{u_K^2\sigma^2}{Z_l^2}\right) = \sum_{n=0}^{7}\left(\log_{10}\frac{E}{\lambda u_K}\right)^2 A_n \qquad (4-3)$$

where E = energy of the projectile

A_0 = -19.04

A_1 = 0.03028

A_2 = -1.11

A_3 = 0.3771

A_4 = 0.1923

A_5 = 0.07459

A_6 = -0.05084

A_7 = -0.005949

and the other variables have the meaning previously indicated.

Reid has implemented Equation (4-3) with a computer code, and Figure 4-5 shows examples of graphs of σ_K vs. proton energy calculated with this code [59].

Computed values of cross section must be used only as a general guideline, since in some cases they may differ significantly from experimental data.

Figure 4-6 shows examples of graphs of σ_L vs. proton energy plotted directly from experimental data [43].

As mentioned in section 4.1, a point to be noticed in the graphs or tables is that the x-ray production cross section is a strong function of the energy (approximately fourth power above 500 keV, and even stronger below that energy). This fact is of some help in simplifying calculations of the x-ray yield, since it indicates that only the first few layers of material need to be taken into account. After the particles have lost about half of their

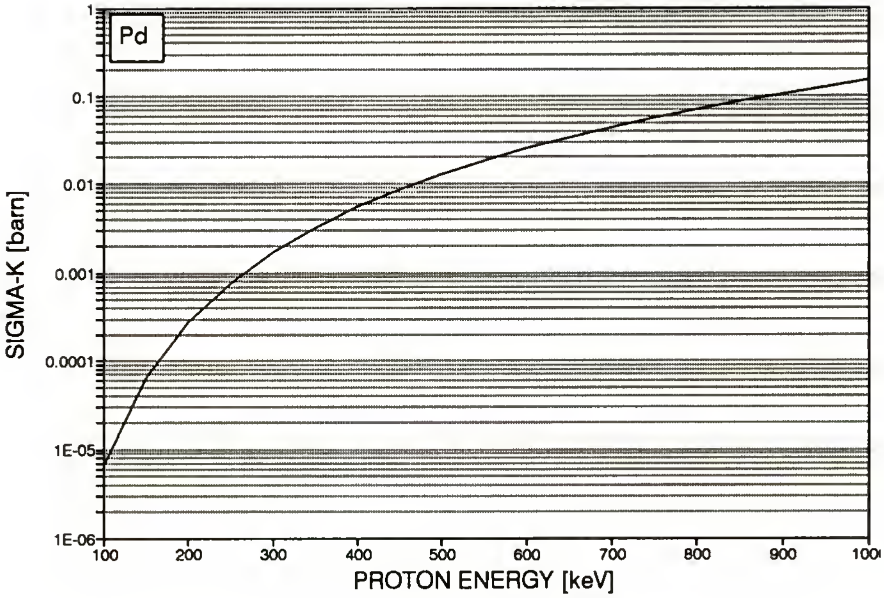

a. Palladium

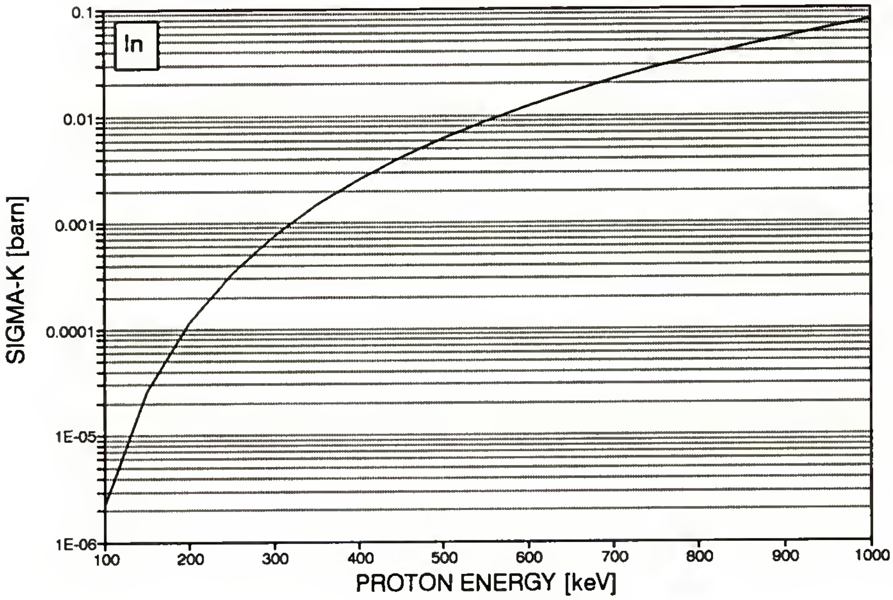

b. Indium

Figure 4-5. K-series x-ray production cross sections computed with Reuter's formula and Reid's program

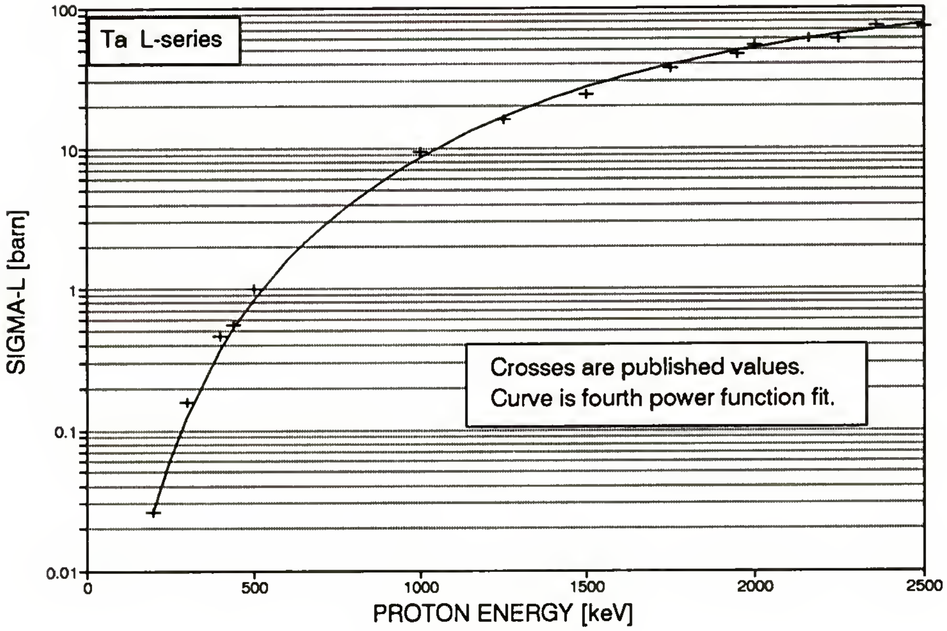

a. Tantalum

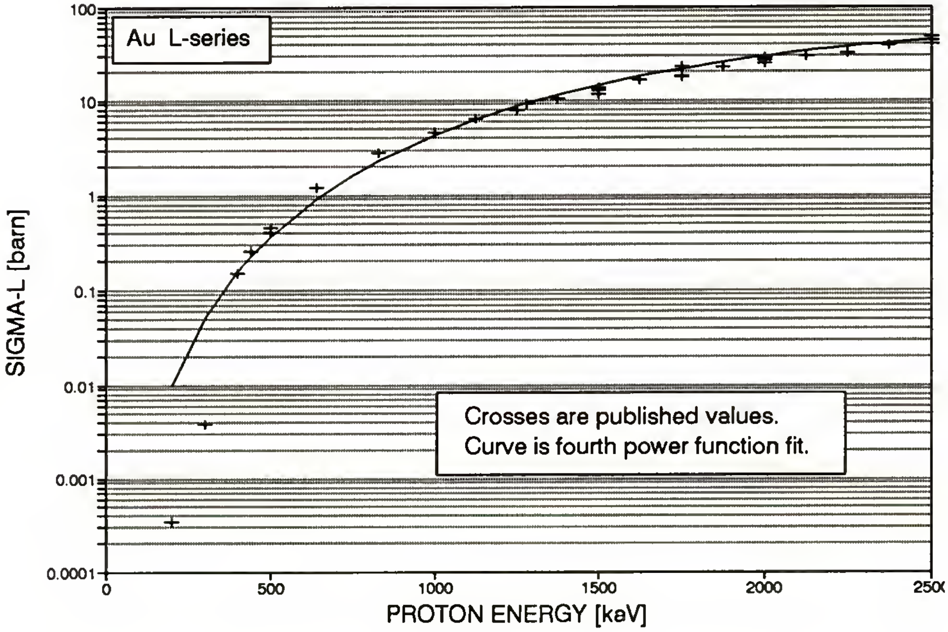

b. Gold

Figure 4-6. L-series x-ray production cross sections plotted from published data

initial energy, their contribution to x-ray production becomes very small.

Another point that should be stressed is that the reported values of the x-ray production cross sections are often given with significant uncertainties (10, 20, or 30 percent, and occasionally even higher), and that in some cases discrepancies among independent measurements are larger than could be expected from the stated errors. Mitchell and Ziegler in the introduction to their table of cross sections (compiled from different sources) state that "the thick target data are specially prone to additional uncertainties caused by energy loss, recoil, and absorption effects" ([43], p. 408).

As the energetic particles penetrate a thick target they loose energy until they come to a complete stop at the end of their range. This process was discussed in Section 4.1. A plot of the average particle energy vs. penetration was shown in Figure 4-2. This figure also showed the standard deviation of the energy distribution about the average. For the purposes of the discussion that follows, it is useful to recast the plot of Figure 4-2 into a graph showing the energy distribution of the particles at different average energies (or at different penetration depths, which is equivalent) as they travel through the target material. This is shown in Figure 4-7.

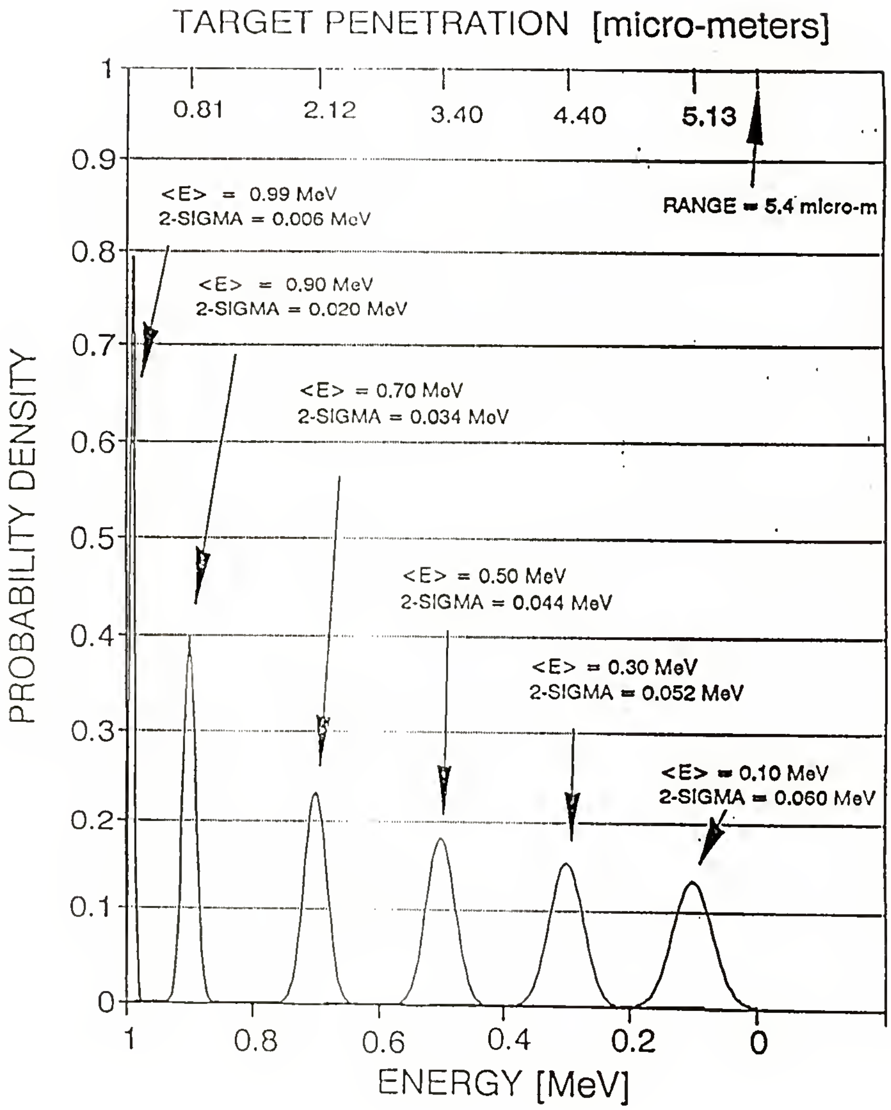

Figure 4-7. Energy distribution of protons of initial energy E_0 = 1 MeV vs. average energy <E(t)>, as they penetrate a thick tungstan target. The areas under the curves are equal.

As they loose energy through interaction with the target, the particles generate characteristic x-rays at each point along their path. Because at each penetration depth the particles have a different average energy and energy distribution, the production of x-rays varies with depth as determined by these two parameters. The x-ray production cross section at a distance t from the point of impact of the particles on the target surface will be called $\sigma(E_{eff}[t])$, and is given by

$$\sigma(E_{eff}[t]) - \int_{0}^{E_o} \sigma(E)\left(\frac{1}{\xi\sqrt{2\pi}} e^{-\frac{1}{2}\left(\frac{E-\langle E(t)\rangle}{\xi}\right)^2}\right) dE \qquad (4\text{-}4)$$

where E_0 = Initial energy of the beam.

$\langle E(t)\rangle$ = Mean energy of the beam at a distance t from the point of impact.

ξ = Standard deviation of the energy distribution.

$E_{eff}[t]$ = Is the effective energy of the beam at t, which is defined as the energy of a mono-energetic beam that would generate the same number of photons as the beam with the given distribution.

Equation (4-4) for protons of E_0 = 1 MeV and the L-series characteristic x-rays of tungsten was approximated numerically using the expression

$$\sigma(E_{eff}[t]) - \sum_{i-1}^{250} \sigma(E)\left(\frac{1}{s\sqrt{2\pi}} e^{-\frac{1}{2}\left(\frac{E-\langle E(t)\rangle}{s}\right)^2}\right)\Delta E \qquad (4\text{-}5)$$

and the obtained values of $\sigma(E_{eff}[t])$ are shown in Table 4-1.

The example given is for 1 MeV protons (approximately in the middle of the energy range of interest for this work) striking a thick tungsten target. However, the conclusions that can be derived from it are quite general because the behavior of the cross section with energy is essentially the same for all elements considered.

As Table 4-1 shows, the difference between the effective and mean energies of the distribution is small, particularly for the first 70% of the particle range where over 99% of the x-rays are produced (< 1%). This leads to the observation that it is permissible to use $\sigma(\langle E \rangle)$ instead of $\sigma(E_{eff}[t])$ in the computations of x-ray yields (see below) without incurring a significant error. This substitution simplifies matters considerably since it makes it

Table 4-1. X-ray production cross-sections for protons in tungsten, calculated with Equation (4-4)

X-Ray Production Cross-Section, $\sigma(E_{eff}[t])$, Effective Energy, $E_{eff}[t]$, and Mean Energy $\langle \bar{E}(t) \rangle$ of the Particle Energy Distribution as a Function of the Target Penetration Depth, t. Target: W. X-Rays: L-Series.

Depth [% of Range]	$\sigma(E_{eff}[t])$ [cm^2]	$E_{eff}[t]$ [MeV] {1}	$\langle E(t) \rangle$ [MeV] {2}	ΔE {1}-{2} [%]	% of Total Production
2	1.31×10^{-23}	0.989	0.990	0.1	38.1
15	8.95×10^{-24}	0.901	0.900	0.1	64.1
29	5.95×10^{-24}	0.801	0.800	0.1	81.4
40	3.28×10^{-24}	0.701	0.700	0.1	90.9
51	1.78×10^{-24}	0.601	0.600	0.2	96.1
64	8.26×10^{-25}	0.497	0.500	0.6	98.5
73	3.56×10^{-25}	0.397	0.400	0.8	99.4
82	1.15×10^{-25}	0.304	0.300	1.3	99.7
89	2.44×10^{-26}	0.206	0.200	3.0	99.8
96	2.13×10^{-27}	0.111	0.100	11.0	99.9

unnecessary to compute $\sigma(E_{eff}[t])$ by carrying out the integration of Equation 4-4 for every initial energy, target material, and penetration depth. Instead, $\sigma(<E(t)>)$ is found through the following simpler procedure: The energy $<E(t)>$ at each depth is found in tables or graphs such as that of Figure 4-2 which, in turn, are plotted from values of stopping power computed by Anderson and Ziegler. The cross section at those energies is then found from tables published in the literature.

In summary, for the purpose of computing x-ray yields an initially mono-energetic particle beam can still be considered mono-energetic at any point within the penetration range; the distribution of energies about a mean value can be ignored. The foregoing argument is found in the literature in the form of simple statements such as the following by Reuter et al.: "The beam energy straggling in the target can be neglected over the effective excitation range" [58], or by Campbell et al.: "The basic premise [for the accuracy of the model] is a proton path which is linear and affords a well-defined proton energy at any given depth" [60].

In the remainder of the discussion of photon yields, this correspondence between a penetration depth and a single energy will be assumed.

The number of x-rays produced at a depth t over a path length dt will be called the differential photon yield, dY(t), and is given by

$$dY(t) = \rho_a \, \sigma(\langle E(t)\rangle)\,dt \qquad (4\text{-}6)$$

where ρ_a = atomic density (atoms of target material per unit volume).

By integration of Equation (4-6), the total photon yield, $Y(E_o)$, is obtained:

$$Y(E_o) = \rho_a \int_0^{R(E_o)} \sigma(\langle E(t)\rangle)\,dt \qquad (4\text{-}7)$$

where $R(E_o)$ = range of particles with initial energy E_o.

Equation (4-7) can be written in terms of energy instead of penetration depth with the relationship

$$dt = \frac{dE}{S(E)} \qquad (4\text{-}8)$$

The stopping power S(E) can be calculated with the expressions given by Anderson and Ziegler. Alternately, the same conversion can be performed through the relationship t = F(E) which can be found from curves such as that of Figure 4-2. The procedures are equivalent, since the curves are drawn from values of S(E). However, because the expression for $Y(E_o)$ must be later combined with the expression for photon self-absorption that is a function of t (the energy E of the particles ceases to play a role once the photons have been generated), it is advantageous to leave it in the form of Equation (4-7).

4.4 Absorption of X-rays in the Target Material

Not all the produced photons escape the target. Some are absorbed within it. This phenomenon is called self-absorption; it is discussed below.

In general, the attenuation of x-rays by matter is governed by the relationship

$$I = I_0 e^{-\mu\tau} \qquad (4\text{-}9)$$

where I_0 = Initial photon beam intensity.

μ = Linear attenuation coefficient of the absorbing material for photons of a given energy.

τ = Thickness of the absorber.

I = Intensity of the attenuated beam.

Extensive tables of attenuation coefficients have been compiled by Hubbell [61]. Usually, the tabulated values are those of the mass attenuation coefficients, μ_m. They are converted into linear absorption coefficients by multiplying them by the density of the material.

To compute the number of x-rays that actually emerge from a target, Equation (4-9) is integrated along the path of the ions within the target material. Often, the quantity of interest is not the total number of photons that emerge from the target but the number of photons that leave the target within a defined solid angle or in a defined direction. The manner in which the actual integration is carried out depends on the target and detector geometry.

4.5. Detection of X-rays

The photons that leave the target within the solid angle of acceptance of the detector may have to pass through one or more external absorbing materials before they reach the detector itself. For extremely low-energy photons, it is sometimes necessary to construct a windowless detection arrangement, including evacuation of the space between the source of x-rays and the detector; in most other circumstances the additional expense that this arrangement entails is usually not warranted. When intervening windows must be used, it is desirable to keep their attenuation to a minimum to increase the detection efficiency.

When n windows exist between the point of production and the point of detection, Equation (4-9) becomes

$$I = I_o\, e^{-\sum_{i=1}^{n} \mu_i \Delta\tau_i} \tag{4-10}$$

where the i's stand for each of the absorbers.

Because for a given experimental situation and for a given photon energy (indicated by the subindex j), the exponential part of the equation is a constant, it will be called the attenuation factor and simply expressed as F_{aj}:

$$F_{a_j} = \frac{I}{I_o} = e^{-\sum_{i=1}^{n} \mu_{ji} \Delta\tau_i} \tag{4-11}$$

Another factor that needs to be considered in the detection process is the absolute efficiency of the detector. In general, not all the photons that penetrate the detector's sensitive volume are necessarily detected.

One of the causes of detection losses is the decrease in photon total interaction cross section with energy. In the case of gas-filled detectors particularly, the detection efficiency decreases rapidly with x-ray energy. Therefore, proportional counters used in x-ray diffraction and spectrometry applications are practical only for detecting very low energy photons.

A second reason for decreased efficiency may be simply the small dimensions of the detector. For instance, if a two millimeter-thick lithium-drifted silicon (Si(Li)) detector is used to detect the K_α line of Ag (approximately 22 keV), only 70% of the photons entering the detector volume will be stopped and detected; the rest will emerge without interaction.

A third factor that may adversely affect the efficiency of the detector is attenuation by the entrance dead layer. For practical reasons, semiconductor detectors for applications involving relatively low-energy photons are fabricated in the shape of flat cylinders (disks). The contacts for the charge collecting electrodes are made on the circular bases of the cylinder. To make a proper contact it is necessary to add some dopant to the semiconductor and to plate the surface (usually with Au). This process creates thin conducting layers on the bases of the cylinder, which for detection purposes are dead layers.

One of the bases of the cylinder is the entrance side, so the photons must traverse it before they reach the sensitive volume. This causes some of the x-rays to be absorbed in the dead layer and results in a loss of efficiency. This effect is only noticeable at photon energies below a few keV, and, unless the detector is windowless, it is of negligible importance compared to absorption by the window.

Another cause for loss of counts may be incomplete or slow charge collection in regions of low field within the detector volume. This phenomenon usually has a larger impact on the resolution of the detector than in its efficiency, and can be almost completely avoided by restricting the photon beam to the high-field region of the detector sensitive volume by means of suitable collimators.

As in the case of the attenuation factor, the efficiency of the detector is a constant for a given set of operating conditions. This constant will be indicated by ϵ.

4.6 The Specific Detected Photon Yield.

In the method for the measurement of spatial distributions of energetic particles developed in this work, a quantity of particular importance is the specific detected photon yield Y_{sd}, defined as the number of detected photons per particle per steradian:

$$Y_{sd} = \frac{X_d}{P_i\ \omega} \qquad (4\text{-}12)$$

where X_d = number of detected photons.

P_i = number of particles intercepted by the target.

ω = solid angle subtended by the detector with vertex at the point photon emission.

For a given set of experimental conditions and x-ray energy, Y_{sd} is a constant. The value of Y_{sd} is computed from the production of characteristic x-rays (Equation (4-7)), the self-absorption (Equation (4-9)), the attenuation factor F_{aj}, the detector efficiency ϵ, and 4π.

$$Y_{sd}(E_o) = \rho_a \left[\int_0^{R(E_o)} \sigma(\langle E(t) \rangle)\, e^{-\mu\tau} dt \right] F_{aj}\ \epsilon\ \frac{1}{4\pi} \qquad (4\text{-}13)$$

For geometries in which the angle of impact and the take-off angle are both equal to 45 degrees, such as shown in Figure 4-8, $\tau = t$.

As can be seen by re-arranging Equation 4-12, the specific detected photon yield is the constant of proportionality that, for a given set of experimental conditions, relates the number of detected photons to the number of particles intercepted by the target:

$$P_i = \frac{X_d}{Y_{sd}\omega} \qquad (4\text{-}14)$$

In other words, Y_{sd} is the basic parameter used in the determination of the number of particles from the values

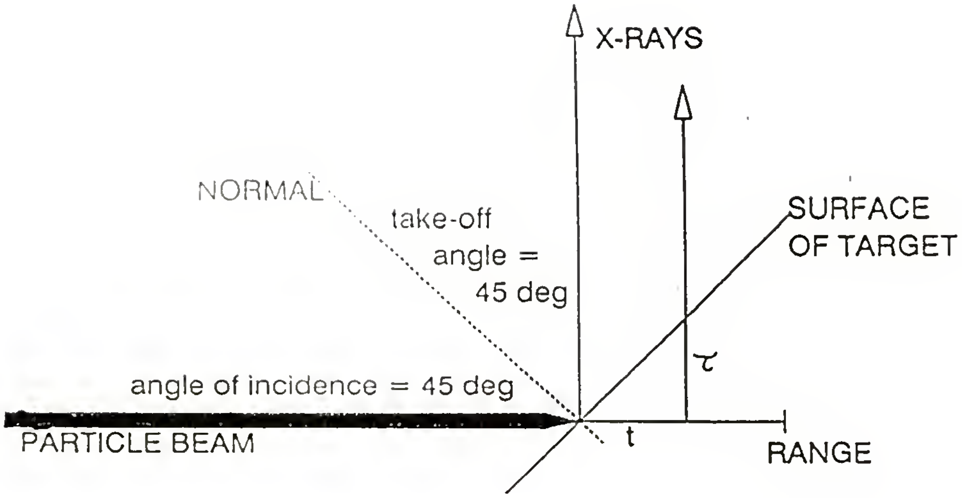

Figure 4-8. Geometry for Equation 4-13

obtained from x-ray measurements. It can be computed from Equation 4-13 for a given geometry, or it can be measured.

CHAPTER 5
IMPLEMENTATION OF THE MULTI-ELEMENT PROBE METHOD

The implementation of the multi-element x-ray emission method may be divided into two parts: The mechanical aspects of the probes and the test chamber, and the instrumentation aspects of the acquisition and analysis of information. The former include the design and construction of the test chamber and the methods of fabrication of the probes, the latter addresses the specification of the characteristics of the detector and the electronic instrumentation used in the detection of radiation, processing of the signals, conversion of the analog information to digital form, and storage, retrieval, and analysis of the acquired data. In this chapter, all of these aspects of the implementation of the system are addressed.

As indicated in Chapter 4, it is important to calibrate the probes in conditions closely resembling those of the actual measurements. On the other hand, as mentioned in Chapter 3, there are many possible variations in the geometrical configuration of the probes. Therefore, for the initial implementation of the probes it was necessary to choose configurations particularly relevant to the main intended applications. Two configuration were selected:

Probes with targets made with thick metallic foils (laminiform probes), and probes with targets made with thin wires (filiform probes). The laminiform geometry was selected because of its importance in establishing a baseline for the measurement of specific photon yields. The filiform geometry is of interest because of its wide range of applications to particle distribution measurements in general and to the planned SCFR experiments in particular.

The acquisition and analysis of even moderately complex x-ray spectra requires the application of strict criteria in the selection of the components of the spectrometry system. These criteria must be applied both to individual module specifications and to the system integration. A discussion of the selection process is included in the sections that deal with each system component, preceded by introductory background material. First, a summary description of the experimental system as actually implemented is given below.

All the experiments were performed in a test chamber mounted at the end of one of the Van de Graaff accelerator beam lines. The test chamber was constructed with one of the beam line sections known as beam diagnostic assembly (BDA) with a thin plastic window fitted on one of its ports (see Appendix) plus other components. The probes consisted of targets (foils or wires) mounted on holders which in turn were attached to the tip of a vacuum-sealed linear motion device (LMD). The LMD was inserted in the chamber through one of the access ports. Details of the test chamber are shown in Figure 5-1. The photons emitted by the targets were detected by a high-purity germanium (HPGe) x-ray detector with integral very low noise preamplifier. A spectroscopy-grade linear amplifier with gaussian shaping was used for signal amplification and conditioning, and a pc-mounted multi-channel pulse-height analyzer for spectrum acquisition and data reduction. A discussion of the main components of the experimental system follows.

5.1 Construction and Assembly of Probes

5.1.1 Laminiform Probes

The laminiform probes consisted of metallic foil mounted on aperture-type holders (Figure 5-2). A list of the materials used as targets for these probes is given in Table 5-1. The holder was attached to an LMD, as mentioned above. The LMD provided the means for moving the targets in and out of the beam path without having to open the test chamber. The laminiform probes were made and tested to determine thick-target x-ray yields of different materials and to perform measurements with partially- and fully-neutralized particle beams.

5.1.2 Filiform Probes

Single- and multi-element probes were implemented using thin wires of niobium, molybdenum, palladium, tantalum, tungsten, platinum, and gold. The diameter of the wires used ranged from 0.010 to 0.127 mm. The single-element probes were used for measuring photon yields and to profile

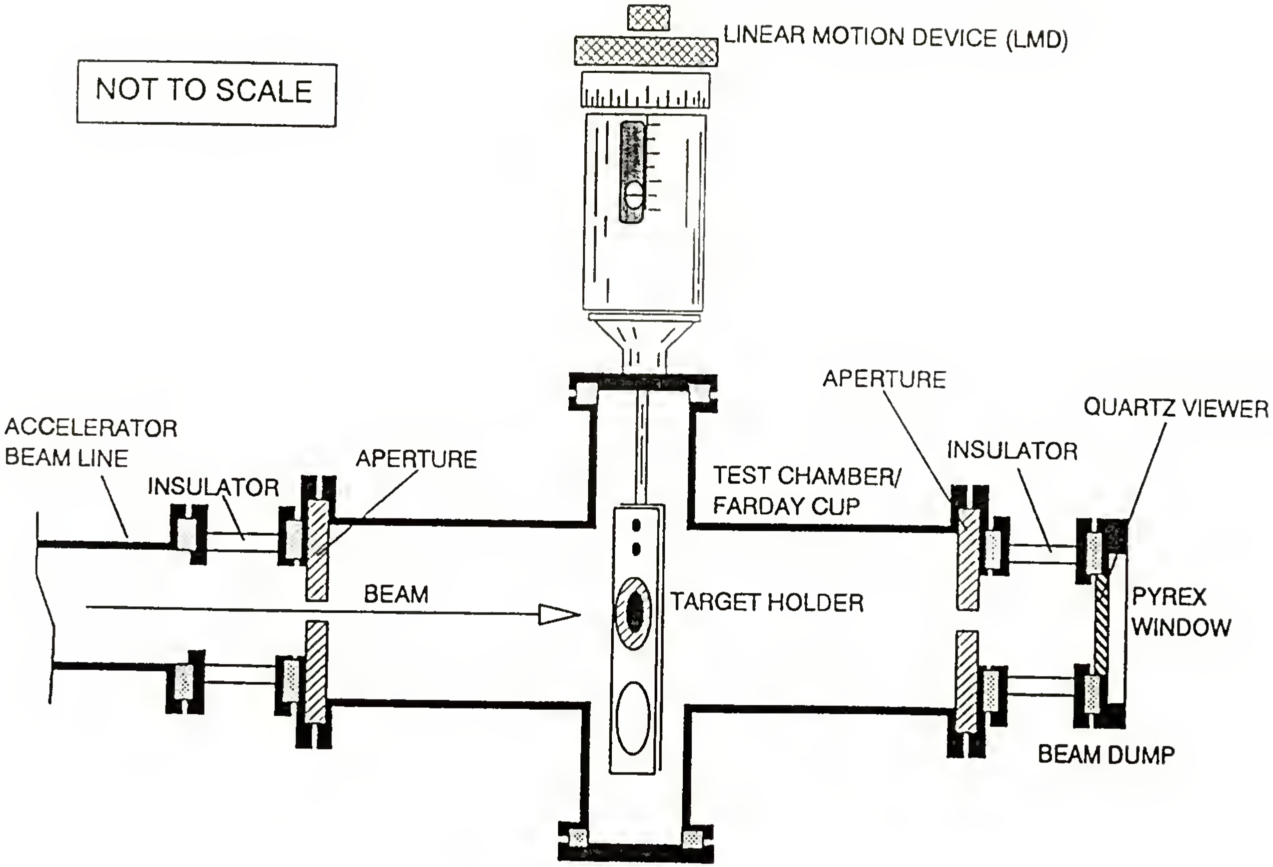

Figure 5-1. Longitudinal section of test chamber showing target holder

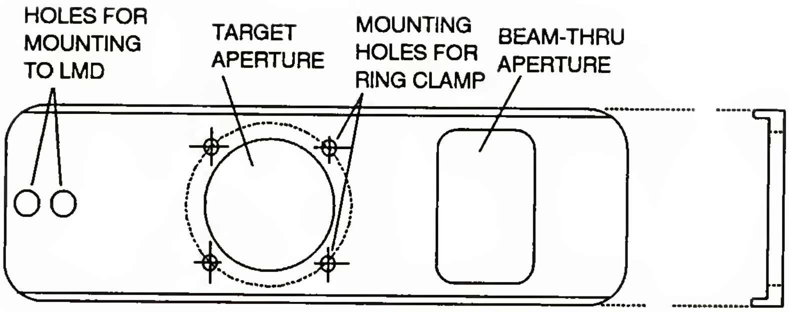

a. Base

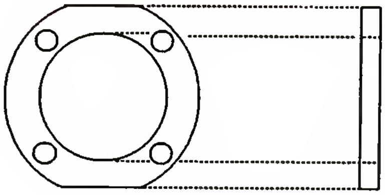

b. Ring clamp

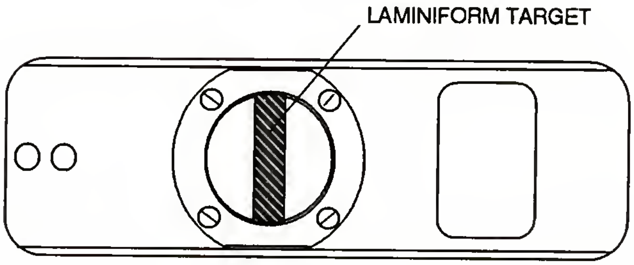

c. Complete assembly

Figure 5-2. Aperture-type holder

ion beams by sequential measurements. The multi-element probes were used for simultaneous multi-position measurements of beam profiles. The wires were mounted on the aperture-type holders previously described or on fork-type holders shown in Figure 5-3. In either case, the holders were fastened to the end of the LMD shaft.

Table 5-1. Target materials used in the laminiform probes

Material (Z)	Thickness of foil [μm]	Range of 2.5 MeV protons in material [μm]
Nb (41)	300	32
Mo (42)	127	29
Pd (46)	60	27
Ta (73)	127	27
W (74)	220	22

A jig was designed and built for mounting uniformly-spaced wires to the fork-type holders. This jig is shown in Figure 5-4. As constructed, the jig can be used for mounting up to six wires with spacings from zero to 2.54 mm. The maximum spacing for six-wire assemblies is limited by the spacing between the steel pins on the rotatable platforms. If a lower number of wires is used, wider spacing can be achieved by mounting them on alternate pins. Intermediate wire spacings between zero and the maximum are obtained by rotation of the platforms. The spacing between wire centers is given by

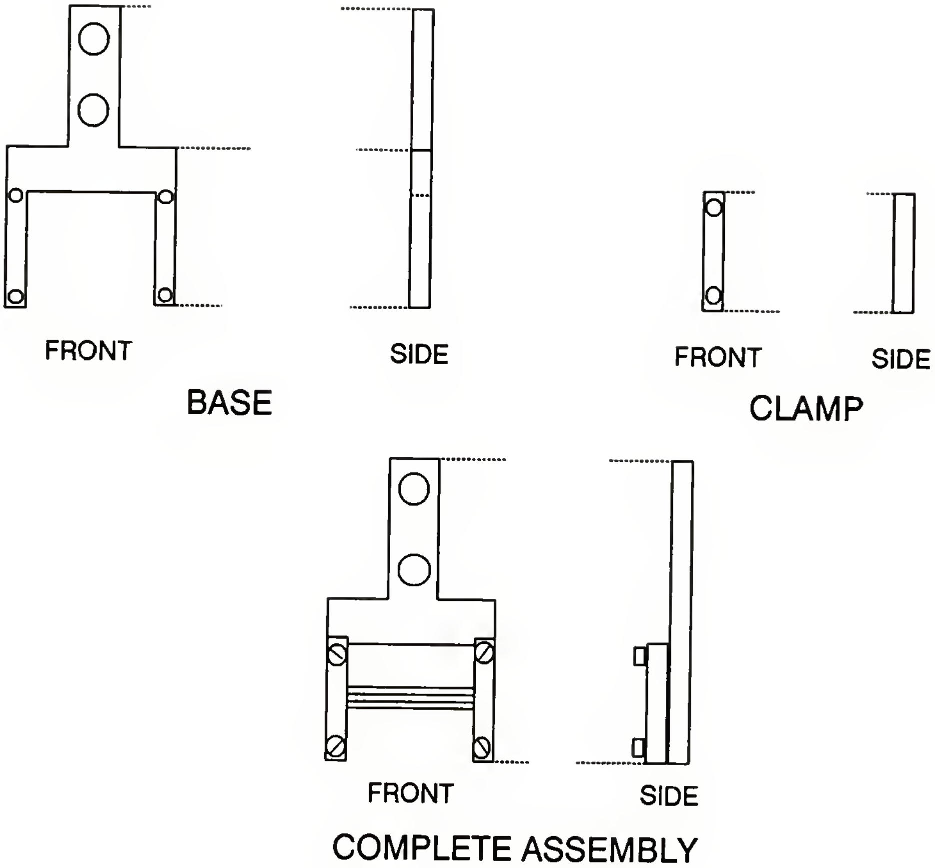

Figure 5-3. Fork-type holder

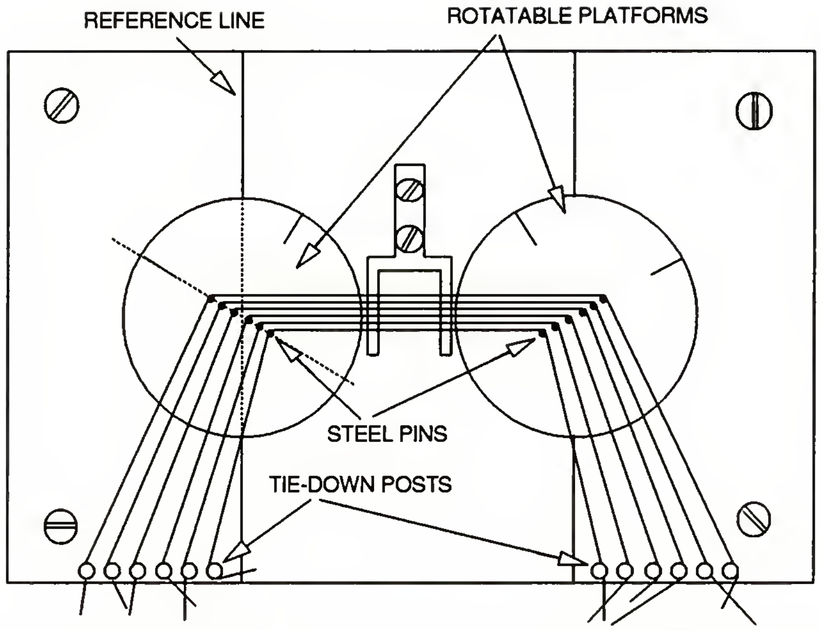

a. Top view showing partially assembled probe

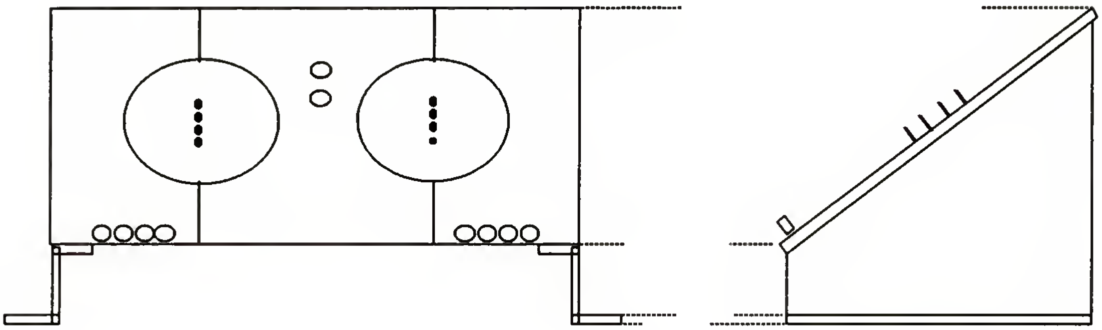

b. Front and side views

Figure 5-4. Jig for assembling filiform probes

$$s = d\cos\alpha \tag{5-1}$$

wheres = wire spacing.

d = distance between pin centers.

α = platform rotation angle.

To install wires with a given spacing, the platforms are rotated symmetrically to the desired angle and secured in place. Then the holder is mounted in position with the hold-down screws. The wires are strung and made taut, and their ends are clamped at the tie-down posts. When all the wires are in place, they are fastened to the holder with the clamping rods and screws. If necessary, aluminum foil shims can be used under and over the wires before clamping to ensure uniform compression. Even wires of nominally equal diameters, have small size differences that may cause some of them to be compressed before others; the aluminum shims usually take care of this problem. The end of the wires are then trimmed with small wire cutters and the frame is removed from the jig. Wires as small as 0.010 mm in diameter were successfully installed with this procedure.

The fork-type holders just described were designed for use in profiling accelerator beams. For other applications holders of different dimensions may be used. The jig that was constructed may be adapted for other holder sizes, or new jigs based on the same general design may be built.

5.1.3 Selection of Materials for Probe Construction

As mentioned in section 3.2, any element that can be drawn into the required shapes, plated to wires or plane surfaces, embedded in a matrix, or otherwise fixed in a desired position, could be used as a component in a multi-element x-ray excitation probe. In practice, there are limitations imposed by the energy of their characteristic photons, their x-ray production cross sections, the behavior of the material in vacuum conditions, and the possibility of interference of their characteristic spectra. In particular, for the probes used in this work the choice of materials was further limited to metals that can be drawn into very thin wires. (Most metals are available in wire sizes of 0.1 mm and larger; several, in sizes of 0.01 or 0.013 mm. Gold and platinum wires can be obtained in diameters as small as 0.0006 mm in the form of Wollaston wire). When all the requirements were taken into account, the list of potential target materials reduced to those in Table 5-2.

5.2 The X-ray Detector

A high-purity germanium x-ray detector was designed specifically for the development work of the multi-element x-ray excitation probes. The detector characteristics were selected to meet the experimental requirements of the calibration of the probes, the determination of intrinsic photon yields, and the physical constraints of future SCFR

Table 5-2. Reduced list of metals suitable as targets in x-ray excitation probes

Element	Atomic number (Z)	Useful x-ray lines	Energy of most prominent line [keV]
V	23	K-series	4.951
Cr	24	K-series	5.414
Co	27	K-series	6.929
Ni	28	K-series	7.477
Nb	41	K-series	16.692
Mo	42	K-series	17.476
Rh	45	K-series	20.213
Pd	46	K-series	21.174
Ag	47	K-series	22.159
In	49	K-series	24.206
Hf	72	L-series	7.898
Ta	73	L-series	8.145
W	74	L-series	8.396
Ir	77	L-series	9.174
Pt	78	L-series	9.441
Au	79	L-series	9.712

applications. The detector was built to these specifications by Princeton Gamma-Tech, Inc. (PGT) of Princeton, New Jersey.

The following considerations determined the characteristic of the chosen design:

1. Non-continuous use.
2. Sufficient resolution.
3. Reasonable efficiency.
4. Physical configuration.

They are discussed in detail in the rest of this section.

5.2.1 Non-continuous Use

It was anticipated that the development work of the probes would require intermittent use of the detector: Periods of intense use while measurements were being performed in the Van de Graaff accelerator interspersed with prolonged idling periods while work was being done in other aspects of the project. This requirement made the choice of a high-purity germanium (HPGe) detector mandatory. HPGe detectors require cooling to liquid nitrogen temperature only when in use, but they can be stored at room temperature for indefinite periods of time. On the other hand, lithium-drifted silicon (Si(Li)) detectors, which were the second possible choice, require continuous cooling to avoid permanent damage. No advantages were found in these detectors to offset this serious shortcoming, so they were withdrawn from consideration in the early stages of the design.

5.2.2 Sufficient Resolution

The ability of a detector to separate x-rays lines of different energies is measured by its resolution. The resolution of a detector is usually expressed as the full-width at half-maximum (fwhm) of spectral lines. This definition is illustrated in Figure 5-5. The overall resolution of a spectrometry system is usually lower (larger fwhm) than the resolution of the detector itself. This is because there are other factors that affect the resolution in actual experimental conditions, such as preamplifier noise, pulse shaping, and count rate; these will be addressed in following sections. In principle, the resolution of a detector should be specified so that adequate separation between all the spectral lines of interest could be obtained. In practice, it can't be arbitrarily specified since it is limited by fundamental physical processes and by conflict with other specifications, such as efficiency. In addition, it is not meaningful to specify a high detector resolution if preamplifier noise, for instance, would ultimately determine overall system resolution. Therefore, the resolution is usually specified as the minimum required to meet the needs of the experiment. In many cases, this is an important point from the economy standpoint since the cost of semiconductor detectors rises rapidly with resolution. The

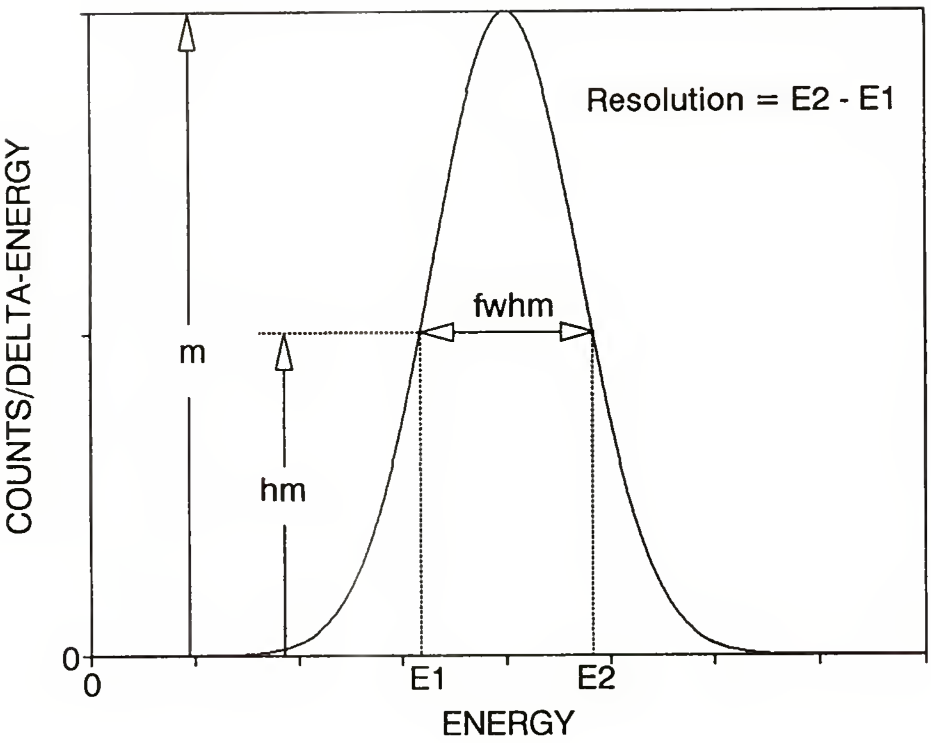

Figure 5-5. Definition of resolution

resolution of the detector acquired for this work was specified with the goal of maximizing the number ofdifferent targets that could be used in a probe and still being able to resolve at least one prominent peak for each element. Taking into consideration that the minimum spacing between lines of interest is approximately 500 eV (the difference between K-series of low-Z elements), a resolution of approximately 250 eV at the low energy end of the spectrum was deemed acceptable. It should be pointed out that this specification is for the detector/preamplifier combination since, by necessity, the two components are part of an integral assembly. This is explained in section 5.3.

5.2.3 Reasonable Efficiency

To attain good sensitivity, it is desirable to make the solid angle of detection as large as possible. For a detector of small diameter compared to the target-to-detector distance, the solid angle ω is given by the ratio

$$\omega = \frac{A_d}{r^2} \ (steradians) \qquad (5\text{-}2)$$

where A_d = area of detector

r = target-detector distance

This implies that for good efficiency the detector must be placed very close to the point where the photons are generated, or that the area of the detector must be very large, or both. As it will be discussed later, there are practical consideration that restrict the detector size.

Therefore, the diameter of the detector was determined by these considerations rather than by the desired efficiency.

For the higher energy lines, the detector efficiency is also a function of its thickness. Photons are absorbed exponentially as they penetrate matter. In the range of photon energies of interest to this work ($h\nu < 100$ keV) the main mechanism of interaction is the photoelectric effect. Therefore the absorption by the germanium crystal is a strong inverse function of the energy ($\sim(h\nu)^{-3}$). The highest energy photons that needed to be efficiently detected in this application were those corresponding to the $K_{\beta 2}$ line of silver (25.452 keV). For 99 per cent or better absorption of 25 keV photons in the detector, the minimum acceptable thickness is obtained from

$$\frac{I_a}{I_o} = 0.99 > (1-e^{-\mu x}) \qquad (5\text{-}3)$$

where μ = 158 cm^{-1} (linear absorption coefficient for Ge for 25 keV photons)

Equation 5-3 yields $x \geq 0.3$ mm for the minimum thickness, which is easily attainable. Therefore, the detector acquired for this work had a thickness several times larger than the minimum.

5.2.4 Physical Configuration

The physical configuration of the detector was determined not only by the general requirements of the x-ray excitation probe but also by the additional requirement of being able to use it in actual SCFR experiments. As a result of this, the need to meet the rigid physical constraints imposed limits to other detector specifications. The physical configuration of the detector was largely determined by the following.

Measurements in the vicinity of the reaction chamber of the SCFR will require that the detector be introduced to the desired position through an access port between the superconducting solenoids. This dictated that the vacuum chamber (end cap), which is part of the cryostat assembly, be at least 400 mm long to reach the edge of the reaction chamber, and no larger than 35 mm in diameter to fit in the access duct. With an end cap of these dimensions it will be possible to place the germanium crystal itself, which is mounted at the tip of the copper cooling rod (cold finger) at the far end of the end cap, very close to the point of production of x-rays. In addition, it was necessary to use a liquid nitrogen reservoir (dewar) capable of being mounted in any orientation and with dimensions sufficiently small to fit between the various obstructions found around the superconducting magnets.

The principal manufacturers of x-ray spectrometers were contacted regarding their capabilities for producing a detector with the desired specifications at a reasonable cost. Two suppliers (EGG Ortec and PGT) indicated that they could work on non-standard detector configurations. Eventually only PGT was able to guarantee delivery within an acceptable time frame. This manufacturer had a crystal in stock that essentially met all of the requirements, and that they could mount on a cryostat/dewar assembly of the specified design. A drawing of the detector "as built" indicating its principal dimensions is shown in Figure 5-6. Other detector specifications "as delivered" are listed below.

Geometry: Planar.

Sensitive region area: 200 mm^2

Thickness: 10 mm

Dead-layer thickness: 6×10^{-4} mm

Window material: Beryllium

Window thickness: 0.127 mm (0.005 in.)

Window area: 400 mm^2

Resolution: 187 eV @ 5.9 keV, 208 eV @ 6.4 keV,
244 eV @ 14.4 keV, 500 eV @ 122 keV,
510 eV @ 136 keV

Recommended bias: -1,500 V

5.3 The Very Low Noise Preamplifier

The preamplifier used with the HPGe detector is part of the integral assembly that includes the cryostat, the detector itself and, in this case, also the liquid nitrogen reservoir (dewar). The need to incorporate the preamplifier

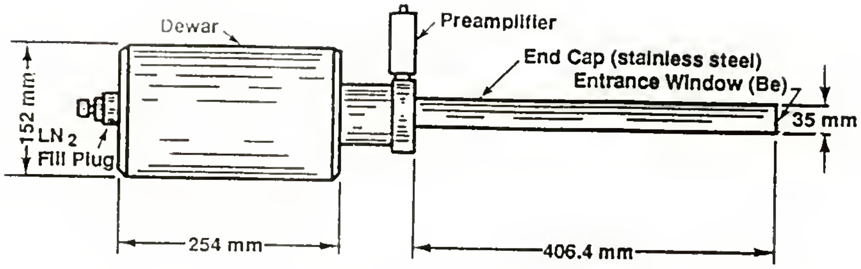

a. Overall view

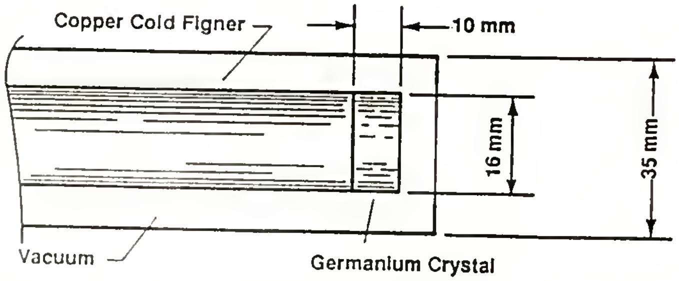

b. End-cap detail

Figure 5-6. High -purity Germanium detector

in this assembly[1] stems from the requirement of reducing the system noise to a minimum.

As mentioned in the introduction to this chapter, the performance of each of the components of the spectrometry system must be carefully considered when acquiring the characteristic x-ray spectra emitted by the multi-element probes. In the case of the preamplifier, noise level is the critical specification. The width of the spectral lines, particularly in the case of low count rates of low-energy photons, is largely determined by the preamplifier noise. Therefore, special attention should be given to the preamplifier noise specifications.

Essentially, all of the noise of a spectrometry system is generated at the preamplifier input stage. If the gain of the first stage is sufficiently high, the noise contribution of subsequent stages can be neglected. The input stage of preamplifiers used in nuclear and x-ray spectrometry consists of field-effect transistors (FET's) selected for their unusual broad-band low-noise characteristics from among a large number of production devices. For x-ray and low-energy gamma-ray spectrometry applications, the selected transistors are refrigerated to temperatures near that of liquid nitrogen to further reduce their noise level. Although because of this reason alone it makes sense to mount the preamplifier on the cryostat where a source of liquid nitrogen is already available, a second reason equally important that requires close proximity between the gate terminal of the input FET and the semiconductor detector is reduction of the total input capacitance, as discussed below.

---

[1] The detector-cryostat-dewar-preamplifier assembly is sometimes referred to as the "x-ray spectrometer." In this work, the term spectrometer will be used only in the sense of spectrometry system, which also includes all other components up to the data reduction system.

The noise of the system is determined, among other things, by the ratio of the transconductance g_m[1] of the input FET to the total capacitance C_t from its gate terminal to ground. Low noise systems are characterized by a high value of g_m/C_t.

The FET transconductance is determined by the device geometry and drain current; the former is fixed by the manufacturing process, the latter is optimized by circuit design. C_t is the sum of the input capacitance C_i of the FET, the detector capacitance C_d, the feedback capacitance C_f, and the stray capacitance C_s. Once an FET has been selected for its low noise characteristics, and a detector for its resolution and efficiency specifications, C_i and C_d

---

[1] The transconductance (also called mutual conductance) of an amplifying device such as a vacuum tube, a bipolar transistor, or an FET is defined as follows:

$$g_m = \frac{\Delta i_o}{\Delta v_i}$$

where $\underline{\Delta i_o}$ = change in the output current (plate, collector, or drain current).
Δv_i = change in the input voltage (grid-cathode, base-emitter, or gate-source voltage).

are fixed; C_f is determined by considerations of preamplifier rise-time and gain stability. Therefore, C_s must be kept to a minimum to maximize g_m/C_t. C_s consists of the capacitance to ground of the leads that connect the detector, feedback capacitor and feedback resistor to the FET gate. It follows that to minimize C_s the input FET must be physically placed as close to the detector as possible. In practice, the input FET is mounted directly on the "cold-finger" next to the detector to keep the length of the lead connecting the detector signal terminal with the FET gate terminal extremely short; the feedback components are placed next to the FET. The rest of the preamplifier circuit is mounted externally but as close as possible to the input FET; this is done to avoid circuit unstability.

Preamplifiers for nuclear and x-ray spectrometry are of the charge-sensitive type. A diagram of a charge-sensitive preamplifier is shown in Figure 5-7. The charge-sensitive configuration has become the circuit of choice since the introduction of semiconductor detectors because of their unique characteristic of delivering an output voltage signal whose amplitude is proportional to the collected charge, and essentially independent of the detector capacitance. This characteristic of charge-sensitive preamplifiers is highly desirable because, as shown below, it means that the calibration of the system in terms of output signal amplitude vs. radiation energy remains approximately

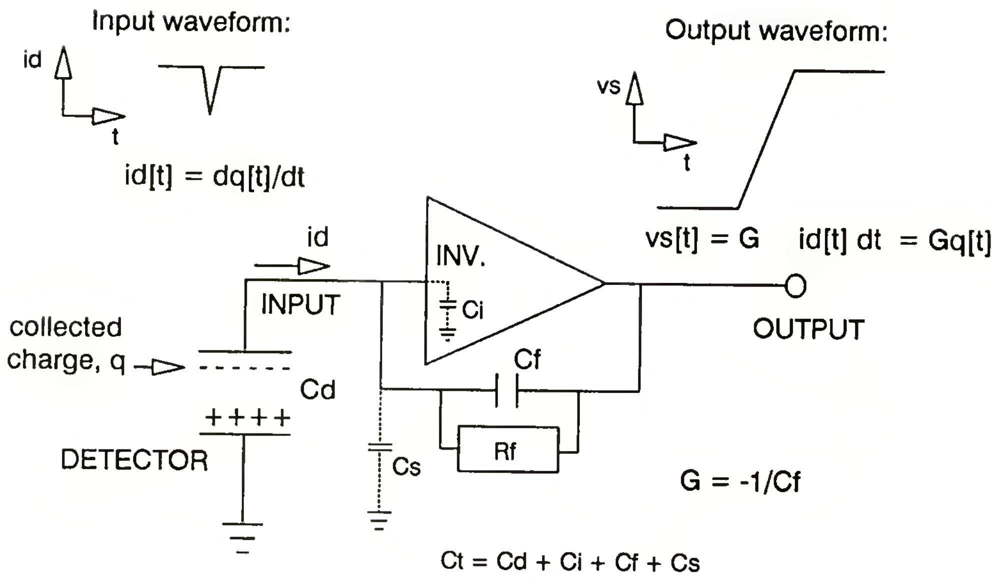

Figure 5-7. Charge-sensitive preamplifier

constant with changes in detector capacitance, and even when switching from one detector to another of similar type. Since the capacitance of semiconductor detectors may vary with the applied bias voltage, the constancy of the conversion gain is of critical importance.

The conversion-gain[1] G of a charge-sensitive preamplifier is given by

$$G = \frac{v_s}{q_i} = -\frac{1}{C_f} \qquad (5\text{-}4)$$

where vs = voltage signal at the output of the preamplifier.

qi = charge collected by the detector and deposited at the input of the preamplifier .

C_f = feedback capacitor.

Therefore, if the energy w necessary to produce a pair of free charges in the detector is known and the amplitude of the preamplifier output signal is measured, the energy E of the detected radiation can be readily computed from the following expression:

---

[1] Because the output of a charge-sensitive preamplifier has the dimension of voltage, and the input of charge, the term conversion-gain has been coined to indicate the relation between the two quantities. It has the dimension of capacitance^{-1}.

$$E = \frac{wv_s C_f}{e} \tag{5-5}$$

where e is the electronic charge.[1]

It should be noticed that the detector capacitance doesn't appear in Equation 5-5. This is another significant advantage of the charge-sensitive configuration, since C_d is and ill-defined quantity usually inconvenient to measure.

These reasons have resulted in the practically universal use of charge-sensitive preamplifiers in nuclear and x-ray spectrometers, and this type of instrument was the choice for this work. One aspect of the circuit requires a brief mention here to justify the selection of the particular type of charge-sensitive preamplifier known as resistor-feedback configuration.

Strictly speaking, the feedback resistor R_f (Figure 5-7) is not an essential part of the charge-sensitive configuration, but its inclusion in the circuit is usually indispensable because of the following. The output signal of a charge sensitive stage is a voltage step. Each time an event is detected and charge is collected, a new step is generated. Without R_f these steps would have perfectly flat tops. Therefore, they would pile up on top of each other until the dynamic range of the preamplifier was reached (saturation). To avoid this condition, resistor R_f is included to provide a leakage path for capacitor C_f. This causes the top of the steps to decay slowly (with the time constant $T_f = R_fC_f$). In this manner, the output of the preamplifier is maintained at an average dc voltage which is a function of the input current (determined by the radiation energy and the count rates). Saturation occurs only in the case of extremely large individual signals or very high count rate [62]. However, the inclusion of R_f has two undesirable collateral effects: It introduces an additional time constant and it increases the noise level.

---

[1] In reality, this measurement is somewhat more involved because additional amplification and pulse shaping are necessary.

The additional time constant, if not dealt with properly, causes undershoots at the output of the main amplifier which reduce the spectral resolution even at moderate count rates. Fortunately, the undershoots can be compensated in the main amplifier by means of the scheme known as pole-zero cancellation and it ceases to be a real problem, only an inconvenience [63]. All state-of-the art linear amplifiers used in x-ray spectrometry have the pole-zero cancellation feature. The pole-zero compensation is usually adjustable by means of a multi-turn potentiometer at the front panel of the main amplifier. It must be individually set for each preamplifier.

The increase in noise level is a more serious problem; it can be minimized but not eliminated as long as a feedback resistor is used in the circuit. The noise generated by the feedback resistor is known as thermal or Johnson noise [64].

It is caused by the thermal agitation of the electrons in the resistor, and its voltage spectral density is given by

$$\frac{v_t^2}{\delta f} = 4kTR \tag{5-6}$$

where v_t = thermal noise voltage at the resistor terminals.

δf = small frequency interval.

k = Boltzman's constant.

T = temperature [K].

R = resistance of the device.

From this equation, it would appear that the larger the resistor, the higher the system's noise. However, the opposite is true because the resistor's parasitic shunt capacitance and the spectrometer's finite bandwidth combine to make the noise components of interest an inverse function of R_f [65]. Therefore, the largest value of R_f compatible with avoidance of saturation is selected. It is not unusual to see preamplifiers with $R_f > 10^9$ Ω.

In 1969, Goulding et al. introduced a novel scheme for dc feedback of charge-sensitive preamplifiers known as pulsed optical feedback (POF) which obviates the need of a feedback resistor. Currently, POF is implemented by replacing R_f in the standard charge-sensitive configuration with the components shown in Figure 5-8. The operation of the circuit is described below with reference to that figure.

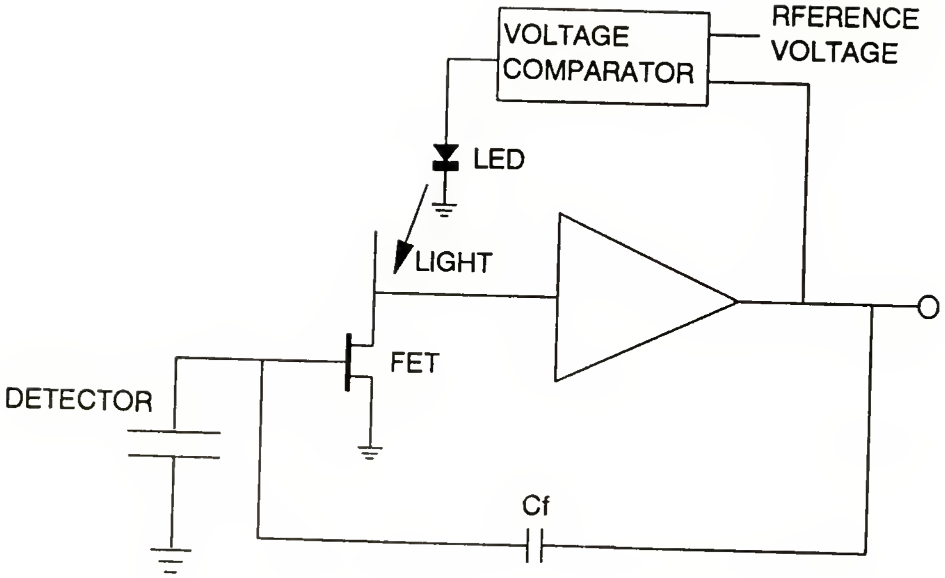

Figure 5-8. Pulsed optical feedback charge sensitive preamplifier

As radiation is detected, the output of the preamplifier shows the staircase waveform previously described. Since the preamplifier has no dc-feedback (no R_f), the top of the steps are perfectly flat and the output dc level grows unchecked. When this level reaches a certain preset value (determined by the reference voltage) the comparator flips states and commands the driving circuit to energize the LED. The LED shines on the FET chip creating current carriers which are free to penetrate the reverse-biased gate-channel junction. The increase in conductivity of the junction drastically reduces the input resistance of the device causing C_f to rapidly discharge through this path. The output voltage returns to zero and the voltage comparator to its original state. The LED is turned off and the preamplifier begins a new cycle. While this resetting process is in progress the spectrometer is gated off to prevent spurious signals from being recorded.

By means of this scheme two desirable goals are accomplished: The Johnson noise introduced by the feedback resistor is completely eliminated, and the total input capacitance is reduced by the amount usually contributed by the feedback resistor lead.

Optical feedback preamplifiers are widely used in high resolution x-ray spectrometers. However, in the system designed for this work, it was not possible to incorporate this feature without great inconvenience. This was because the unusually long and narrow end cap required for the reasons discussed before interfered with the installation of the necessary feedback components inside the cryostat. In addition, since the resolution of the system was sufficiently high without this refinement, it was decided to compromise and use a standard feedback circuit.

Finally, another factor that in theory is of importance in the performance of low-noise preamplifiers is their differential non-linearity, but it will be only briefly discussed here because as indicated below, in the case of the x-ray excitation probe experiments it has no detectable effects. Loosely defined, differential non-linearity is a measure of the constancy of the gain (or conversion gain) over the dynamic range. High differential non-linearity in the preamplifier results in a rapid deterioration of resolution with count rate. However, in a properly designed spectrometer, preamplifier non-linearity is not a problem since count rate performance is determined by the main amplifier [62]. The main amplifier is discussed in the next section.

5.4 The Linear Amplifier

Another of the critical components of an x-ray spectrometer that should be selected taking into consideration the effect of several of its characteristics on the spectra from multi-element excitation probes is the linear amplifier. To fully realize the excellent intrinsic resolution of the HPGe detector and the low-noise characteristics of the preamplifier it is necessary to process the signals with a linear amplifier of adequate specifications. Of particular importance is the ability of the amplifier to improve the signal-to-noise ratio of the system and to maintain good spectral resolution with increasing count rate. These, as well as other characteristics of the linear amplifier are discussed in this section.

The low-level signals at the output of the low noise preamplifier (voltage steps) are not suitable for direct analysis. It is necessary to amplify them to levels that can be more conveniently processed by the analog-to-digital converter (ADC) and to filter them to improve their signal-to-noise ratio (SNR). These functions, in addition to others mentioned below, are performed by the linear amplifier.

The linear amplifier, also known as main amplifier, shaping amplifier, and spectroscopy amplifier, consists of several amplification stages that boost the signal to the desired level, filters that increase the SNR and re-shape the signal, and auxiliary components that perform the functions of pole-zero (P-Z) cancellation, baseline restoration, and, sometimes, pile-up rejection.

5.4.1 Amplification

Amplification is the primary function of the linear amplifier, and the need for it is the most readily intuitively understood. In the early days of nuclear spectrometry, amplifiers were used almost exclusively for this purpose, perhaps with the addition of some rudimentary shaping. In the amplifiers used in the implementation of multi-element x-ray probes, this function must be performed in such a way that a linear relationship of signal amplitude to photon energy is maintained throughout the process. The pertinent aspects of this function are discussed below.

Amplification (or gain) A is defined as the relationship between the output v_o and the input v_i of a voltage amplifier:

$$v_o = A v_i \tag{5-7}$$

where, ideally, A should be a constant. In practice, A depends on the signal level and to some extent on the instrument operating temperature. This dependence is described by the linearity and temperature coefficient specifications.

The degree to which A departs from a constant, as function of v_o, is called the amplifier non-linearity. Two types of non-linearity are particularly relevant to spectrometry systems used with x-ray probes: Integral and differential.

If A' is the amplification at the maximum rated output voltage v_m, the maximum value of the difference $\Delta v_o = Av_i - A'v_i$ expressed as a percentage of v_m is the integral non-linearity L_i [66]:

$$L_I = 100 \frac{\Delta v_o}{v_m} \tag{5-8}$$

The differential non-linearity is defined as: "the change of incremental gain, usually expressed as a percentage of a reference gain" [66].

Integral non-linearity is the only type of non-linearity that needs to be considered in main amplifiers. In state-of-the-art amplifiers, the differential non-linearity is usually so low that its effect on overall system performance can be neglected.

Integral non-linearity affects the energy calibration of the x-ray spectrometry system (energy vs. channel number). Accurate energy calibration is particularly important for identification of peaks with close energies, as may be found in some multi-element probes. When the experimental work requires such peak identification, either the spectrometer must be linear or the integral non-linearity must be accurately known.

The acceptable value of the integral non-linearity of the main amplifier is specified to satisfy the particular experimental requirements. The following is a discussion of one way of estimating this value in the case of amplifiers to be used with multi-element x-ray excitation probes.

The adopted criteria is that if perfect linearity is assumed, the error resulting from using a straight line calibration instead of the actual calibration function to assign the energy value to a given characteristic line should be significantly less than the energy difference between that line and the closest line from another element.

In other words, the assumption of perfect linearity shouldn't lead to erroneous elemental identification.

To express this in mathematical formulation, the maximum x-ray energy E_m to be detected and the minimum energy separation ΔE that needs to be resolved (to differentiate between lines of two different elements) are found in the tables of characteristic x-ray energies. From these values, an estimate of the integral non-linearity is given by

$$L_I \leq 100 \frac{\Delta E}{E_m} \tag{5-9}$$

As an example, replacing E_m with 80.172 keV ($K\beta_2$ line of Au) and ΔE with 0.5 keV (the approximate difference between K-series of elements with $Z < 30$) the value of 0.06% is obtained in Equation 5-9. The main amplifier selected for this work (ORTEC Model 572) had a specified integral non-linearity of less than 0.05%.

5.4.2 Pulse Shaping and Noise Filtering

As mentioned before, measurements performed with the x-ray excitation probes require the acqusition of multiple characteristic x-ray spectra, each with multiple peaks. It is therefore necessary to be able to separate these peaks (lines) with relative ease. This, in turn, requires that the resolution specification arrived at in section 5.2 be observed in the final spectra. The linear amplifier plays a key role in making the attainment of the specified resolution possible. This is explained below.

The signals at the output of the preamplifier are unsuitable for direct measurement not only because of their low amplitude but also because of their shape. As shown before, these signals consist of voltage steps that ride on the tails of the previous ones. If these steps are amplified without further processing, the main amplifier would quickly saturate. Therefore, they should be made to return to the baseline very promptly (this couldn't be done in the preamplifier because it would have required a small-valued feedback resistor - not allowed from the noise standpoint). Also, the information about the energy of the detected radiation is contained entirely in the leading edge of the step: the energy of each event is proportional to the difference between the voltages just after and just before the step. The determination of this difference is accomplished by reshaping the signal in such a way that the measurement of the amplitude is always performed with reference to a fixed baseline (zero volts). Again, a prompt return to the baseline is required after each event so that the following signal may start from zero. In addition, to facilitate the measurement of the amplitude (peak value), it is desirable to have a signal without a sharp maximum (by lingering at the peak value, the signal allows the measuring circuits to determine its amplitude more accurately). These requirements taken together indicate that a desirable signal should have the shape of a pulse: a relatively fast rise, a flat or gently rounded top, and a relatively fast decay. A bell-shaped curve is a fair example of a desirable pulse shape.

Another reason already mentioned for reshaping the preamplifier signals is the need to reduce the effects of noise on resolution. The ideal treatment of noise would be to use a filter that would reject the noise completely, and that would allow the signal to pass unmodified. In the field of communications, where the signals are essentially periodic, it is possible to come quite close to this ideal situation and to extract extremely weak signals from an intense noise background. The reception of transmissions from spacecraft far out in the fringes of the solar system is proof of what can be accomplished in this respect. In nuclear and x-ray spectrometry the situation is not quite as fortunate: Both the signal and the noise are random in time and in amplitude.

The important parameter to be considered in analyzing noise performance is signal-to-noise ratio (SNR). The goal in this respect is to find a filter that will make the SNR as high as possible.

In terms of frequency components, it can be said that the signal, being a single step with a finite rise time, and the noise, being a sequence of small steps of random amplitude and randomly spaced in time, have different Fourier spectra. Therefore, it is plausible to expect that there are filters which improve the SNR. This is indeed the case. The filters that are most effective in improving the

SNR are bandpass filters (filters that strongly attenuate low and high frequency components and have little effect on components within a range of intermediate frequencies).

Interestingly, the networks that realize passband filters and those required to transform steps into pulses are of the same general type. The particular values of the components used in implementing the networks vary from one experimental situation to another. For instance, at extremely low count rates the problem of pulse pile-up can be neglected since the spectral resolution is essentially given by the SNR; therefore, the network that yields the highest SNR should be selected. On the other hand, at high count rates, a network with a lower SNR but which avoids most of the pulse pile-up gives the best overall performance. Therefore, it is important that the parameters of the signal generated by the selected linear amplifier be adjustable by simple front-panel controls. This makes possible the optimization of the system for the different experimental situations that may be encountered.

Here, the discussion of the subject will proceed along the following lines: First, the networks required to obtain a desirable pulse shape will be analyzed, and then the behavior of these networks with respect to the SNR will be discussed.

The first aspect of the problem to be considered is the pile-up of the signals generated by successive events.

As mentioned before, the energy information about the detected events is fully contained in the vicinity of the leading edge of the voltage steps generated by the preamplifier. Therefore, the long tails that follow this leading edge can be suppressed without loss of information. This can be easily accomplished by means of an RC circuit known as a differentiating network (Figure 5-9). If the time constant $T_1 = R_1C_1$ of the differentiating network is much longer than the rise-time of the voltage step (which inpractice is usually the case), the amplitude of the step remains essentially unchanged (no ballistic deficit). This simple type of pulse shaping was used even before the times of nuclear spectrometry; it facilitated the counting of events detected by G-M counters.

The pulse shape obtained with just a single differentiator is far from ideal for pulse-height measurements. The top of single-differentiated signals is too sharp. This makes the accurate amplitude determination very difficult. A simple solution to this problem is to add a second RC circuit; this time with the configuration shown in Figure 5-10a, known as an integrating network with time constant $T_2 = R_2C_2$. The effect of this network on the differentiated signal is to produce a pulse with a rounded top as shown in Figure 5-10c.

The net result of the effects of the two RC networks on the original steps is a signal with approximately the

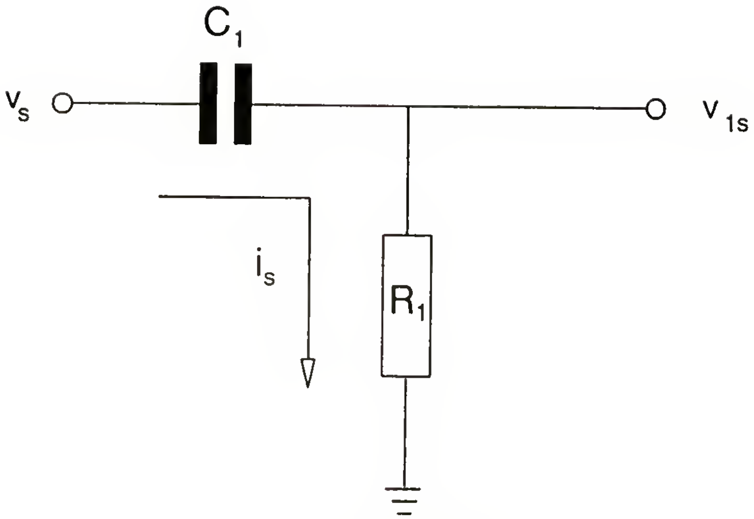

a. Network

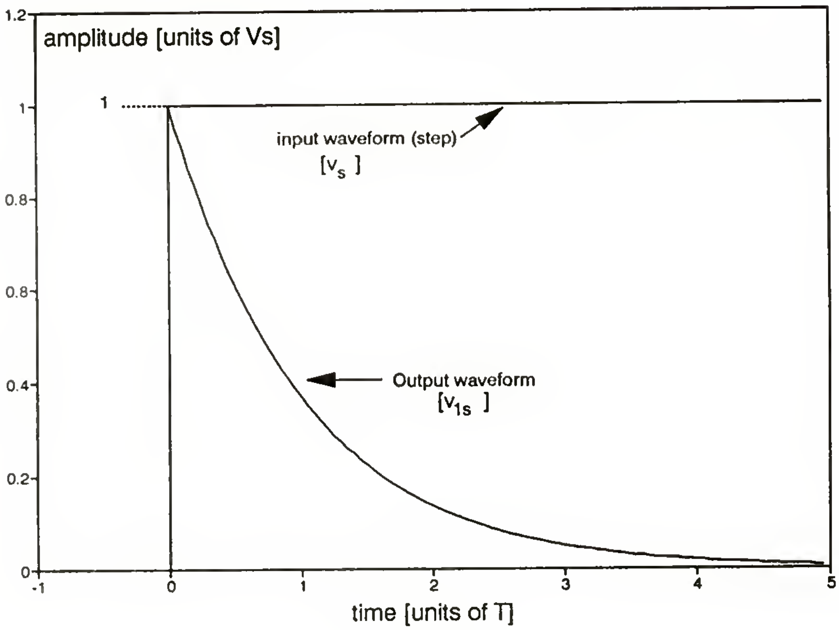

b. Input and output waveforms

Figure 5-9. Differentiating network

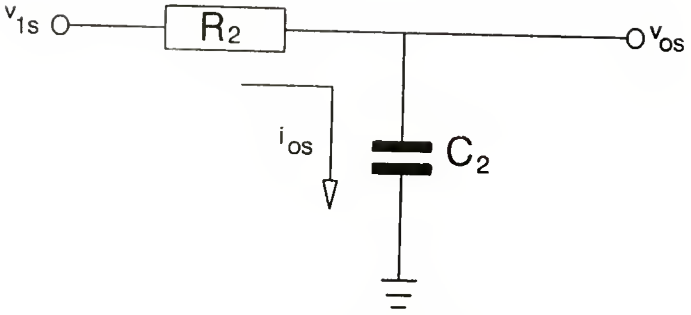

a. Network

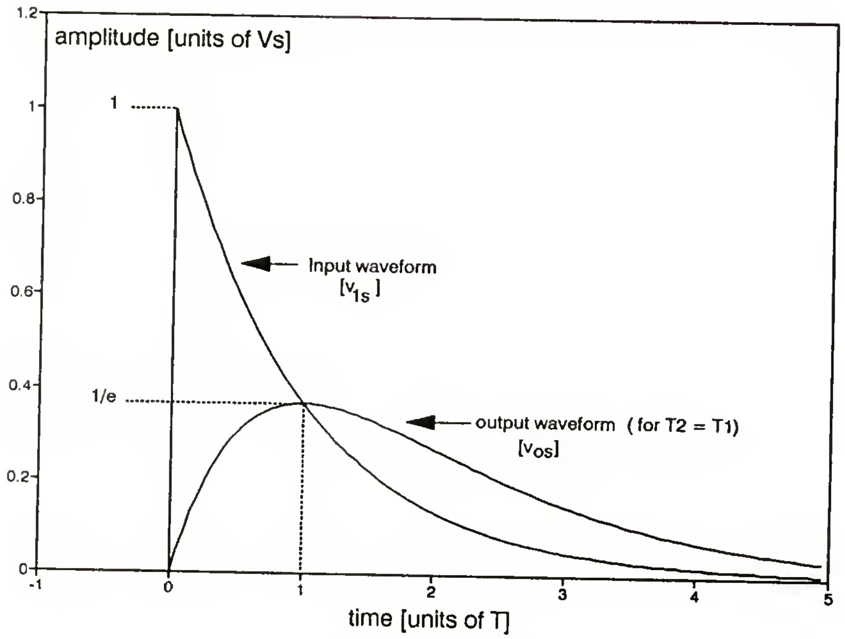

b. Input and output waveforms

Figure 5-10. Integrating network

desired characteristics: Relatively fast rise, approximately flat top, and a fairly rapid return to the baseline.

The differentiating network is so called because its output approximates the derivative of the signal applied to the input terminals. In the field of general electronics this circuit is also called a high-pass filter. The reason for this name is that if a signal with several Fourier harmonics is applied at the input, the network will preferentially attenuate the low-frequency components: The higher the frequency, the lower the attenuation. Very high-frequency components will pass through the network essentially unaltered.

For similar reasons, the second network is called an integrating network or low pass filter: Its output approximates the integral of the input current or, in different words, it preferentially allows the low-frequency components of the signal to pass through.

The mention of filters shifts the discussion to the problem of signal-to-noise ratio (SNR). What is the effect of the pulse-shaping networks on the SNR of the system? For simple RC-shaped signals Gillespie determined that the optimum SNR is obtained when the integrating and differentiating time constants are equal [65].

While this SNR analysis establishes the relative value of the time constants, the absolute value is determined experimentally in each counting situation. Necessarily, for optimum resolution, it is a compromise between count rate and SNR.

At low count-rates, since the pulses are widely spaced in time, the optimum time constant is determined mainly by noise considerations. For x-ray detectors such as the one used in this work the different noise components, each with is own frequency spectrum, cause the optimum shaping constant to be in the order of several microseconds (5 to 10 μs) . At higher count rates the resolution is affected both by the noise and by the incipient pile-up of pulses. Shorter time constants become optimum in these situations (1 to 5 μs).

Although only RC shaping has been discussed, in general the arguments apply equally well to other shaping networks, such as gaussian, $\sin^n$, and quasi-triangular [66]. In every case, for optimum performance the pulses should be longer at low and shorter at high count rates.

RC networks are the simplest used in nuclear amplifiers. Other, more complex, networks such as the ones just mentioned, yield pulses which are more symmetrical with respect to their centroid and which have better SNR, as discussed below.

From the brief discussion of the previous paragraphs, it can be seen that a parameter that is of importance in pulse-height spectrometry is the pulse width. Pulse width has been defined in different ways, but IEEE Std. 301-1988 recommends using the full-width at half-maximum amplitude

($t_{1/2}$) as a measure of pulse width, and calls it shaping index. The question then arises: Is it possible to construct networks that for the same shaping index will yield better noise performance than the simple RC networks described above? The answer is yes, and since the mid-60's when the first gaussian-shaping network amplifier was introduced [67], networks have been used that generate pulse shapes with superior performance to that of the single RC filter.

For the sake of completeness, it should be mentioned that besides the pulse shapes achieved with resistors and capacitors, and even in some cases with inductors, amplifier signals can be shaped with distributed-parameter components such as delay lines. However, delay line-shaped pulses are used only with scintillation counters where the resolution is mainly determined by detector statistics and not particularly affected by preamplifier noise.

Also, the pulse shapes discussed so far are unipolar, i.e. they are all contained within one side of the baseline. Bipolar signals (doubly-differentiated) may be necessary to preserve some reasonable resolution in circumstances of extremely high count-rates.

The selected amplifier (Ortec Model 572) is an instrument designed for the type of high resolution spectrometry required in the multi-element x-ray probe measurements. It has a gaussian pulse shape which yields excellent noise performance. Its shaping indices are front panel selectable for system optimization. Depending on the count rate, the index values used in the measurements were 6 or 10 μs.

5.4.3 Pole-Zero Cancellation

Although the pulse shaping discussed in the previous section accomplishes to a large degree the purposes for which it was introduced (proper shaping of pulses to diminish pile-up effects and noise filtering), in high resolution systems such as the one required for the x-ray excitation probes some subtler undesirable effects must also be considered. One of them is the impact on resolution of the long signal undershoots that in some cases are unavoidable.

As mentioned before, the voltage steps at the output of a pulsed optical feedback preamplifier have perfectly flat tops but those at the output of resistor-feedback preamplifier (such as the one used in this work for the reasons given in section 5.3) have long exponential tails with a time constant $T_f = R_f C_f$. The preamplifier feedback network is actually a differentiating circuit which has the effect of introducing a small undershoot of long duration in the pulse shape at the output of the main amplifier. If a pulse occurs before the undershoot from a previous one has completely disappeared (a very likely occurrence since the undershoot usually last several milliseconds) it will have its amplitude (with respect to the baseline) diminished by the magnitude of the undershoot. This phenomenon causes the broadening of the spectral lines on their low-energy side. The problem is solved by means of the technique known as pole-zero cancellation, devised by Blankenship and Nowlin [63]. It consists of adding a resistor R_{pz} in parallel with the differentiating capacitor C_1. The value of R_{pz} is chosen to introduce a zero in the Laplace transform of the network's transfer function that exactly cancels the pole due to R_fC_f. This modification eliminates the undesirable undershoot.

In actual amplifiers Ry_{pz} usually is a front-panel multi-turn potentiometer that can be adjusted to effect the cancellation for the particular preamplifier being used. The Ortec Model 572 amplifier has the pole-zero cancellation feature. Significant improvement in resolution can be obtained by proper adjustment of the pole-zero cancellation, even at relatively low count rates.

5.4.4 Baseline Restoration

Another problem that becomes noticeable only in high resolution work such as that of multi-element x-ray probes is the effect of baseline-shift caused by ac-coupling at one or more points in the spectrometry system. This is discussed below.

Unless the system is truly dc-coupled from the detector to the ADC, there is another factor that may affect the spectral resolution at medium to high count-rates: Baseline shift.

Any coupling capacitor between modules or stages, no matter how large, will block the transmission of dc-components. Because of this, if a unipolar signal is applied to the input of the system, the output will necessarily show an undershoot. The integral of the output signal over a long period of time remains at zero volts (no dc component). If the differentiating time constant(s) introduced by the coupling capacitor(s) is (are) several orders of magnitude larger than the shaping constants, as it is usually the case, the undershoot of each pulse will be extremely small; actually unnoticeable on a pulse by pulse basis (and un-correctable by PZ-cancellation). However, at higher count rates the cumulative effect of the undershoots will cause the baseline to shift to a negative value until the average voltage is again zero. This effect can be shown by taking a spectrum at low count rate and, without any changes in the equipment settings, acquiring it again at a much higher rate. The second spectrum will appear displaced downwards in energy because of the baseline shift.

In practice, the count-rate from nuclear and x-rays detectors is random about an average value, so the net effect of the baseline shift is a deterioration of the resolution rather than a spectrum displacement.

To alleviate this problem, Robinson designed a circuit known as a baseline restorer (BLR) of which there are several later versions [68]. The basic idea behind BLR's is the following: As long as there are no signals present, the baseline is clamped to zero volts by means of a low impedance (such as a forward-biased diode). When the presence of a signal is detected (by a threshold discriminator, for instance), the clamp is released (by reversing the bias on the diode) and the amplifier operates normally. As soon as the signal decays to within a few millivolts of the baseline, the clamp is re-activated, and the baseline is restored to its original value.

State-of-the-art instruments, such as the amplifier selected for this work, have a front-panel switch that permits to optimize the BLR for the count rates encountered in the experiment.

5.5 The Multi-channel Pulse-height Analyzer

The last step in obtaining an energy spectrum from the ionizing events detected by the germanium crystal consists in measuring the amplitude of the pulses at the output of the linear amplifier by converting this amplitude into a number, and using this number as a memory address to increment a storage register. These functions are performed by the multi-channel pulse-height analyzer (MCA).

Several aspects of an MCA must be taken into account in selecting a unit for multi-element x-ray excitation probe applications. Some of these are basic specifications such as the number of channels and the linearity which have a direct impact on the accuracy and precision of the measurements. Others are features of convenience which facilitate the data reduction needed in x-ray probe work. Both types of requirements will be addressed after some introductory remarks about MCA's in general.

There are three main components in any MCA used in high-resolution spectrometry: A peak detector/pulse stretcher, an analog-to-digital converter (ADC), and an updatable memory.

The function of the peak detector/pulse stretcher is to determine when the incoming signal has reached its maximum value and to temporarily store this value in an analog memory (storage capacitor). This allows sufficient time for the ADC to effect its conversion into a number.

The ADC converts the signal amplitude into a number. In spectrometry work, these numbers are referred to as channels. In state-of-the-art analyzers the signal amplitude is usually assigned to one among up to 8,192 (8k) channels. MCA's are commercially available with capacities from 1k to 16k channels.

In gamma-ray work, 4k- or 8k-channel analyzers are the most common types. In x-ray spectrometry 1k or 2k channels are usually sufficient. The number of channels required in the analyzer is determined by the maximum energy to be analyzed and the resolution of the detector. As mentioned above, the section of the analyzer responsible for assigning a signal to a particular channel is called an analog-to-digital converter (ADC). This is discussed below.

The analog signal is applied to the input of the ADC and its output delivers a number directly proportional to the signal amplitude. There are many schemes that can be used to effect this conversion. In the past, the ramp or Wilkinson type ADC was used almost exclusively for spectrometry work because of its excellent integral and differential linearities. In an ADC, integral non-linearity is defined as before and differential non-linearity can be conveniently defined as channel-width non-uniformity. While integral linearity is fairly simple to achieve with several types of converters, the degree of differential linearity required in spectrometry systems is more easily obtained with Wilkinson-type ADC's. For this reason they have been the preferred type in the past, as mentioned above. However, because ramp converters are rather slow, sometimes they impose unacceptable upper limits to the pulse acquisition rate (through-put). For this reason, other types of ADC's, such as the successive approximations type, have been perfected and are widely used today.

After the analog signal has been converted into a number, this number is used as a memory address. Every time a signal of a particular amplitude is processed, the corresponding memory address (channel) is incremented by one count. In this manner the spectrum is accumulated in memory with the address corresponding to pulse amplitude (energy) and its contents to number of counts (intensity).

5.5.1 Determination of the Required MCA Specifications

5.5.1.1 Number of channels

The MCA channel capacity required for the multi-element x-ray excitation probes is determined by the system resolution and by the maximum photon energy to be detected, in the following manner.

The best resolution attainable with the system is approximately 200 eV fwhm (see section 5.2). For ease of peak identification it is desirable to include at least five channels within the fwhm, particularly during the spectrometer setting-up procedure. This results in a channel width of 40 eV.

As mentioned before, the maximum photon energy to be detected is approximately 80 keV. Therefore, the required number of channels is:

$$Required\,number\,of\,channels = \frac{80keV}{40eV} = 2000 \qquad (5\text{-}10)$$

5.5.1.2 Integral non-linearity

The integral non-linearity requirement is established by the criterion that all x-ray spectrometer components must contribute approximately equally to overall system non-linearity. From the discussion on main amplifier integral non-linearity, it follows that in the MCA this specification should be approximately 0.05%.

5.5.1.3 Differential non-linearity

The manner in which the requirements for a certain value of ADC differential non-linearity is specified is an ill-defined procedure. Probably there is not a single best way of arriving at a differential non-linearity target specification starting from experimental variables. Part of the problem stems from the fact that differential non-linearity itself is ill-defined. Without going into details beyond the scope of this discussion, a hypothetical (albeit extreme) example is presented below that illustrates the difficulty of a rigorous treatment of differential non-linearity.

Assume that the differential non-linearity is defined in terms of channel width non-uniformity, that a 1k ADC is used, and that its maximum differential non-linearity is 1% (i.e., any channel width is within ±1% of the average channel width).

Signals whose amplitude varies randomly over the full dynamic range of the ADC are applied to the input.[1] The system is allowed to run until an average of 10^5 counts per channel are accumulated. If the channel-width variations (within 1% of the average) are randomly distributed among all the channels, they would be undetectable since they would fall within the statistical uncertainty (a maximum of about three standard deviations from the mean number of counts uniformly distributed throughout the spectrum).

---

[1] This in itself is not easily accomplished. It could be approximated with the flat region of a compton continuum. However, the difficulty in obtaining a suitable test spectrum to measure differential non-linearity gives an idea of the complexity of the task.

However, if most of the channels have essentially the same width (variations much less than 1%) and the differential non-linearity of the instrument is concentrated in a small cluster of contiguous channels, the acquired spectrum may show an irregularity riding on the continuum which may be mistaken for a weak peak if the non-linearity is of positive sign or, in the opposite case, an actual peak may be masked by the localized non-linearity.

In practice, the difficulties of arriving at a precise determination of a specification for differential non-linearity are circumvented by experience. Empirically, it is found that a one-percent differential non-linearity causes little (if any) difficulty in nuclear and x-ray spectrometry. This is true, for instance, in the case that the criterion for an upper limit of differential non-linearity is specified in terms of minimum detection capabilities of multi-element x-ray excitation probes. Unless the probe is used in an environment with unrealistically high background radiation, or if a measurement is ran for an impractically long time, the specification of one-percent differential non-linearity should not be the limiting factor for minimum detection capability.

5.5.1.4 Features of convenience

Other analyzer features are discussed below. These are not indispensable for the method of determination of spatial particle density distribution presented in this work but they facilitate the acquisition and reduction of data.

In multi-element x-ray excitation probes applications it is necessary to identify the energy of the different lines to establish their correspondence with the target elements and hence with their point of origin. Therefore, it should be possible to calibrate the MCA used for this task in terms of photon energy. In addition, the instrument must have the capability of so labeling the horizontal axis of the displayed and printed-out spectra.

The analyzer should also have the capability of being calibrated in energy by means of two or more peaks of known energies. This implies that it should be able to determine a properly defined peak centroid, and to indicate the energy of any selected peak (peak identification).

The intensity (number of counts) of any given line is a measure of the particle density at the target location. Therefore, the analyzer should be able to integrate the counts under a selected peak or within given regions of interest and display or print out the results.

From time to time, it may be necessary to measure the resolution of the detector. Means of performing this task in a semi-automated manner are also a desirable feature.

From previous experience with similar spectrometry systems, it was concluded that the following additional MCA capabilities would greatly facilitate the work, particularly in the development stage of the system: capability of logarithmic and several ranges of linear display, horizontal spectral expansion and roll, and preset live time or counts.

Finally, to provide the means for permanent spectra storage for archival purposes and transfer of the data to other processing equipment, the MCA should have the ability of communicating directly with digital computers.

5.5.2 Specifications of the Selected Analyzer

The MCA selected for this work was the Ortec ADCAM® ACE™ Model 916-2k. This MCA is built on a PC-mounted card. The information (spectrum) stored in the MCA memory can be transferred to the host computer memory for data processing and display, or can be stored on disk for transfer to a different machine.

The pertinent specifications of this instrument, which fulfills all the requirements discussed above, are listed below:

Number of channels: 2k
Dead time: 25 μs
Integral non-linearity: <±0.05%
Differential non-linearity: <±1%

5.6 System Integration

The HPGe detector and the electronic modules discussed in this chapter were integrated into the system shown in Figure 5-11. In addition to the instruments described above, the system included a high voltage power supply to bias the detector (Ortec Model 459), a NIM bin and power

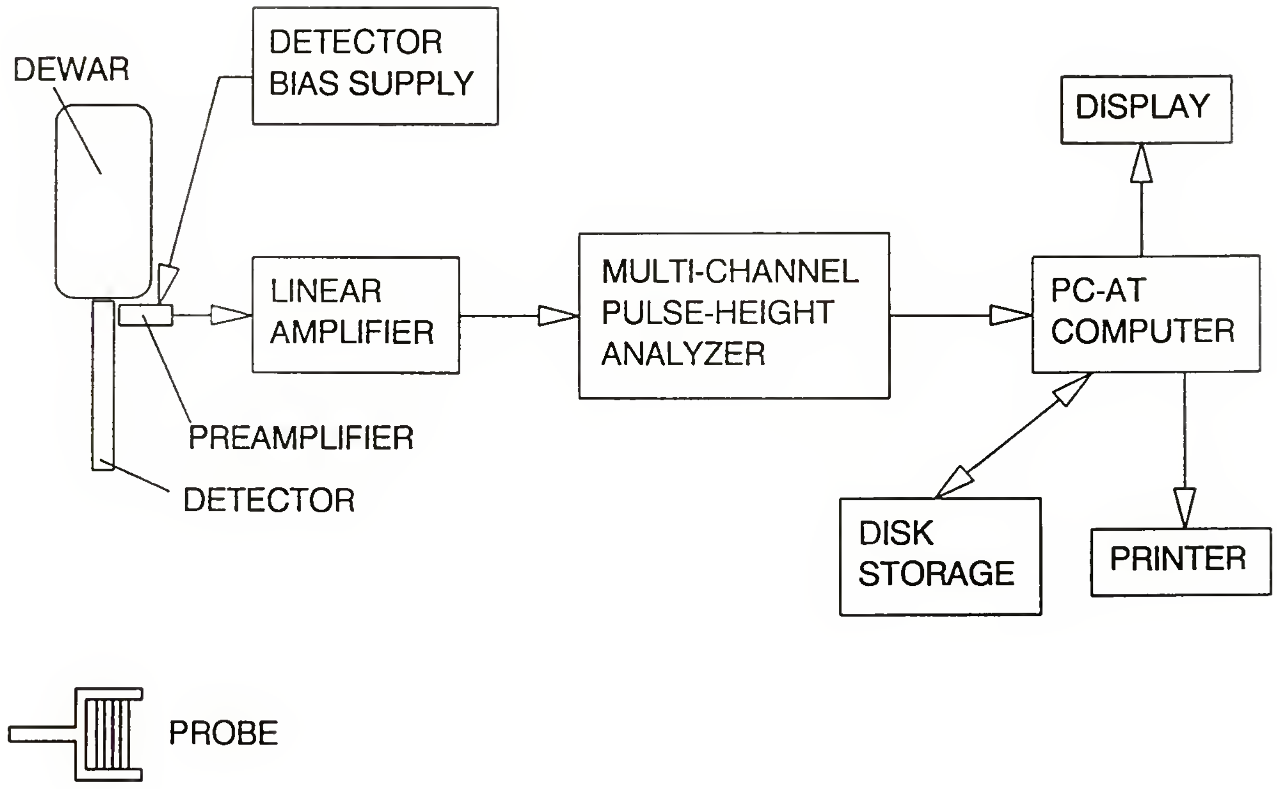

Figure 5-11. System block diagram

supply (Ortec Model 4001M), a detector temperature monitor (Fluke Model 82 multimeter), and a PC-AT computer with hard disk drive and printer.

CHAPTER 6
MEASUREMENT OF SPATIAL PARTICLE DISTRIBUTIONS USING THE MULTI-ELEMENT X-RAY EXCITATION PROBE

In any of the applications of the x-ray excitation probes, such as particle flux or density determinations, the measured quantities are the number of detected x-rays X_d and the solid angle of detection ω. As shown in Equation 4-14, these two quantities are combined with the specific detected photon yield Y_{sd} to obtain the number of incident particles P_i. Y_{sd}, in turn, can be computed with Equation 4-13 from published values of the particle range R and the x-ray production cross section σ_x. However, as pointed out by Mitchell and Ziegler, the reliability of the measured values of σ_x is sometimes questionable [41]. For this reason it is preferable to determine Y_{sd} with Equation 4-12 (reproduced below as Equation 6-1) from measured values of X_d, ω, and P_i:

$$Y_{sd} = \frac{X_d}{P_i \omega} \tag{6-1}$$

In addition, the value of Y_{sd} is strongly dependent on the target geometry. Therefore, the values of X_d and P_i should be measured in experimental conditions as close as possible to those found in actual determinations of particle density or flux.

Details of the calibration method are discussed in the following sections of this chapter, and actual calibration of probes[1] with laminiform and filiform geometries using the University of Florida Van de Graaff accelerator are given as examples of the technique. Later, examples of actual beam profile measurements and of measurements of neutralized beams are shown to illustrate applications of the x-ray excitation probes. In Chapter 7, computation of Y_{sd} for several probe configurations are presented.

Before leaving this introduction, it must be noted that the difficulty just mentioned of using computed values of Y_{sd} to calibrate the probes has a parallel in the traditional mode of using characteristic x-ray emissions in elemental analysis applications. There as well as here, the more it is known a priori, the more information it is possible to extract from the measurements. To achieve high accuracy in elemental analysis using x-ray spectroscopy it is necessary to calibrate the system with standards whose characteristics (mix of elements, physical form, etc.) are as close as possible to those of the sample under analysis. Similarly, as indicated above, for reliable determination of energetic particle flux using x-ray excitation probes, it is necessary to calibrate them in experimental conditions which closely duplicate those of the actual measurements.

---

[1] In this chapter, the expressions "measurement of Y_{sd}" and "calibration of the probes" are used interchangeably.

In this work, values of Y_{sd} were determined from experimental measurements of X_d, ω and P_i whenever possible. As discussed later, in the case of very thin targets (thinner than the range of the particles) it was not possible to determine P_i from direct measurement of the current. In these cases, the value of Y_{sd} was computed with Equation 4-13 and these computations are shown in the following chapter.

6.1 Calibration Facility

6.1.1 The Van de Graaff Accelerator and the Beam Line Used in the Measurements

The experimental part of this work (calibration of the x-ray excitation probes, determination of beam profiles, and measurement of partially and completely neutralized particle beams) was performed using the facilities of the University of Florida Van de Graaf accelerator (VDG). The facility is located in the Nuclear Engineering Sciences building, at the main campus of the University, in Gainesville, Florida. The accelerator is a High Voltage Engineering Corporation Model KN-4000.

The accelerating section is built in a vertical configuration with the ion source at second-story level. The high-voltage components and the beam tube are enclosed in a tank of pressurized nitrogen. The beam tube exits at first-floor level and continues into the basement, where the experimental facilities are located. As the beam tube passes through the space between the two coils of an electromagnet (analyzing magnet), it is bent 90° and emerges horizontally. The function of the analyzing magnet and its entrance and exit slits is to select particles of the desired energy; a more detailed explanation is given in the next section. From this point, the beam tube extends for about 1.5 m to the switching magnet. The function of the switching magnet is to steer the beam to the selected experimental line. All the experiments performed in this work were done on the north line of the accelerator. The first section of the experimental lines end shortly after the beam tube exits the switching magnet. At that point an isolation valve is installed on each line; the isolation valve remains closed at all times except when the beam is in use. After this valve, the section of the beam line specifically designed and built for the multi-element x-ray probe measurements was installed. A diagram of the line showing its main components is shown in Figure 6-1.

The first component of the experimental line was a multi-port section (BDA[1]) in which a linear motion device

---

[1] BDA stands for beam diagnostic assembly, a section of the beam line with multiple access ports through which a variety of probes, neutralizing foils, and apertures can be inserted and placed in the beam path.

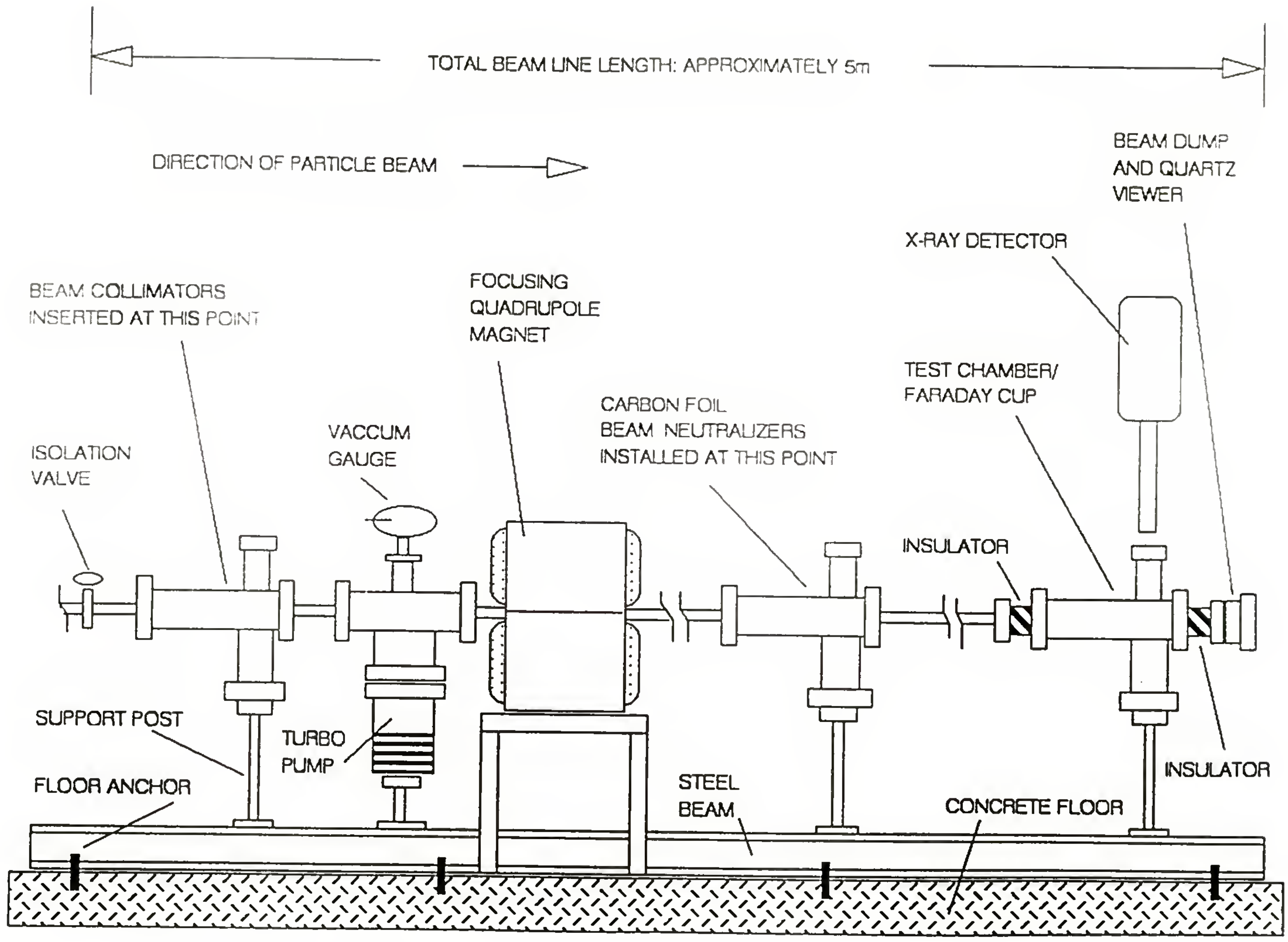
TOTAL BEAM LINE LENGTH: APPROXIMATELY 5m
DIRECTION OF PARTICLE BEAM
BEAM DUMP AND QUARTZ VIEWER
X-RAY DETECTOR
BEAM COLLIMATORS INSERTED AT THIS POINT
FOCUSING QUADRUPOLE MAGNET
TEST CHAMBER/ FARADAY CUP
CARBON FOIL BEAM NEUTRALIZERS INSTALLED AT THIS POINT
VACCUM GAUGE
ISOLATION VALVE
INSULATOR
SUPPORT POST
TURBO PUMP
INSULATOR
FLOOR ANCHOR
STEEL BEAM
CONCRETE FLOOR

Figure 6-1. Simplified diagram of the experimental beam line.

(LMD) with an aluminum plate with a series of apertures of various sizes was installed. The main function of these apertures was to adjust the target current without modifying the accelerator settings. The different size apertures afforded an effective method of accomplishing this task because at this point the unfocused beam has a large cross section (~ 2 cm^2) which can be easily collimated. The experimental line had its own vacuum system consisting of rotary vane and turbo-molecular pumps. The main pumping station was located immediately after the first BDA. Pressures of the order of 10^{-7} torr at the pumping station and 10^{-5} torr at the far end of the line were routinely attained. The pressure on the accelerator side of the isolation valve was maintained at approximately 10^{-6} torr by the accelerator's own vacuum system. A short distance after the pumping station, a focusing quadrupole magnet was used to create an image of the exit slit at the location of the target.

Approximately one meter after the focusing magnet, a second BDA was installed to provide means of introducing carbon foils for beam neutralization.

A third BDA was installed at the far end of the line to serve as experimental chamber and Faraday cup. The line was terminated with a short beam dumping section.

The experimental line was built of sections of stainless steel tubing connected by metal-to-metal (Conflat[1]) vacuum-sealed couplings. It was supported by adjustable-height vertical steel posts resting on a 4-in by 4-in steel I-beam which was attached to the concrete floor by captive fasteners.

Aluminum apertures 0.5 in in diameter were installed at several points in the line to stop particles that for any reason may have followed secondary trajectories. Some of these particles may be ions neutralized by the remnant gas before the focusing quadrupole magnet, others may be secondary particles generated by collision of ions with line components. Three of these apertures were particularly important: two at the ends of the Faraday cup and one at the entrance to the beam dump. The purpose of the former was to avoid the escape of secondary electrons produced by impact of the beam on the target, and that of the latter was to prevent electrons similarly produced in the beam dump from reaching the Farady cup. In both cases, the ultimate aim was to reduce the errors on the measurement of P_i caused by secondary electrons.

At the far end of the line a fused silica disk was installed for alignment and focusing by visual observation of the fluorescent spot produced in the quartz by the energetic particles. An additional glass window at the end of an oblique port of the BDA permitted viewing of the target when required for alignment. The port immediately above the target was closed with a 0.004-in Mylar[1] window which minimized x-ray attenuation (see Appendix A). The detector was mounted directly above this window. Figure 6-2 shows this arrangement.

---

[1] Conflat is a trademark of Varian Associates.

The x-ray spectrometry system and the quadrupole magnet power supplies were located in the immediate vicinity of the experimental chamber near the end of the beam line for easy access when adjusting the beam and performing the measurements.

6.1.2 Energy and Current Calibration of the Van de Graaff Accelerator

The calibration of the multi-element x-ray probes consists in measuring the specific detected photon yield Y_{sd} as a function of the initial particle energy E_0. The way in which Y_{sd} varies with E_0, which is similar to that with σ_x, is given by Equation 4-13. As mentioned in Chapter 4, σ_x is a rather strong function of the particle energy. Therefore, for accurate correlation of Y_{sd} and E_0 it is necessary to know E_0 accurately. The nominal energy of the particles delivered by the accelerator is found in tables and graphs kept in the control room. The energy values are given as a function of the setting of the analyzing magnet (see below). However, the investigators using the facilities are warned that these values are nominal; they should only be used as a

---

[1] Mylar is a trademark of the Dupont Corporation.

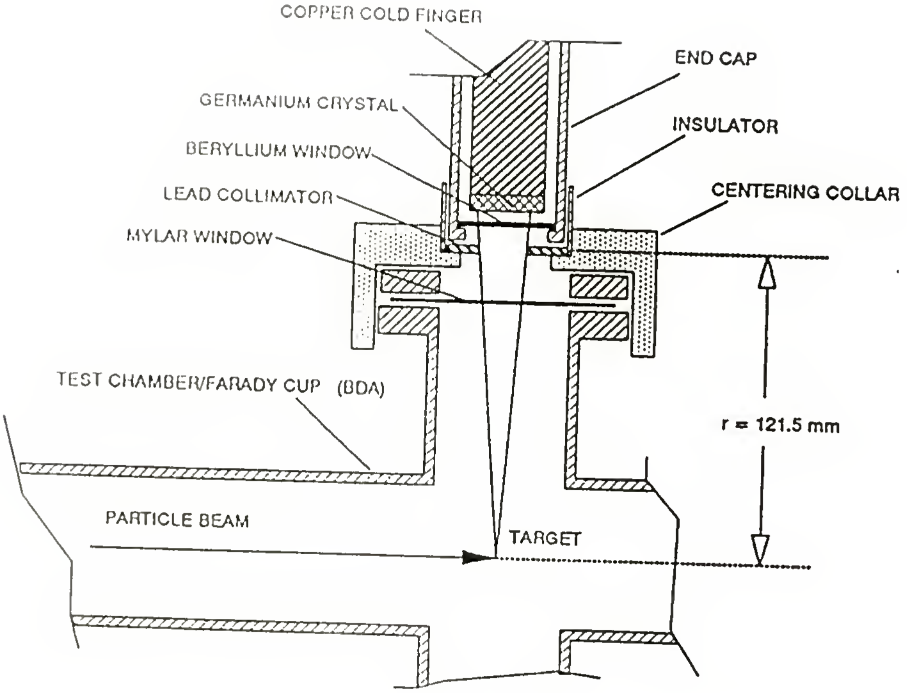

Figure 6-2. Diagram of the target-detector geometry

guide in setting up the accelerator but not in computations where the beam energy is a critical parameter. For these reasons it was decided to perform an independent energy calibration of the accelerator as described in this section.

In addition, the number of particles which strike the target P_i also needs to be known accurately for an accurate determination of Y_{sd}. P_i is measured by integrating the charge collected by the target. The instrument used for this purpose was a Brookhaven Instruments Model 1000 Current Integrator (BIC 1000).

Inquiries made with the operating personnel of the Van de Graaff accelerator revealed that although the accuracy of the BIC 1000 is specified as 0.1%, its calibration had not been checked for several years. Therefore, it was decided to verify it at least within the accuracy afforded by instrumentation available in the department.

6.1.1.1 Energy calibration

The energy of the particles in the beam of electrostatic accelerators is computed from the value of the magnetic field in the analyzing magnet B and from the magnet constant k. The value B is measured with an NMR magnetometer, and k was determined by the procedure described here. The value of the constant k is different for different particles; in this work, the value of k for protons was determined from the relationship between the indicated values of the magnetic field and known proton energy values. The indicated magnetic field values were those read from the NMR magnetometer display in the control console of the accelerator. The proton energy values were determined by locating five resonances of the $^{27}Al(p,\gamma)^{28}Si$ reaction. [69,70] The results were averaged, and the value of k thus obtained was $1.010 \pm 0.004 \times 10^{-4}$ kev/Gs^{-2}. The obtained value of k is in agreement (within the experimental error) with the value obtained in a previous independent measurement by another investigator [71].

The particle energy produced by an electrostatic accelerator is determined primarily by its terminal voltage. Ideally, the beam is monoenergetic, but in fact a distribution of energies is observed. To reduce the spread striking the target, an analyzing magnet is employed to select the central fraction of the original distribution, which operates as follows: the magnet produces a uniform field oriented perpendicular to the path of the particles, causing the beam to bend along a circular path. A collimating slit at the entrance of the assembly restricts the width of the entering beam, and a second one restrict the width of the exit beam. Only those particles will pass through both slits that satisfy Equation 6-2.

$$E_o = \left(\frac{qR}{2M}\right) B^2 \qquad (6\text{-}2)$$

where E_o = energy

q = charge

R = radius of the circular trajectory

M = mass

B = magnetic field strength

To select particles of a given energy, the accelerator terminal voltage is adjusted first, then the strength of the field in the analyzing magnet.

For a given type of particle, all the quantities within the parentheses are fixed and can be replaced by a single constant k:

$$k = \frac{qR}{2M} \tag{6-3}$$

Where the symbols correspond to those in Equation 6-2. Thus, Equation 6-2 becomes

$$E_o = kB^2 \tag{6-4}$$

and by rearranging terms,

$$k = \frac{E_o}{B^2} \tag{6-5}$$

In this form, the constant k is known as the "magnet constant" because it relates the particle energy to the strength of the magnetic field. The determination of k for proton beams is the subject of this section.

From Equation 6-3, an expression that gives values of k for other particles can be derived:

$$k' = k\frac{q'M}{qM'} \tag{6-6}$$

where q' and M' are the charge and the mass, respectively, of the particle for which the value of k' is desired.

6.1.1.2 Method

An aluminum target is bombarded by the beam of protons from the accelerator, causing γ-rays to be emitted via the reaction $^{27}Al(p,\gamma)^{28}Si$. Resonances occur at the energies listed in Table 6-1. Experimentally, they are located by slowly increasing the energy of the protons while observing the γ-ray count rate, which suddenly increases when a resonance occurs.

The proton energy is selected as described before. Having established proton energy and field strength at resonance, the k in Equation 6-4 can be calculated from Equation 6-5.

6.1.1.2.1 Experimental procedure, measurements and results. Figure 6-3 shows the experimental arrangement. The target was an aluminum foil approximately 3 mm thick, thick enough to stop the most energetic protons used in the measurements. The γ-rays produced in the reaction slightly exceeded the span from 1 to 14 MeV.

Table 6-2 shows the energy levels of ^{28}Si, and Figure 6-4 shows the spectrum acquired with the 5" x 5" NaI(Tl) detector used in this work.

The expression "gamma count" used throughout this report refers to the integrated spectrum from ≈4 to ≈12 MeV [67].

The measurement procedure comprised two parts:

First, several of the resonances were located by starting at a low value of the magnetic field and increasing

Table 6-1
Resonances in the $^{27}Al(p,\gamma)^{28}Si$ reaction
(between 800 and 1200 keV)

Proton energy at resonance, E_o [keV]	NOTES
885.0 ± 2	-----
922.6 ± 0.2	Used in this calibration
937.2 ± 0.2	Used in this calibration
991.88 ± 0.04	Used in this calibration
1002.1 ± 0.5	-----
1025.0 ± 0.2	Used in this calibration
1089.8 ± 0.2	-----
1097.6 ± 0.5	-----
1118.4 ± 0.2	Used in this calibration
1171.9 ± 0.3	-----

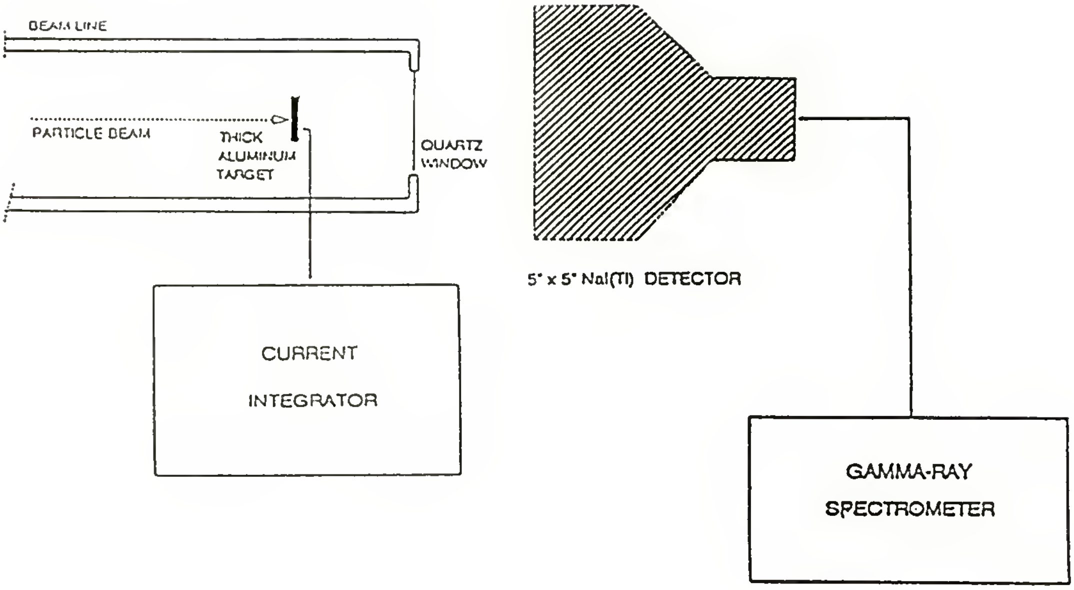

Figure 6-3. Experimental arrangement for the energy calibration of the Van de Graaff accelerator

Table 6-2
Energy levels of ^{28}Si

[keV]	(continued)
1 788.88 +/- 0.09	9 930 +/- 7
4 617.8 +/- 0.2	10 179.8 +/- 1.6
4 979.1 +/- 0.5	10 210.0 +/- 0.8
6 276.5 +/- 0.2	10 275 +/- 3
6 691.4 +/- 0.4	10 377.1 +/- 1.0
6 878.6 +/- 0.3	10 418 +/- 2
6 888.8 +/- 0.5	10 540 +/- 3
7 380.7 +/- 0.4	10 594.4 +/- 1.3
7 417.3 +/- 0.4	10 668 +/- 5
7 798.8 +/- 0.4	10 724.6 +/- 1.3
7 933.4 +/- 0.4	10 901 +/- 3
8 259.4 +/- 0.6	10 915.7 +/- 1.3
8 328.3 +/- 0.9	10 945 +/- 3
8 413.3 +/- 0.3	11 077.5 +/- 1.3
8 542.9 +/- 0.9	11 148 +/- 7
8 588.9 +/- 0.6	11 298 +/- 3
8 903.5 +/- 0.7	11 418 +/- 10
8 944.8 +/- 0.7	11 432 +/- 2
9 163.9 +/- 0.6	11 445 +/- 3
9 316.1 +/- 0.5	11 517 +/- 3
9 381.2 +/- 0.6	11 585 +/- 3
29 418.1 +/- 0.7	11 659 +/- 3
9 480.4 +/- 1.5	11 669 +/- 3
9 497.3 +/- 0.9	11 780 +/- 3
9 702.3 +/- 0.8	Several
9 761.5 +/- 1.4	15 224 +/- 3

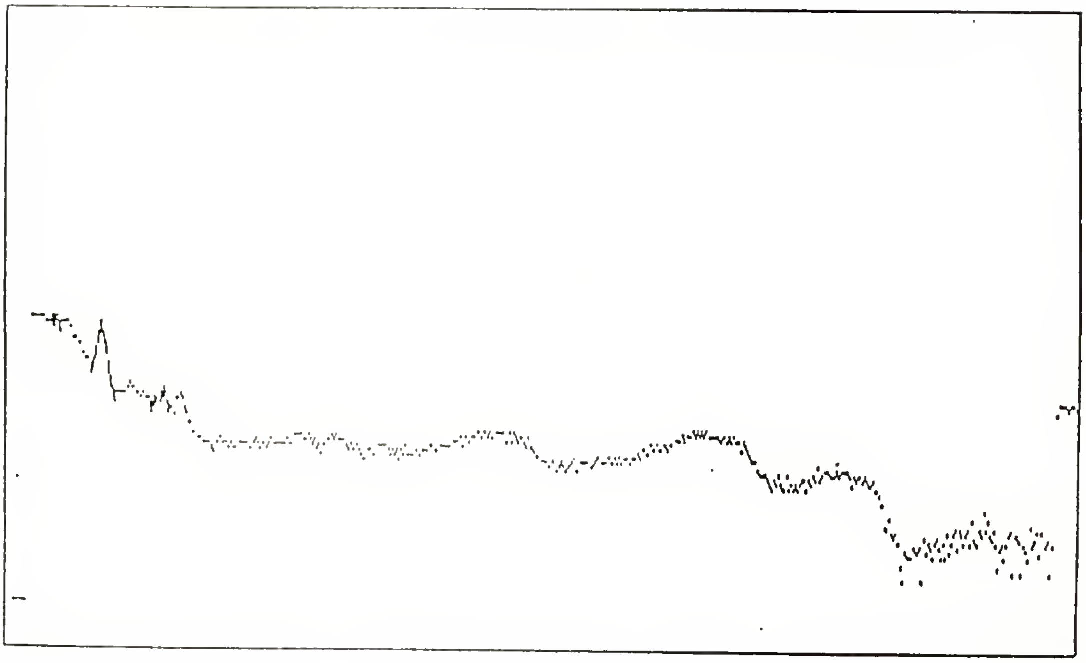

Figure 6-4. Gamma-ray spectrum of ^{28}Si acquired with a 5-inch x 5-inch NaI(Tl) detector. The horizontal scale (energy) ranges from zero to approximately 14 MeV. The vertical scale (counts) is logarithmic

it in steps of ≈100 Gs,[1] corresponding to increments of ≈70 keV. The resonances, which manifested themselves as sudden increases in the gamma count, were matched with known values of the resonance energy (Figure 6-5). Second, the five resonances shown boldfaced in Table 6-1 were chosen for making precise correlations with known values of the magnetic field (Tables 6-3 through 6-7 and Figures 6-6 through 6-10). The averaged value of k and the averaging procedure of these measurements are shown in Table 6-8.

In all the measurements, an effort was made to remain on the same leg of the magnet's hysteresis curve by incrementing the field in only the positive direction. However, from unrecorded measurements it appears that the actual field seen by the particles was independent of the direction of approach --no significant error was introduced in those few instances when the desired values were overshot, then arrived at by backtracking.

Details of the experimental steps and of the calculation of k follow.

1. Starting from a low magnetic field, its value was slowly increased until the desired resonance was approached.

---

[1] Although it would have been preferable to use SI units throughout this work to be consistent with current practice, for this section it was decided to use gauss (Gs) for the magnetic field of the analyzing magnet. Because the NMR magnetometer in the control console of the accelerator is indicated in these units, it was felt that the use of tesla (T) would have led to confusion.

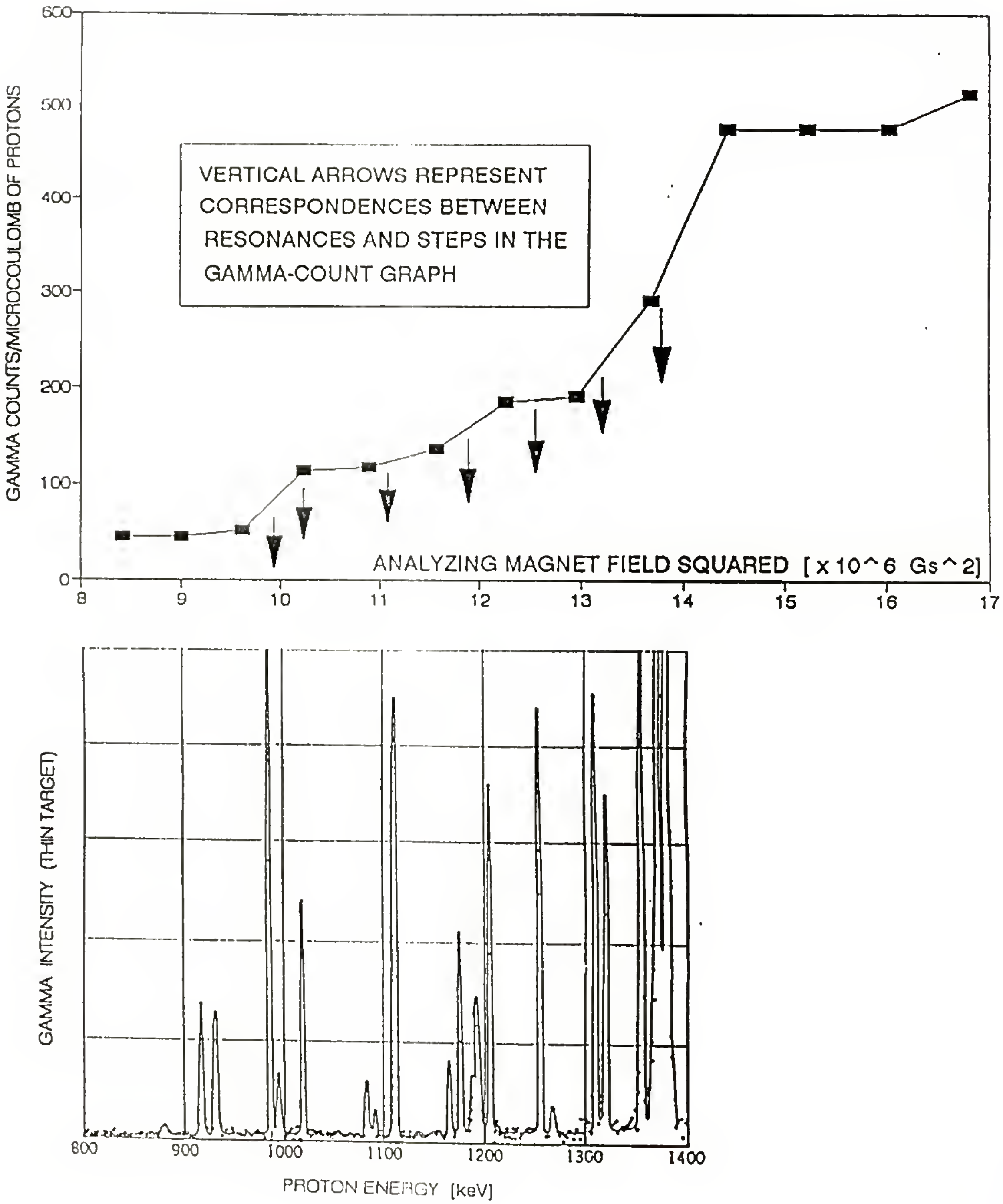

VERTICAL ARROWS REPRESENT CORRESPONDENCES BETWEEN RESONANCES AND STEPS IN THE GAMMA-COUNT GRAPH

Figure 6-5. Correspondence between steps in the gamma-count graph with resonances in the $^{27}Al(p,\gamma)^{28}Si$ reaction

Table 6-3
Data for the determination of k
at the 922.6 keV resonance

Analyzing magnet setting [Gs]	Total gamma-ray intensity [counts/microcoulomb]
3000.76	48.2
3010.28	49.0
3015.29	47.4
3018.79	46.3
3021.79	48.7
3024.79	52.1
3027.30	53.1
3030.30	54.1
3033.30	53.8
3035.30	53.8
3042.30	55.2

Table 6-4
Data for the determination of
k at the 937.2 keV resonance

Analyzing magnet setting [Gs]	Total gamma-ray intensity [counts/microcoulomb]
3040.30	55.2
3042.30	55.6
3044.30	54.8
3046.30	55.9
3048.80	58.7
3050.30	59.1
3052.81	58.3
3054.80	58.7

Table 6-5
Data for the determination of
k at the 991.88 keV resonance

Analyzing magnet setting [Gs]	Total gamma-ray intensity [counts/microcoulomb]
3050.29	58
3100.30	58
3120.80	57
3132.80	79
3140.31	111
3150.31	113
3160.80	113
3170.80	111
3180.81	111

Table 6-6
Data for the determination of
k at the 1025.0 keV resonance

Analyzing magnet setting [Gs]	Total gamma-ray intensity [counts/microcoulomb]
3170.80	111
3180.81	111
3190.31	119
3200.80	119

Table 6-7
Data for the determination of
k at the 1118.4 keV resonance

Analyzing magnet setting [Gs]	Total gamma-ray intensity [counts/microcoulomb]
3300.80	124
3310.80	124
3320.32	124
3330.32	144
3340.32	152
3350.32	144
3350.82	146

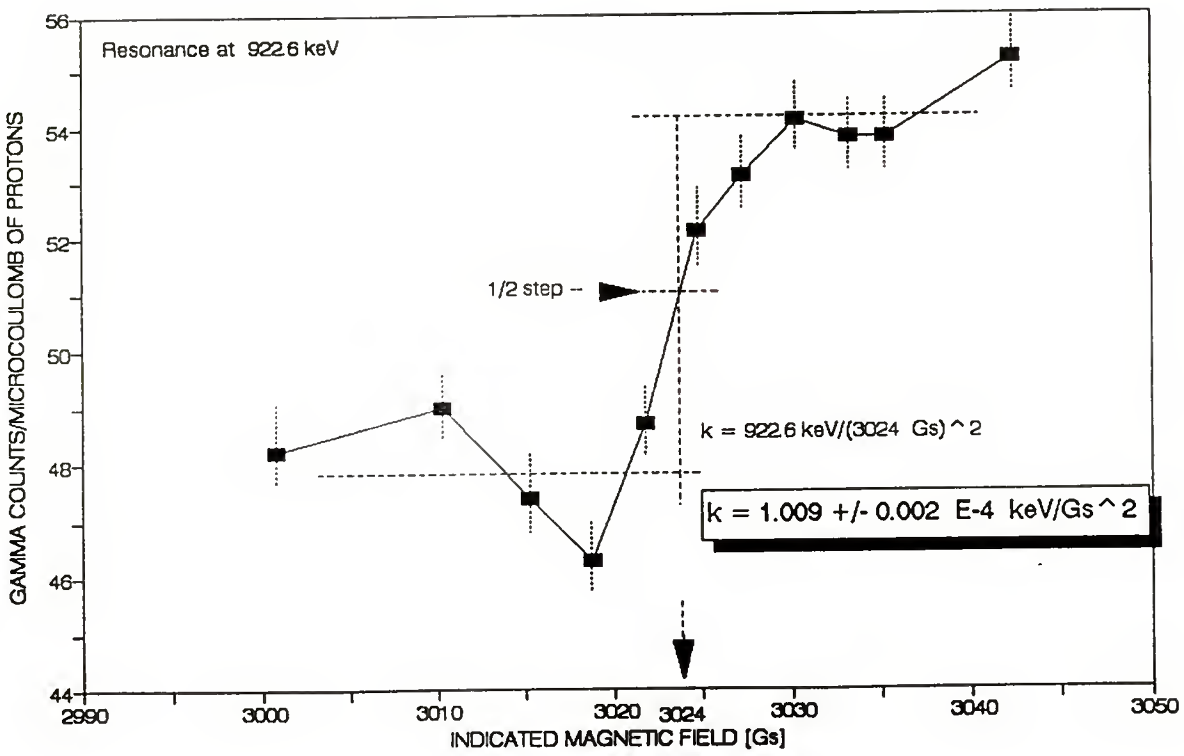

Figure 6-6. Determination of k at the 922.6 keV resonance

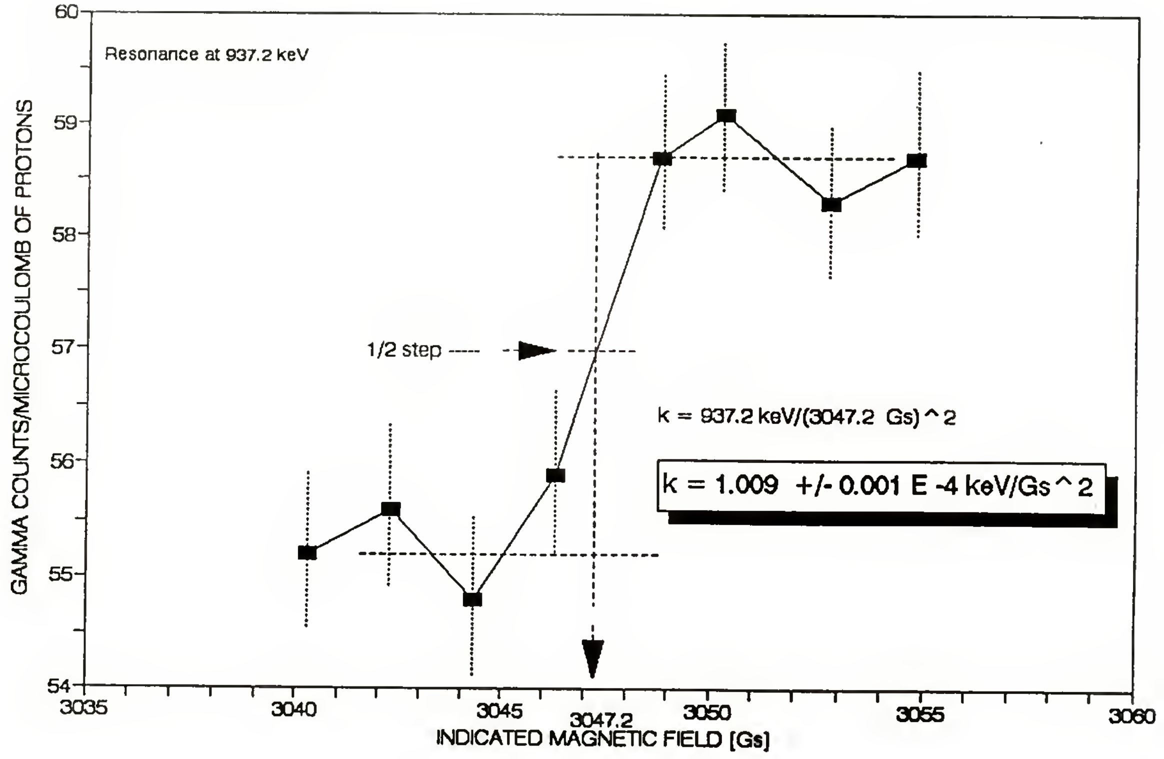

Figure 6-7. Determination of k at the 937.2 keV resonance

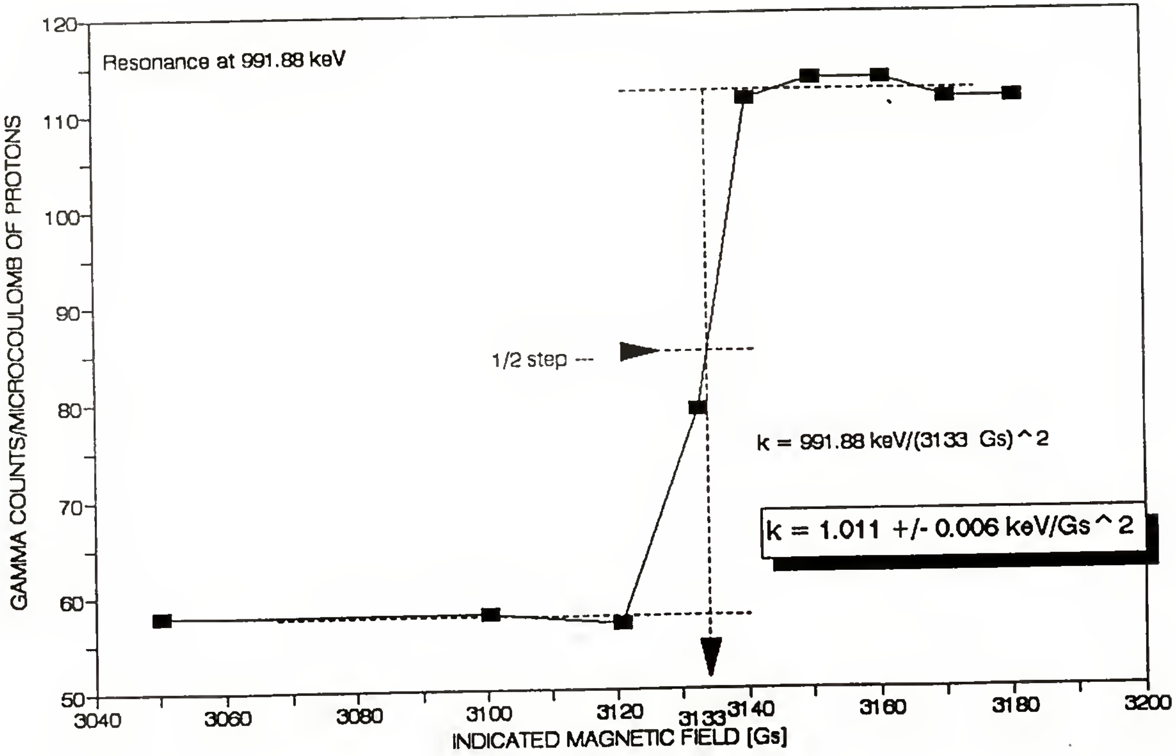

Figure 6-8. Determination of k at at the 991.88 keV resonance

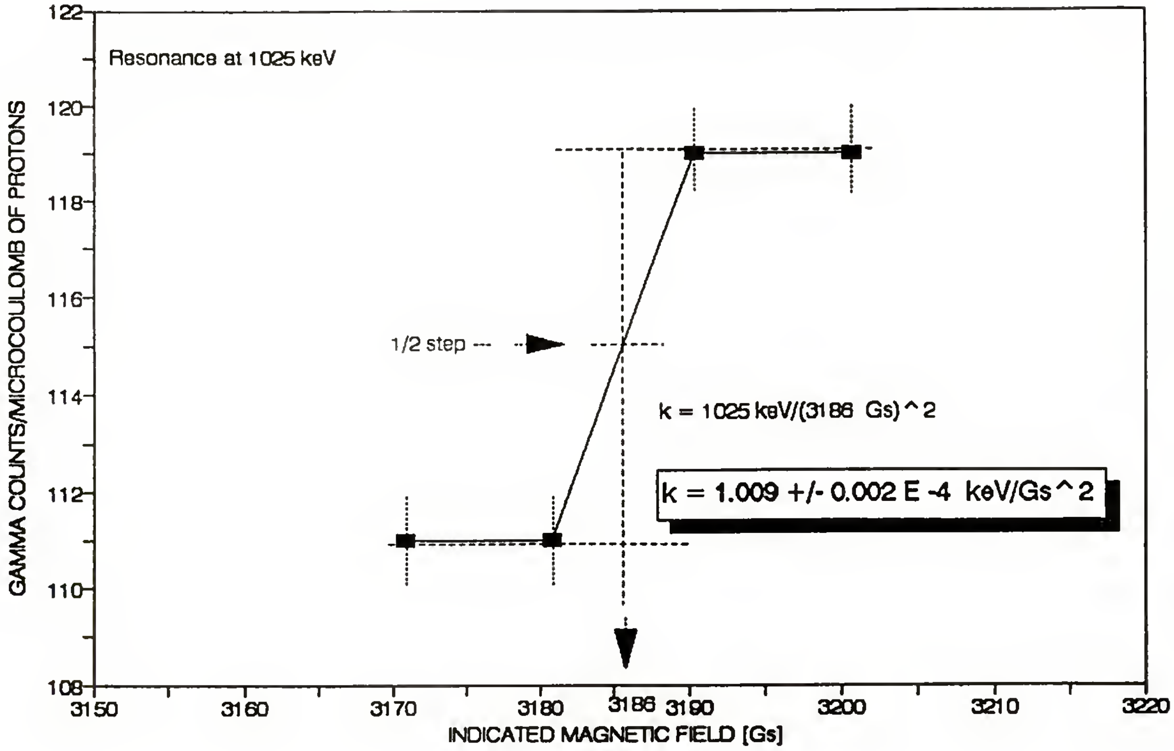

Figure 6-9. Determination of k at the 1025.0 keV resonance

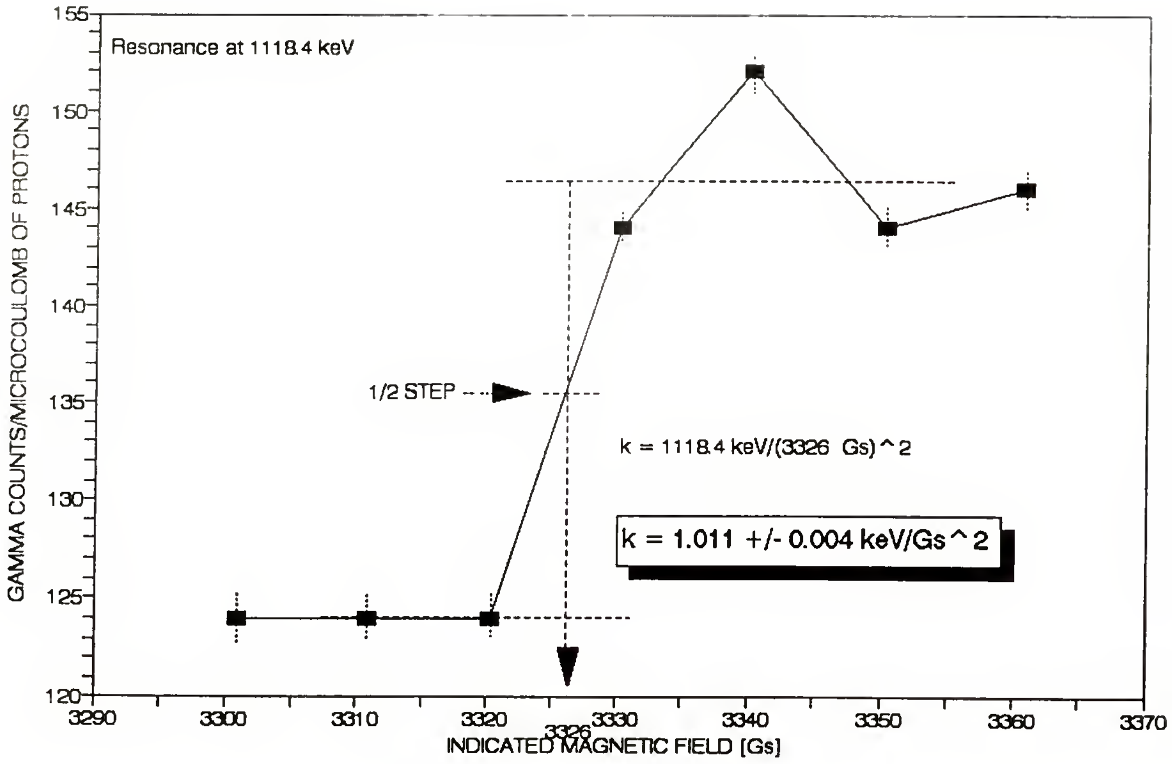

Figure 6-10. Determination of k at the 1118.4 keV resonance

Table 6-8
Summary of the determinations of k
and calculation of the average value

Energy of resonance E [keV]	Magnet constant k [x 10^{-4} keV/Gs^2]	Error Δk [x 10^{-4} keV/Gs^2]
922.6	1.009	0.002
937.2	1.009	0.001
991.88	1.011	0.006
1025	1.009	0.003
1118.4	1.011	0.003

Calculation of k [10^{-4} keV/Gs^2]

$$\bar{k}=\frac{\sum k_i}{5}=1.0098\simeq 1.010$$

$$e=\sqrt{\frac{\sum (\Delta k_i)^2}{5}}=0.00363\simeq 0.004$$

2. The field was increased in increments equivalent to 10 keV of particle energy until it was certain that the resonance had been passed. At each increment, the γ-ray spectrum was accumulated and the total proton charge was integrated, which varied from 9 to 21 μC.
   (Note that counts were accumulated in the γ-ray spectrometer, while charge was accumulated in the current integrator.) There was no special significance to these values--the critical factor was to reduce the statistical uncertainty in the integrated counts to less than 2%.
3. The integrated gamma count in each measurement was divided by the integrated charge, thus obtaining normalized values which were plotted against the magnetic field.
4. The gamma intensities immediately before and after the resonance were separately averaged to obtain the "floor" and "roof" values shown in Figures 6-6 through 6-10. The average between these two values was taken as the gamma intensity at the point of resonance. From the appropriate graph, the value of the magnetic field was determined.
5. Replacing the values of E_0 (resonant energy) and B (indicated magnetic field) in Equation 6-5, the value of k was calculated.

6. In this last step, the five values of k were averaged to obtain

$$k = 1.010 \pm 0.004\,(x\ 10^{-4})\ keV/Gs^{2} \tag{6-7}$$

6.1.1.2.2 Discussion of the uncertainty in the measurements. As shown in Equation 6-5, k = E_o/B^2. Since the two quantities are measured independently, the uncertainty in the value of k as a function of the uncertainties of the two variables is given by

$$\Delta k = \sqrt{(\frac{\partial k}{\partial E})^{2}\Delta E^{2}+(\frac{\partial k}{\partial B})^{2}\Delta B^{2}} \tag{6-8}$$

or

$$\Delta k = \sqrt{(\frac{1}{B^{2}})^{2}\Delta E^{2} + (\frac{E}{B^{3}})^{2}\Delta B^{2}} \tag{6-9}$$

The values of Δk shown in Table 6-8 were computed with this equation.

6.1.1.2.3 Comparison with an earlier measurement. The value of k for singly-ionized molecular hydrogen, H^{+}_{2}, was measured in 1989 by I. Reid [69]. He obtained:

$k = 5.044 \times 10^{-5}$ keV/Gs^2 ± 0.2%

or

$k = (5.044 \pm 0.01) \times 10^{-5}$ keV/Gs^2

Using Equation 6-6, this value of k can be converted to k for H^+:

$$k = 1.008 \pm 0.002\ (x\ 10^{-4})\ keV/Gs^{2}$$

which, within the uncertainty of the measurement, is equal to the value reported here.

6.1.1.3 Current calibration

The calibration of the BIC 1000 was confirmed to within 1% in two steps: first, a Keithley Model 485 Picoammeter (K485) was used to calibrate a Keithley Model 261 Picoampere Source (K261); second, the K261 was used to confirm the accuracy of the BIC 1000.

The accuracy of the K485, which in this instance was used as a secondary standard, is traceable to the National Institute of Standards and Technology (formerly National Bureau of Standards) in a recent certified calibration.

6.1.1.3.1 Instruments used in the calibration. The K261 current source consists of a stabilized voltage supply and a number of high-valued precision resistors which, through four rotary switches can be connected in series with each other and with the power supply. The resulting output current is indicated by the dials if the load is a short circuit. The same is true if the load is a "virtual ground", which constitutes the input impedances of both the K485 picoammeter and the BIC 1000 current integrator.

A block diagram of the K261 is shown in Figure 6-11, and that of a circuit illustrating a virtual ground in Figure 6-12. The resistors in the K261 have trimming controls, but perhaps because of aging, some of them require more range that can be provided by the trimmers. In those instances, the K485 was used to determine the dial settings of the K261 which delivered the desired currents for the calibration of the BIC 1000.

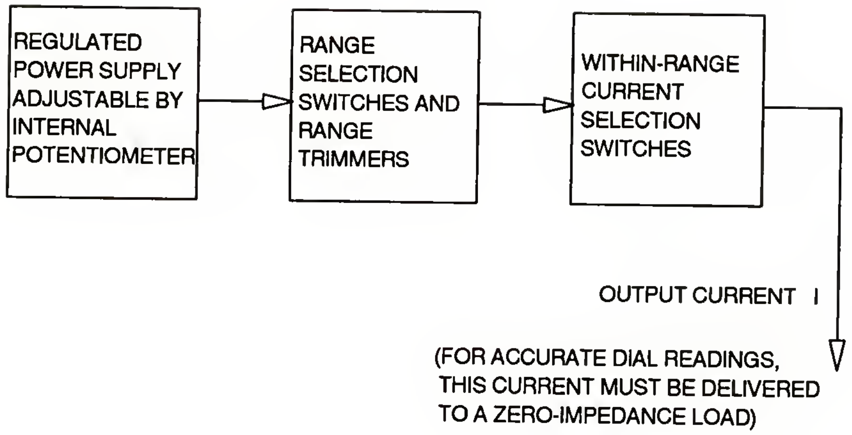
REGULATED POWER SUPPLY ADJUSTABLE BY INTERNAL POTENTIOMETER
RANGE SELECTION SWITCHES AND RANGE TRIMMERS
WITHIN-RANGE CURRENT SELECTION SWITCHES
OUTPUT CURRENT I
(FOR ACCURATE DIAL READINGS, THIS CURRENT MUST BE DELIVERED TO A ZERO-IMPEDANCE LOAD)

Figure 6-11. Block diagram of the K261 current source

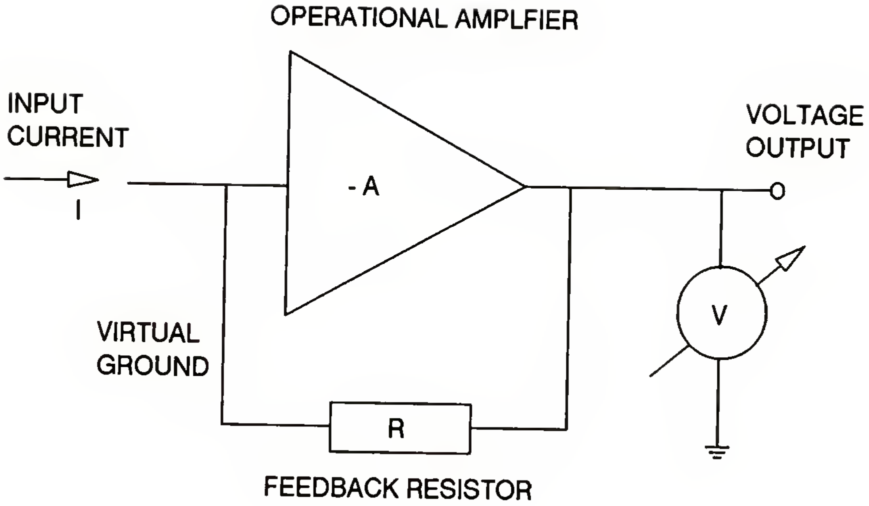

Figure 6-12. Illustration of the virtual ground type of current-measuring instrument

The K485, Ser. No. 464585, is a late model instrument with an error not exceeding 0.4%. The specifications and the factory calibration certificate are shown in Apppendix B.

6.1.1.3.2 Calibration of the K261. The K261 and the K485 were switched ON and allowed to stabilize for at least twohours before making any measurements. The calibration procedure was initiated by directly connecting the output of the K261 to the input of the K485.

The first step was to adjust the internal trimming controls of the K261 such that the values read on the dials matched the currents measured with the K485 for a reading of 1.00 in all ranges. As stated earlier, this adjustment was not possible for some current ranges--those between 10^{-8} and 10^{-10} A. For those ranges, compromise settings of the voltage control and the range trimmers were selected to minimize error.

The second step was to find the actual switch settings in a 5-3-1 sequence of the K261 that gave desired current indications in the K485, for all currents between 5×10^{-5} and 10^{-12} A (current ranges are indicated in the actual order in which they were calibrated). For example: the upper rotary switches of the K261 had to be set for 2.97 to produce a desired current of exactly 3×10^{-11} A (on the RANGE-switch setting of 10^{-11}). The results of this procedure are shown in Table 6-9.

Table 6-9

Calibration of the K261 current source

Desired current [A]	Setting of upper rotary switches	Setting of RANGE switch
1×10^{-12}	1.00	10^{-12}
3×10^{-12}	2.80	10^{-12}
5×10^{-12}	4.70	10^{-12}
1×10^{-11}	1.00	10^{-11}
3×10^{-11}	2.97	10^{-11}
5×10^{-11}	4.95	10^{-11}
1×10^{-10}	9.88	10^{-11}
3×10^{-10}	2.97	10^{-10}
5×10^{-10}	4.95	10^{-10}
1×10^{-9}	9.33	10^{-10}
3×10^{-9}	2.96	10^{-9}
5×10^{-9}	4.94	10^{-9}
1×10^{-8}	1.02	10^{-8}
3×10^{-8}	3.04	10^{-8}
5×10^{-8}	5.08	10^{-8}
1×10^{-7}	1.00	10^{-7}
3×10^{-7}	3.00	10^{-7}
5×10^{-7}	5.00	10^{-7}
1×10^{-6}	1.00	10^{-6}
3×10^{-6}	3.00	10^{-6}
5×10^{-6}	5.00	10^{-6}
1×10^{-5}	1.00	10^{-5}
3×10^{-5}	3.00	10^{-5}
5×10^{-5}	5.01	10^{-5}

Finally, three current values--in the x1, x3, and x5 ranges-- were selected to provide suitably-spaced calibration points on the BIC 1000 panel meter: one near the zero-end of the scale, one at midscale, and one near full scale.

6.1.1.3.3 Verification of the BIC 1000 calibration. The K261 was directly connected to the BIC 1000, and using the values from Table 6-9, the calibration of the current integrator was verified for all ranges (2 x 10^{-9} to 6 x 10^{-5} A). For all but the defective one at 2 x 10^{-9}, the error was found to be less than 0.5%.

The detailed verification procedure was as follows:

1. With the K261 disconnected from the input of the BIC 1000, the range to be verified was selected.
2. The ZERO-OPERATE switch of the BIC 1000 was set at ZERO.
3. Its front panel analog meter was set at zero by adjusting the 10-turn potentiometer located just below the meter, which was the procedure called for in the BIC 1000 instruction manual.
4. The digital counter of the current integrator was reset to zero, and the ZERO-OPERATE switch set to OPERATE.
5. The rotary switches of the K261 were set for the desired current according to Table 6-10, and the K261 reconnected to the BIC 1000.

Table 6-10
Main energy peaks of the calibration sources

Photon Energy [keV]	Comments
6.403	Fe - $K_{\alpha 1}$
7.057	Fe - K_{β}
14.410	^{57}Fe - γ-ray
22.159	Ag - $K_{\alpha 1}$
24.938	Ag - $K_{\beta 1}$
88.030	^{109}Cd - γ-ray

6. The BIC 1000 and a stopwatch were started simultaneously. When the digital indicator of the BIC 1000 reached 500, the stopwatch was halted.
7. The indicated charge was divided by the elapsed time, thereby obtaining the value of the current into the BIC 1000.

6.2 Calibration of the X-ray Spectrometer

For proper identification of the characteristic x-ray lines of the elements used as targets in the probes, the x-ray spectrometer was calibrated in terms of energy vs. channel number. This calibration was performed each time it was necessary to change the spectrometer settings (amplifier gain or shaping time); it was also verified before each series of measurements.

The energy calibration of the x-ray spectrometer consisted in acquiring a spectrum with peaks of known energies and establishing a correlation between energy and channel number.

Two standard radioactive sources (^{109}Cd and ^{57}Co) were routinely used for calibration of the spectrometer. The main energy peaks of these radioisotopes are shown in Table 6-10, and their combined spectrum in Figure 6-13.

Semi-automated features of the MCA were used in the calibration procedure, which was performed as follows. Once the standard spectrum had been acquired, two peaks

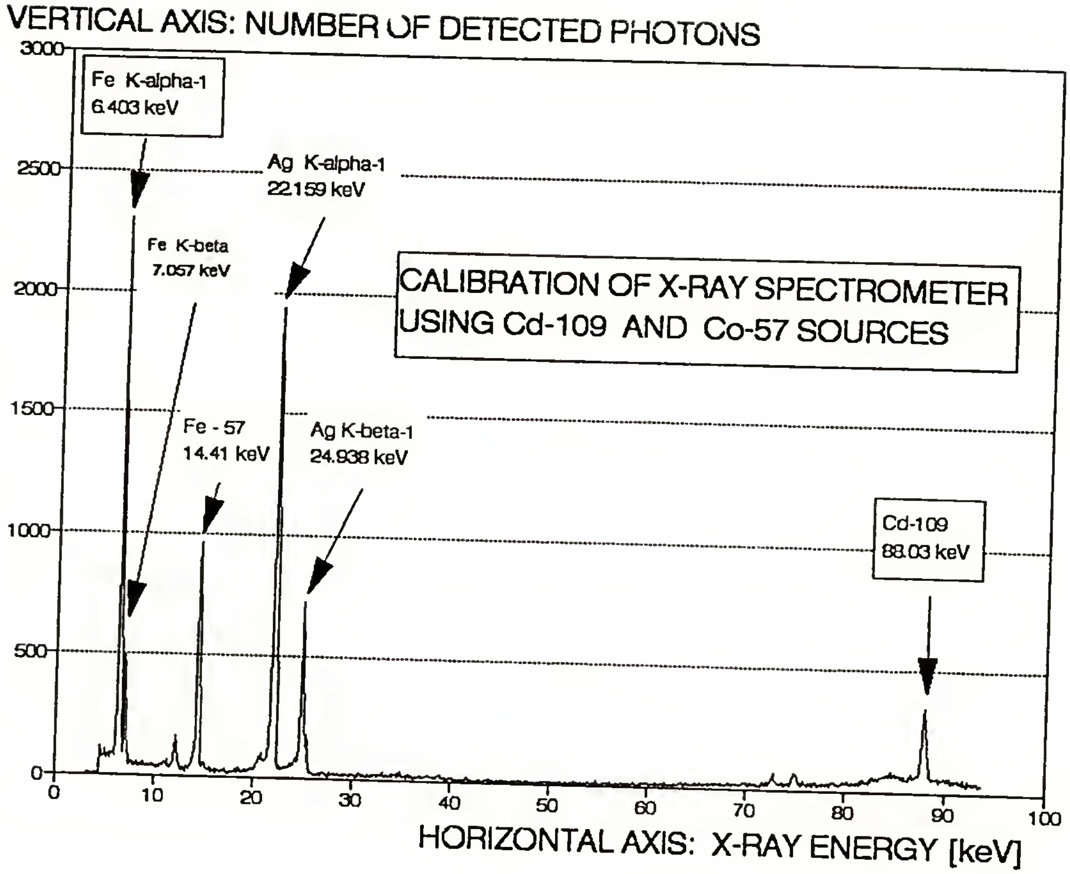

Figure 6-13. Photon energy spectrum of calibration sources

(6.403 and 88.03 keV, for instance) were chosen as calibration points by enclosing them within separate regions of interest (ROI's). The position of the low energy peak was determined by means of a built-in MCA routine which computes its centroid. The query of the analyzer about what energy should be assigned to the channel was answered with the value corresponding to the chosen peak (6.403 keV, in this case). The procedure was repeated with the high energy peak. The analyzer automatically performed a linear calibration of all the channels in terms of energy.

A typical spectrometer calibration curve is shown in Figure 6-14.

6.3 Calibration of X-Ray Excitation Probes

As stated in the introduction to this chapter, the calibration of x-ray excitation probes consists in measuring their specific photon yields Y_{sd}. Later, when a probe is used in actual measurements, its previously obtained Y_{sd} is used in combination with the number of detected photons X_d and the solid angle of detection ω to find the number of intercepted particles P_i:

$$P_i = \frac{X_d}{Y_{sd}\omega} \tag{6-10}$$

The first part of the experimental aspect of this work consisted in measuring values of Y_{sd} for several probes with different target materials built with the two types of

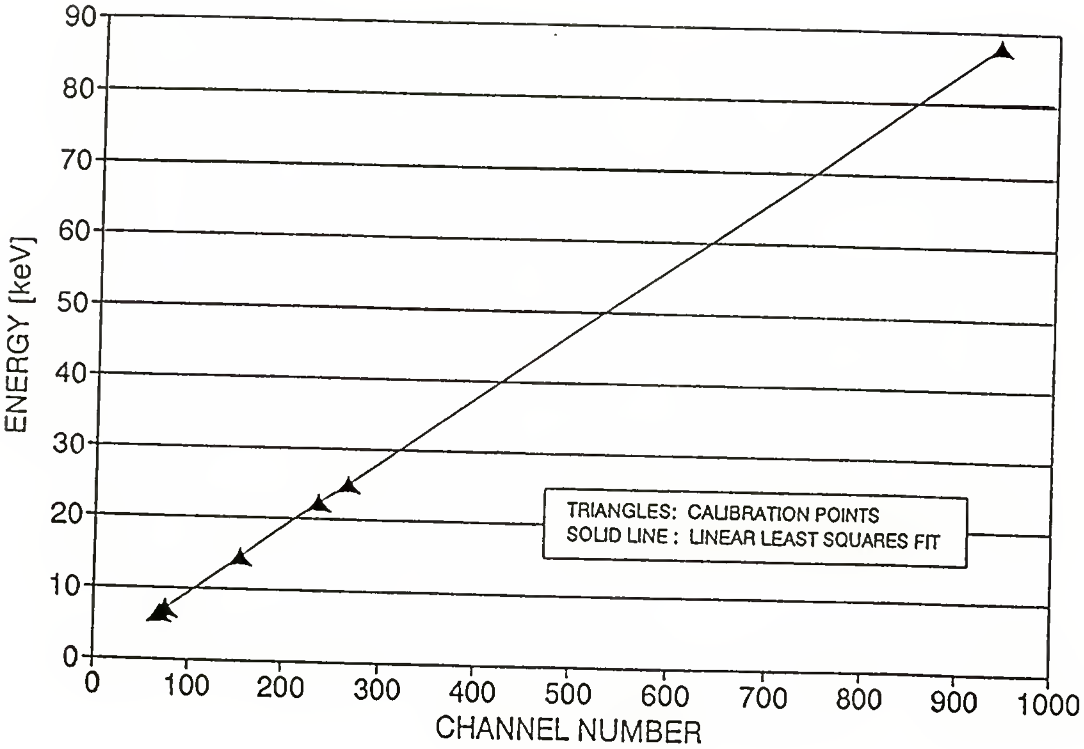

Figure 6-14. Typical spectrometer calibration graph

targets described in Chapter 5: laminiform and filiform. As mentioned before, the first geometry was selected because of its importance in establishing a baseline for measurements of Y_{sd} in general, and the second one because of its wide range of applications.

6.3.1 General Method of Probe Calibration

The Van de Graaff Accelerator (VDG) facility previously discussed is operated by the Physics Department of the University of Florida. Weekly meetings are held at which its usage is scheduled for at least the following seven-day period. At those meetings, users request VDG time and state their requirements such as operating voltage, current, and ionic species.

When the accelerator was used for the purposes of this work the routine described below was generally observed.

On the scheduled dates, the accelerator was started by its operating personnel at the beginning of the working day. It was allowed to stabilize for one and one-half to two hours at the voltage and current at which it would be initially used, and the VDG operator, working at the control console ensured that a beam of the required characteristics was delivered to the user's line. The user was responsible for operation of all the equipment after the isolation valve. This division of responsibilities was generally maintained throughout the measurements. However, the nature of the work require some flexibility in the performance of tasks. There were occasions in which the user relieved the operator in the monitoring of the VDG control console, and conversely, there were many instances in which the operator assisted in performing the measurements.

One of the duties of the user was to ensure that the experimental line had reached the proper level of vacuum before the isolation valve was opened (approximately 10^{-6} torr). Usually, this implied that the day before the accelerator was used, evacuation of the line was started, and the vacuum system was allowed to work overnight. Whenever possible, the vacuum system was kept in continuous operation. However, the nature of the measurements performed in this work often necessitated breaking vacuum to change targets. In this cases, a pumping cycle of approximately one hour was required before resumption of measurements.

Another preliminary action necessary before each series of measurements was the cooling of the HPGe detector to liquid nitrogen temperature. This takes a relatively short time (approximately two to three hours) so it was often possible to fill the dewar early in the morning and to have the detector ready for application of the bias voltage by the time the accelerator had stabilized. The temperature of the detector was monitored by means of a thermistor installed by the manufacturer next to the crystal at the tip of the cold finger to verify the completion of the cooling-down process before applying bias.

After the accelerator had stabilized, the isolation valve was opened and the pressure on both sides was allowed to equalize. The switching magnet was adjusted to the nominal setting for the given beam energy (experimentally determined values for the north line are listed in Table 6-11), and the beam stop[1] was removed from the beam path.

The beam was deflected by the analyzing magnet into the experimental line and allowed to pass through the largest aperture of the collimator mounted on the LMD in the BDA next to the isolation valve (Figure 6-1). At the end of the line, a bluish fluorescent image approximately 1.5 cm in diameter was formed on the fused-silica viewer. The image was centered on the viewer by fine adjustment of the switching magnet. This operation was performed by one person viewing the beam at basement level and another manning the controls at the VDG console, communicating through an intercom.

The quadrupole focusing magnet power supplies --located near the person viewing the spot on the fused silica disc-- were adjusted to yield the desired beam spot size. Usually, this was the smallest spot attainable --approximately 1 mm on the side-- but for some experiments, such as the determination of beam profile described later, a larger spot was selected.

---

[1] A water-cooled, vacuum-sealed copper plunger next to the analyzing magnet exit slit.

Table 6-11
Switching magnet settings for north line

Type of particle	Particle energy [keV]	Switching magnet setting
H_2^+	500	2378
H^+	500	1695
H^+	750	2062
H^+	1000	2379
H^+	1250	2660
H^+	1500	2940
H^+	1750	3149
H^+	2000	3366
H^+	2250	3570
H^+	2500	3761
H^+	2750	3947

The target was moved into position by means of the linear motion device. In the case of wire targets, they were centered on the beam spot by observing their shadow(s) projected on the quartz viewer. This wasn't possible with the laminiform targets, but in their case positioning wasn't critical since it was only required that they intercepted the beam completely.

Once the target was in position, the proper beam and x-ray collimator sizes were selected by trial count rate measurements. The count rate was adjusted to yield an analyzer dead-time indication no larger than a few percent. This was an important aspect of the measurement procedure because of the following.

In principle, the VDG was supposed to generate a constant-current beam. In practice, the intensity of the beam was strongly modulated at a frequency of the order of one cps by the motion of the charging belt. Also, the feedback system responsible for stabilizing the beam energy by controlling the analyzing magnet appeared to be non-critically dampened. This resulted in an additional modulation of the beam. These modulations caused the x-rays to be produced in bursts. Therefore, the readings of the analyzer dead-time meter were not reliable indicators of dead-time losses, except at low counting rates. (The error in total count determination was estimated to be the major contributor to overall experimental error. If measurements must be made at higher rates, either the beam modulation must be significantly reduced or other more sophisticated means of count-loss determination must be employed.)

After these preliminary tasks were completed the actual probe calibration procedure was began.

As mentioned before, the calibration of the probes consisted in measuring their specific photon yield Y_{sd}. To obtain this value it was necessary to measure the number of particles that struck the target P_i, the solid angle of detection ω, and the number of detected photons of the characteristic energy X_d.

The number of particles was obtained from the measurement of the integrated current Q:

$$P_i = \frac{Q}{z_i} \qquad (6\text{-}11)$$

where z_i = charge of the incident ions.

The measurement of Q was performed with BIC 1000 current integrator. The test chamber/Faraday cup was connected to the BIC 1000 by a coaxial cable running from the end of the experimental line to the VDG control console.

The numbers read on the digital indicator of the BIC 1000 needed to be multiplied by the value of the current scale being used to obtain the total charge in coulombs. This charge, in turn, needed to be divided by the charge of the projectiles to obtain the number of protons striking the target. The values of the conversion factors for all the BIC 1000 scales and the types of particles used in the measurement described here were calculated a priori for easy reference and are shown in Table 6-12.

The area of the collimator placed between the exit Mylar window and the detector entrance window and the target-collimator distance determined the solid angle ω (ω = area of collimator/(target-detector distance)^2). Different solid angles were obtained by selecting collimators with different size apertures while keeping constant the target-detector distance.

The total number of counts in the peak of the selected characteristic energy X_d was obtained by means of the peak integration routine built into the MCA.

A remote switching arrangement was installed to allow a single operator to control the start and stop of the current integrator and the MCA simultaneously.

A typical measurement procedure is described below.

1. The analyzer and the current integrator were cleared to zero.
2. With the target in place and the beam striking the target, the current integrator and the analyzer acquisition function were activated simultaneously.
3. In most cases, the acquisition was allowed to proceed until sufficient counts to obtain a standard deviation of 1% or less had been accumulated. At that point, the analyzer and the current integrator were stopped simultaneously.

Table 6-12
Charge-to-protons conversion factors

BIC 1000 Scale [A]	Conversion factors	
	For H^+	For H_2^+
2×10^{-9}	1.248×10^{10}	2.497×10^{10}
6×10^{-9}	3.745×10^{10}	7.491×10^{10}
2×10^{-8}	1.248×10^{11}	2.497×10^{11}
6×10^{-8}	3.745×10^{11}	7.491×10^{11}
2×10^{-7}	1.248×10^{12}	2.497×10^{12}
6×10^{-7}	3.745×10^{12}	7.491×10^{12}
2×10^{-6}	1.248×10^{13}	2.497×10^{13}
6×10^{-6}	3.745×10^{13}	7.491×10^{13}
2×10^{-5}	1.248×10^{14}	2.497×10^{14}
6×10^{-5}	3.745×10^{14}	7.491×10^{14}

4. The counts under the selected peak(s) were integrated.
5. The integrated counts X_d (raw data and dead-time corrected), the integrated current Q, and the solid angle ω were recorded in the log form (Appendix C).
6. Y_{sd} was computed from those values and also recorded in the log form.

6.3.2 Calibration of Probes with Laminiform Targets

Probes made with pure-element thick metallic foils were built and calibrated for the following purposes:

1. To establish a baseline for subsequent measurements of the Y_{sd} of targets with more complex geometries.
2. To compare measured values of Y_{sd} with values calculated from independently measured values of stopping powers and x-ray production cross sections.
3. To use the probes later in the measurement of neutralized beams.

The pure metals used in the targets and the thicknesses of the foils are listed in Table 5-1.

Measurements of Y_{sd} of laminiform probes were performed with proton beams over the 0.5 to 2.5 MeV energy range. All the targets were sufficiently thick to stop 2.5 MeV protons. The geometry was constant for all the measurements: 45°

incidence and take-off angles, and 7.18 x 10^{-3} sr solid angle of detection, except where otherwise indicated. The results of the measurements are shown in Tables 6-13 through 6-17, and interpolated values found from polynomial fitting of the data are shown in Tables 6-18 and 6-19 and in Figure 6-15.

6.3.3 Calibration of Probes with Filiform Targets

X-ray excitation probes with thin-wire targets were also built and calibrated following a procedure similar to that described for the laminiform configuration. As previously mentioned, the filiform geometry has a wide range of applications in the measurement of particle density distributions. (In Chapter 2, several current methods of beam monitoring using thin-wire probes were discussed.) Although different physical processes other than the one presented here are used in these probes, such as charge collection or secondary particle emission, the thin wire configuration in itself proves to be a practical design for the purposes of beam monitoring. Therefore, the filiform targets were chosen to illustrate the probe calibration method in a manner approaching realistic experimental conditions.

The physical arrangement used for the calibration of the wire targets was similar to that of the laminiform probes: the probes were mounted in such a way that the

Table 6-13
Measurements of Y_{sd} for laminiform Nb targets (K-series)

E_o [keV]	P_i ($\times 10^{13}$)	X_d ($\times 10^6$)	Y_{sd} ($\times 10^{-6}$)
518	48.3	0.0002	0.006 ± 0.002
1036	1.94	0.255	1.83 ± 0.2
1036	2.02	0.281	1.94 ± 0.2
1555	2.93	0.898	4.27 ± 0.4
1555	1.52	0.444	4.08 ± 0.4
2074	3.27	2.22	9.46 ± 1
2074	2.52	1.74	9.61 ± 1
2593	2.54	3.35	18.4 ± 2
2593	3.73	4.95	18.5 ± 2

Table 6-14
Measurements of Y_{sd} for laminiform Mo targets (K-series)

E_o [keV]	P_i (x 10^{13})	X_d (x 10^6)	Y_{sd} (x 10^{-6})
518	19.6	0.0051	0.0036 ± 0.0004
518	12.2	0.0032	0.0037 ± 0.0004
1036	0.914	0.0124	0.188 ± 0.02
1036	1.65	0.0246	0.208 ± 0.02
1555	1.75	0.189	1.51 ± 0.2
1555	3.15	0.338	1.49 ± 0.2
2047	18.8	5.72	4.23 ± 0.4
2047	18.9	5.75	4.23 ± 0.4
2593	2.15	1.84	12.0 ± 1
2593	1.92	1.64	11.9 ± 1

Table 6-15
Measurements of Y_{sd} for laminiform Pd targets (K-series)

E_o [keV]	P_i ($\times 10^{13}$)	X_d ($\times 10^{6}$)	Y_{sd} ($\times 10^{-6}$)
518	8.01	0.0006	0.0010 ± 0.0003
1037	8.24	0.0626	0.106 ± 0.01
1037	6.82	0.0510	0.104 ± 0.01
1555	4.11	0.197	0.667 ± 0.07
1555	10.3	0.477	0.643 ± 0.07
2074	3.12	0.703	3.14 ± 0.3
2074	2.11	0.457	3.01 ± 0.3
2593	1.69	0.775	6.37 ± 0.6
2593	3.18	1.46	6.41 ± 0.6

Table 6-16
Measurements of Y_{sd} for laminiform Ta targets (L-series)

E_0 [keV]	P_i (x 10^{13})	X_d (x 10^6)	Y_{sd} (x 10^{-6})
518	20.4	0.475	0.324 ± 0.03
518	11.7	0.256	0.309 ± 0.03
1037	0.472	0.237	7.01 ± 0.7
1037	1.12	0.578	7.19 ± 0.7
1555	1.19	1.92	22.5 ± 2
1555	1.27	0.0468	25.1 ± 0.3
* 2074	2.46	0.208	62.4 ± 0.6
* 2074	1.42	0.121	62.9 ± 0.6
* 2594	1.46	0.203	103 ± 10

* Solid angle = 1.36 x 10^{-4} sr

Table 6-17
Measurements of Y_{sd} for laminiform W targets (L-series)

E_o [keV]	P_i (x 10^{13})	X_d (x 10^6)	Y_{sd} (x 10^{-6})
518	1.23	0.0362	0.409 ± 0.1
1036	5.25	2.23	5.93 ± 0.6
1036	4.23	1.85	5.83 ± 0.6
1556	2.08	2.63	17.7 ± 2
1556	2.39	3.23	18.8 ± 2
2074	2.59	6.27	33.7 ± 3
2074	2.24	5.29	32.9 ± 3
2593	1.23	3.52	39.8 ± 4
2593	1.43	4.06	39.6 ± 4

Table 6-18
Interpolated values of Y_{sd} for laminiform targets (K-series)

E_o [MeV]	Y_{sd} ($\times 10^{-6}$)		
	Nb	Mo	Pd
0.9	1.29	0.09	0.08
1.0	1.63	0.14	0.10
1.1	2.00	0.23	0.15
1.2	2.41	0.36	0.21
1.3	2.88	0.77	0.30
1.4	3.40	1.09	0.44
1.5	4.00	1.48	0.68
1.6	4.68	1.97	1.03
1.7	5.46	2.57	1.37
1.8	6.34	3.27	1.77
1.9	7.35	4.10	2.21
2.0	8.48	5.06	2.71
2.1	9.75	6.17	3.26
2.2	11.2	7.43	3.87
2.3	12.8	8.86	4.53
2.4	14.5	10.5	5.25
2.5	16.5	12.2	6.02

Table 6-19
Interpolated values of Y_{sd} for laminiform targets (L-series)

E_o [MeV]	Y_{sd} $(\times 10^{-6})$	
	Ta	W
0.5	0.32	0.41
0.6	1.11	1.28
0.7	1.90	2.15
0.8	2.69	3.02
0.9	3.48	3.89
1.0	4.28	4.76
1.1	7.00	6.81
1.2	10.3	9.14
1.3	14.2	11.7
1.4	18.7	14.4
1.5	23.7	17.2
1.6	29.2	20.1
1.7	35.1	23.0
1.8	41.4	25.8
1.9	48.2	28.6
2.0	55.3	31.1
2.1	62.7	33.4
2.2	70.4	35.5
2.3	78.4	37.2
2.4	86.6	38.5
2.5	95.0	39.4

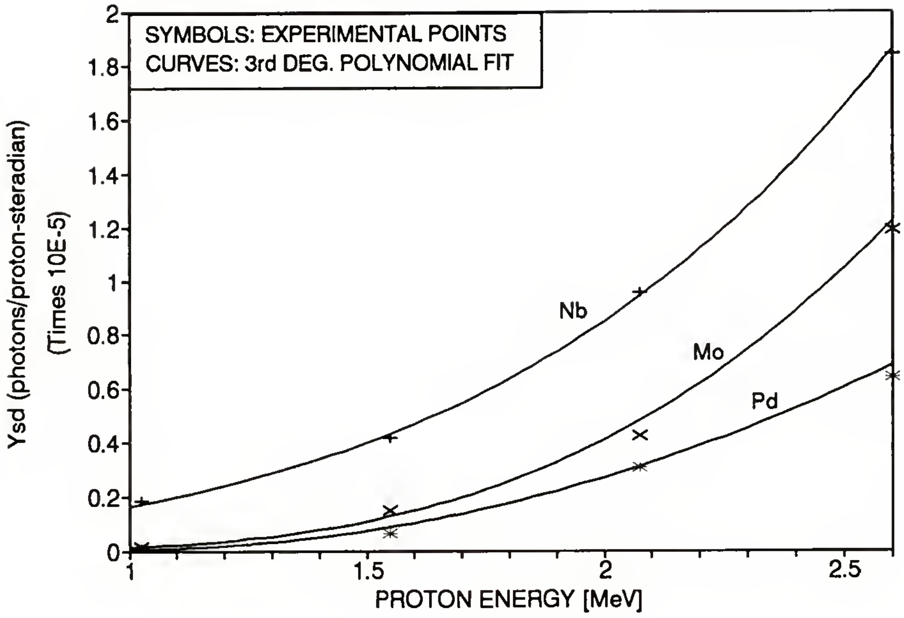

a. K-series

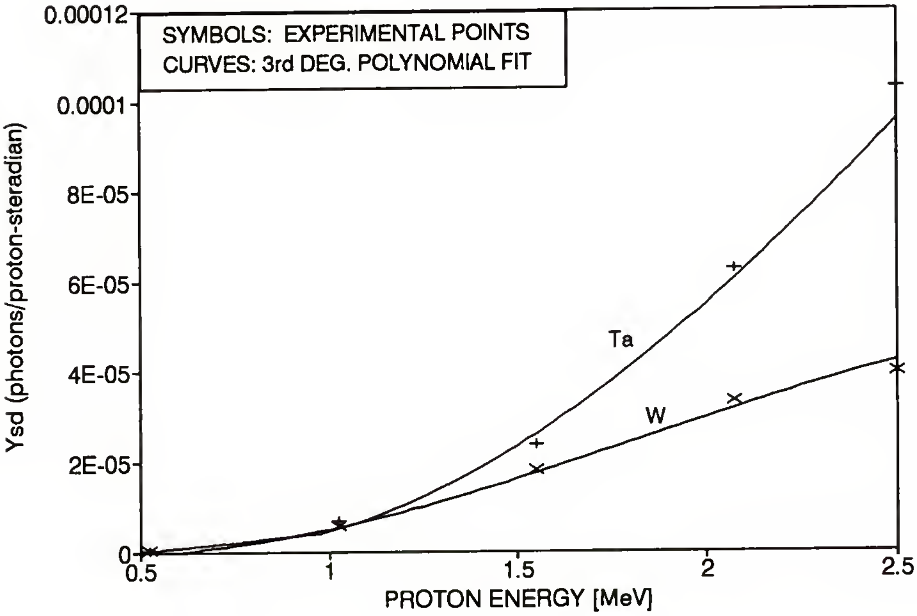

b. L-series

Figure 6-15. Specific detected photon yields of laminiform targets

wires made a 45° angle with the direction of the beam and with the line joining the point of impact with the center of the detector, the target-detector distance was 121.5 mm as before, and the solid angle of detection was 7.18×10^{-3} sr, except where otherwise indicated.

The materials and dimensions of the wires used in this calibration are listed in Table 6-20.

Table 6-20
Materials and sizes of wires used in filiform probes

Element	Wire diameters [μm]
Mo (42)	127, 50, 25, 13
Pd (46)	127
W (74)	127
Pt (78)	127, 25, 10
Au (79)	127

As previously discussed, in the case of thick laminiform targets there was a direct relationship between the charge Q measured by the current integrator and the number of protons P_i striking the target. When using targets with other geometries this is not necessarily the case. If the thickness of the target over the beam cross section is not uniform and in some regions is not sufficient for total particle absorption (thickness < range), some of the particles may emerge from the target after penetrating its full thickness without contributing to the measured value of Q. However, from the standpoint of computing Y_{sd} these particles must still be counted as striking the target. Therefore, some correction must be introduced in the computation of P_i from Q.

Figure 6-16 shows the effect just described for the case of a wire-target mounted at an angle α with respect to the beam. Beacause of its tilt, the wire cross section as α seen by the beam is an ellipse. The particles that strike the center region (defined by segment a) are fully stopped while those on the lateral regions are able to escape after traversing the target. The ratio of the wire diameter d to the length of the segment a is the factor that must be applied to the measured charge Q to obtain the corrected value Q' for the computation of Y_{sd}.

Naturally, this correction factor is a function not only of the wire size and angle with respect to the beam but also of the particle type and energy, and of the wire material. Table 6-21 shows the correction factors for 2.5 MeV protons striking Mo and Pt wire-targets at 45°. These factors were calculated with the following expression derived from Figure 6-16:

$$F_c = \frac{1}{\sqrt{1-\left[\frac{R}{d/\cos 45^\circ}\right]^2}} \qquad (6\text{-}12)$$

where F_c = correction factor

R = range of the particles

d = wire diameter

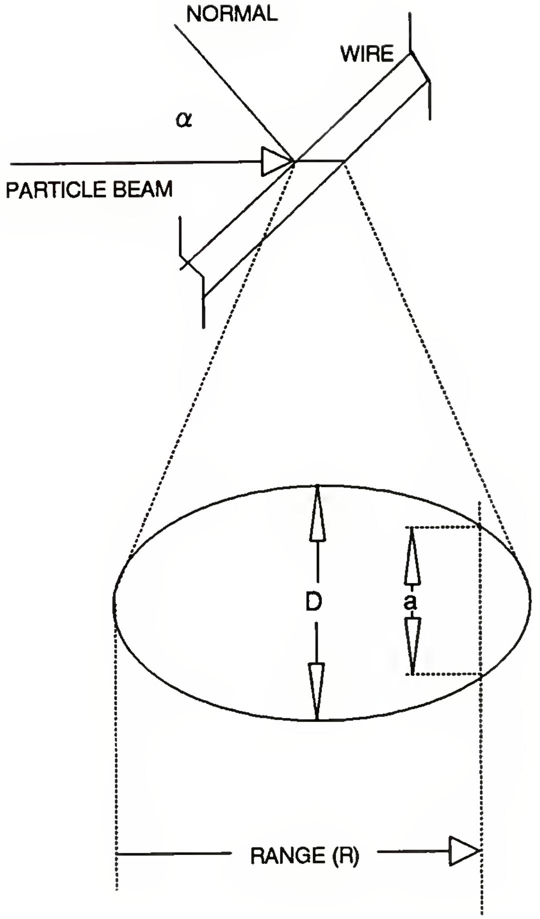

$$F_c = \frac{d}{c} = \frac{1}{\sqrt{1-\left[\frac{R}{d/\cos\alpha}\right]^2}}$$

Figure 6-16. Correction factor for tilted wires

Table 6-21
Correction factors for current-integrator readings for 2.5 MeV protons striking Mo and Pt wire targets at 45°

Wire diameter [μm]	Correction factor (F_c)	
	Mo	Pt
127	1.01	1.00
100	1.01	1.01
75	1.02	1.01
50	1.05	1.03
40	1.09	1.04
30	1.18	1.08
25	1.29	1.13
20	1.62	1.23
19	1.79	--
18	2.07	--
17	2.67	--
16	5.79	--
15	∞	1.57
14	∞	1.77
13	∞	2.18
12	∞	3.72
11	∞	∞

Two series of measurements were performed with filiform probes. The first was the calibration of 127 μm Mo, Pd, W, and Au wires with proton beams over the 0.5 to 2.5 MeV energy range. The second was the calibration at 2.5 MeV of 13, 25, 50, and 127 μm Mo and 10, 25, and 127 μm Pt wires. The results of the first series of measurements are shown in Tables 6-22 through 6-25, and interpolated data from polynomial fittings in Tables 6-26 and 6-27 and in Figure 6-17. The results of the second series of measurements are shown in Tables 6-28 and 6-29.

Table 6-22
Measurements of Y_{sd} for filiform (d = 127 μm)
Mo targets (K-series)

E_o [keV]	P_i (x 10^{13})	X_d (x 10^6)	Y_{sd} (x 10^{-6})
518	16.7	0.0019	0.0016
1037	33.5	0.219	0.0920
1556	2.98	0.146	0.690
2074 *	2.98	0.0090	2.25
2594 *	2.75 #	0.0214	5.73

* Solid angle of detection ω = 1.36 x 10^{-4} sr
# Corrected with the factor of Table 6-21

Table 6-23
Measurements of Y_{sd} for filiform (d = 127 μm)
Pd targets (K-series)

E_o [keV]	P_i (x 10^{13})	X_d (x 10^6)	Y_{sd} (x 10^{-6})
519	8.32	0.00031	0.00052
1036	3.50	0.0123	0.0489
1556	39.9	0.902	0.315
2075	2.52	0.304	1.68
2593	1.69	0.376	3.11

Table 6-24
Measurements of Y_{sd} for filiform (d = 127 μm)
W targets (L-series)

E_o [keV]	P_i (x 10^{13})	X_d (x 10^6)	Y_{sd} (x 10^{-6})
519	1.09	0.0092	0.119
1036	0.764	0.0019 *	1.79
1556	3.06	0.0388 *	9.34
2075	7.68	0.178 *	17.2
2593	7.13	0.277 *	28.7

* Solid angle of detection ω = 1.355 x 10^{-4} sr

Table 6-25
Measurements of Y_{sd} for filiform (d = 127 μm)
Au targets (L-series)

E_o [keV]	P_i (x 10^{13})	X_d (x 10^6)	Y_{sd} (x 10^{-6})
519	21.3	0.0826	0.0541
1037	45.0	4.64	1.44
1555	15.2	12.1 *	5.87
2074	3.18	602 *	14.0
2593	1.13	586 *	38.2

* Solid angle of detection ω = 1.355 10^{-4} sr

Table 6-26
Interpolated values of Y_{sd} for filiform (d = 127 μm) targets (K-series)

E_o [MeV]	Y_{sd} (x 10^{-6})	
	Mo	Pd
0.5	0	0
0.6	0.0162	0
0.7	0.0365	0
0.8	0.0548	0.0004
0.9	0.0762	0.0008
1.0	0.106	0.003
1.1	0.148	0.033
1.2	0.209	0.102
1.3	0.293	0.189
1.4	0.405	0.294
1.5	0.510	0.418
1.6	0.734	0.561
1.7	0.961	0.724
1.8	1.24	0.908
1.9	1.56	1.11
2.0	1.95	1.34
2.1	2.40	1.59
2.2	2.92	1.86
2.3	3.51	2.15
2.4	4.18	2.47
2.5	4.93	2.81

Table 6-27
Interpolated values of Y_{sd} for filiform (d = 127 μm) targets (L-series)

E_o [MeV]	Y_{sd} (x 10^{-6})	
	W	Au
0.5	0	0
0.6	0.0518	0
0.7	0.292	0.0003
0.8	0.702	0.184
0.9	1.28	0.527
1.0	2.01	1.02
1.1	2.89	1.66
1.2	3.90	2.43
1.3	5.06	3.33
1.4	6.34	4.35
1.5	7.73	5.49
1.6	9.24	6.72
1.7	10.8	8.06
1.8	12.6	9.48
1.9	14.3	11.0
2.0	16.2	12.6
2.1	18.2	14.2
2.2	20.2	15.9
2.3	22.2	17.7
2.4	24.4	19.5
2.5	26.5	21.3

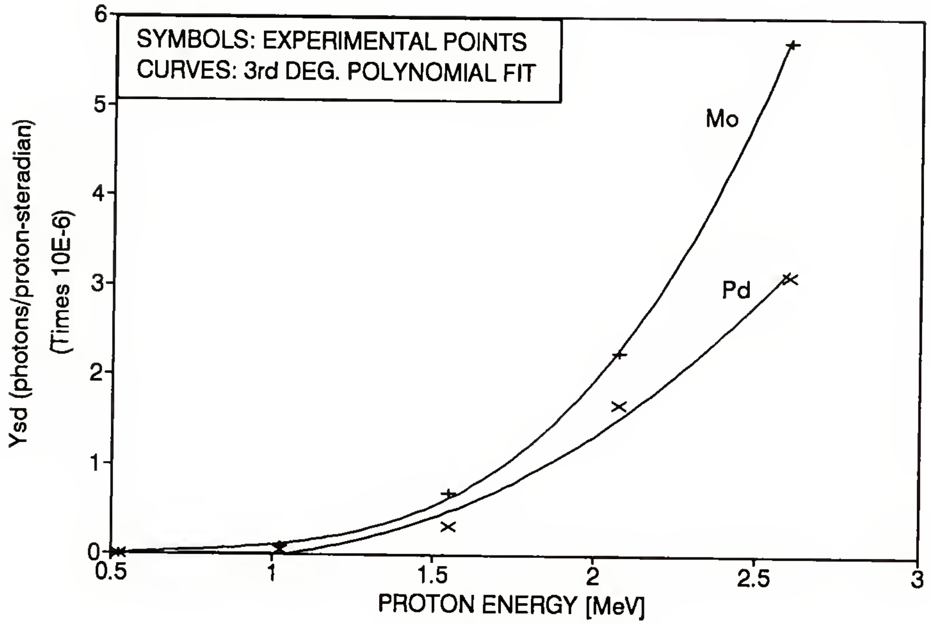

a. K-series

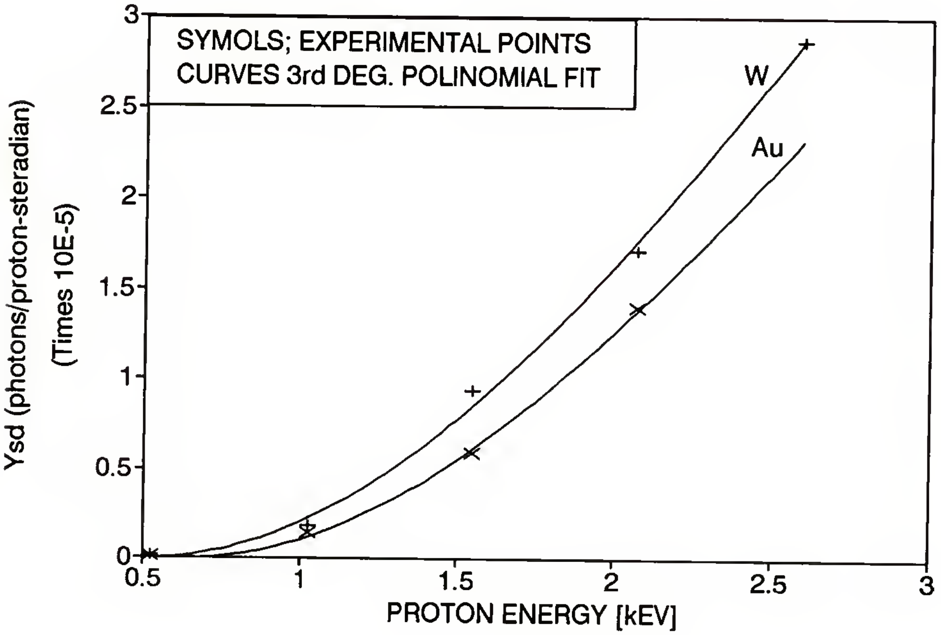

b. L-series

Figure 6-17. Specific detected photon yields of filiform targets of 0.127 mm diameter

Table 6-28
Measurements of Y_{sd} for filiform Mo targets
at E_o = 2.5 MeV
(K-series)

D [μm]	P_i * (x 10^{13})	X_d (x 10^6)	Y_{sd} (x 10^{-6})
13	?	0.268	6 #
13	?	0.282	6 #
25	1.14	0.529	6.46
25	1.29	0.607	6.58
50	1.76	0.0145 +	6.07
50	2.42	0.0191 +	5.85
127	4.49	0.0388 +	6.38
127	2.72	0.0214 +	5.79

* Corrected with the factors of Table 6-21
# Estimated values
+ Solid angle of detection $\omega = 1.355 \times 10^{-4}$ sr

Table 6-29
Measurements of Y_{sd} for filiform Pt targets
at E_o = 2.5 MeV
(L-series)

D [μm]	P_i * (x 10^{13})	X_d (x 10^6)	Y_{sd} (x 10^{-6})
10	?	0.0065	20 #
10	?	0.0121	20 #
25	0.897	1.98	30.7
25	0.906	1.85	28.4
127	3.16	0.0826 +	19.3
127	5.63	0.149 +	19.5

* Corrected with factors of Table 6-21
# Estimated values
+ Solid angle of detection $\omega = 1.355 \times 10^{-4}$ sr

6.3.4 Calibration of Probes Using Partially Ionized Beams

All the measurements of Y_{sd} discussed in sections 6.3.2 and 6.3.3 were performed using fully ionized particles (protons) with energies from 0.5 to 2.5 MeV. From the standpoint of the application that first motivated the development of the multi-element x-ray excitation probes (SCFR) it was also of interest to obtain values of Y_{sd} for proton energies below 0.5 MeV. Unfortunately, because of the difficulty of extracting ions from the ion source when the VDG was operated at accelerating potentials below 0.5 MeV it was not possible to use proton beams below that energy. However, it was possible to extract singly-charged molecular hydrogen ions (H_2^+) and accelerate them to 0.5 MeV. Each of these particles is expected to dissociate into a hydrogen nucleus and a hydrogen atom almost immediately upon impact with the target. In addition, it is also expected that the hydrogen atoms resulting from these dissociations will become immediately ionized.[1] Therefore, two protons with essentially identical energy (250 keV) are obtained from each of the original particles.

Five hundred keV singly-ionized molecular hydrogen beams were used to calibrate thick laminiform tantalum targets for a laminiform tantalum target with 1 MeV protons

---

[1] These assumptions were tested by measuring the proton Y_{sd} immediately before and immediately after measuring it with 2 MeV singly-ionized molecular hydrogen. The obtained results were respectively, 5.953, 5.971, and 6.013 x 10^{-6}.

(L-series) at a proton energy of 250 keV. Four determinations were performed with the following results: Y_{sd} = 1.9, 1.6, 2.3, and 3.3 x 10^{-9}. Because at these low energies the x-ray production cross-section varies with the fourth or fifth power of the energy, the reported results are only an indication of the order of magnitude of the specific detected photon yields.

6.4 Measurements of Beam Profiles and Position Using Multi-element X-ray Excitation Probes

To illustrate typical applications of the method described in this work, profiles and position of the proton beam of the VDG accelerator were measured with multi-element x-ray excitation probes built with 0.127 mm W, Au, Mo, and Pd wires mounted 0.46 mm apart on a fork holder. The wires were mounted in the indicated order, which is also the order of increasing energy of their respective principal x-ray lines (Table 6-30).

Table 6-30
Principal x-ray lines of the target materials
used in the measurement of beam profiles

Element	Energy of principal x-ray line [keV]
W	8.396 ($L_{\alpha 1}$)
Au	9.712 ($L_{\alpha 1}$)
Mo	17.476 ($K_{\alpha 1}$)
Pd	21.174 ($K_{\alpha 1}$)

Figures 6-18 through 6-23 show the results of the measurements. Each figure has three sections. The top section is a diagram of the wire array and of the approximate outline of the beam cross section, as seen on the fluorescent quartz disk. The direction of the beam is into the page. The middle section is the composite x-ray spectrum of the multi-element probe, as seen on the MCA monitor. The lower section is a bar graph showing the number of particles intersected by each of the wires. The three sections are approximately aligned in the vertical direction to highlight the correspondence between each wire position and its corresponding x-ray line, and between these and the number of particles.

Because there is some overlap between some of the x-ray lines in the spectrum, the counts under the peaks were corrected for this interferences whenever necessary before computing the heights of the bars in the lower graphs.

6.5 Measurement of Beams Neutralized with Carbon Foils

As discussed before, one of the applications in which x-ray excitation probes can be used to an advantage is in the measurement of atomic and molecular beams. In particular, one of the diagnostic requirements of the SCFR is the characterization of neutral beams, should this mode of particle injection be selected for the proof-of-principle experiments (see Chapter 2). Therefore, it was deemed

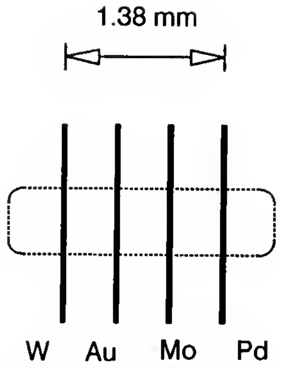

a. Relative positions of beam cross section and multi-element x-ray probe targets

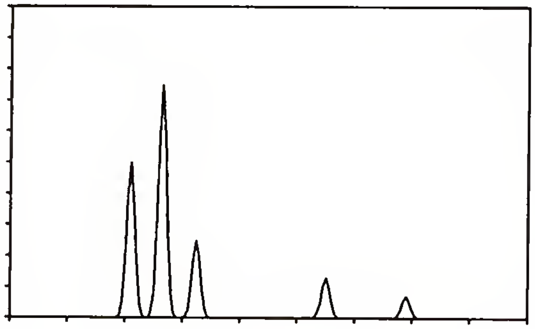

b. composite x-ray spectrum

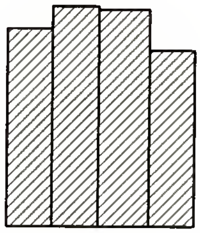

c. Beam intensity profile

Figure 6-18. Measurement of beam profile (I) (beam direction: into the page)

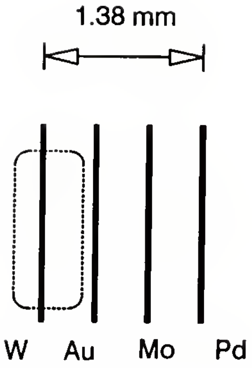

a. Relative positions of beam cross section and multi-element x-ray probe targets

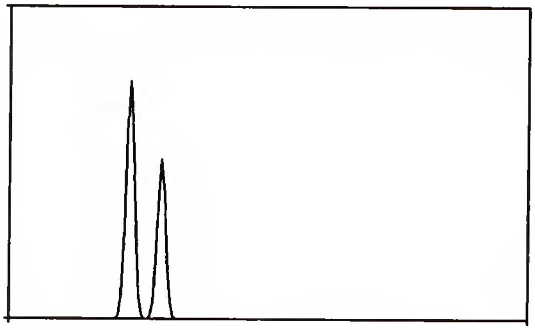

b. composite x-ray spectrum

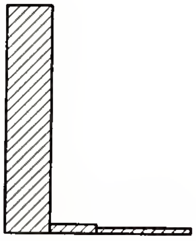

c. Beam intensity profile

Figure 6-19. Measurement of beam profile (II) (beam direction: into the page)

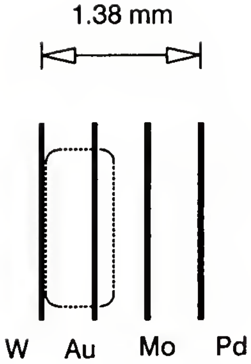

a. Relative positions of beam cross section and multi-element x-ray probe targets

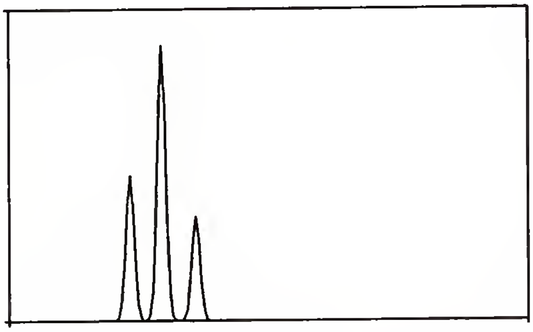

b. composite x-ray spectrum

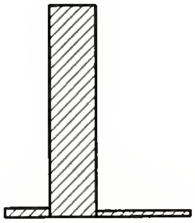

c. Beam intensity profile

Figure 6-20. Measurement of beam profile (III)
(beam direction: into the page)

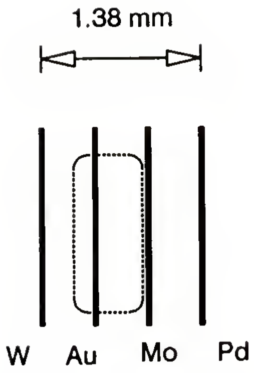

a. Relative positions of beam cross section and multi-element x-ray probe targets

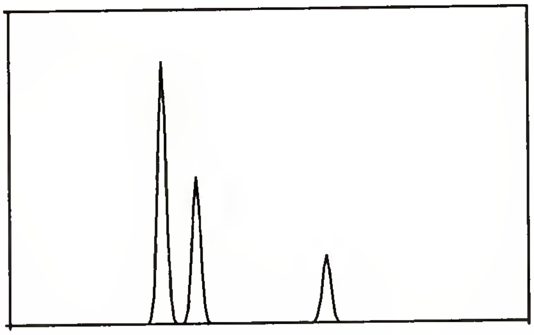

b. composite x-ray spectrum

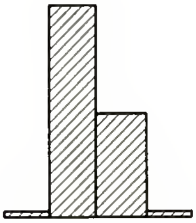

c. Beam intensity profile

Figure 6-21. Measurement of beam profile (IV)
(beam direction: into the page)

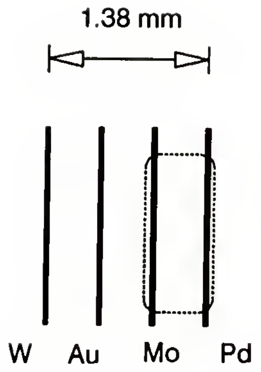

a. Relative positions of beam cross section and multi-element x-ray probe targets

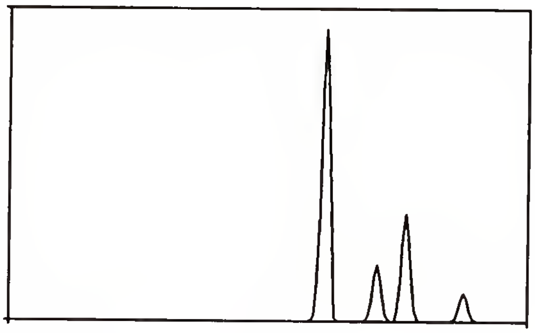

b. composite x-ray spectrum

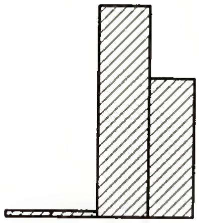

c. Beam intensity profile

Figure 6-22. Measurement of beam profile (V)
(beam direction: into the page)

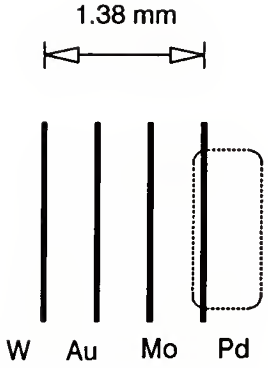

a. Relative positions of beam cross section and multi-element x-ray probe targets

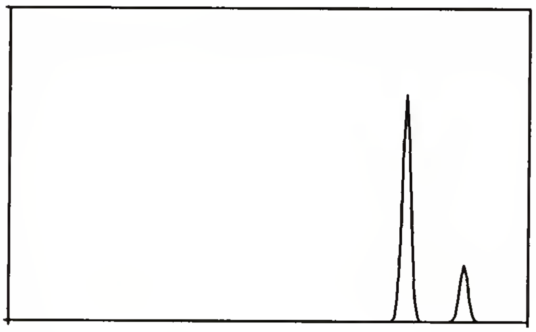

b. composite x-ray spectrum

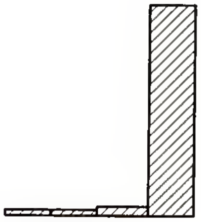

c. Beam intensity profile

Figure 6-23. Measurement of beam profile (VI)
(beam direction: into the page)

appropriate to use one of the versions of the probe for some of the preliminary beam-neutralization experiments. The experiment consisted in determining the fraction of hydrogen ions that could be neutralized using a 200 Å carbon foil. Five hundred keV singly-ionized molecular hydrogen was used in the experiment. A laminiform tungsten target mounted on an aperture type frame was chosen to measure the number of particles (charged or neutral). A counting time of 600 s was selected in every case. The carbon foil was mounted on an LMD in the BDA located towards the center of the experimental line (Figure 6-1). The LMD allowed the foil to be placed on the beam path or to retract it and permit the beam to pass through a large aperture. The probe was mounted, as usual, on an LMD in the BDA at the far end of the line and could also be retracted to allow viewing of the beam on the quartz disk.

The experimental procedure consisted of the following steps:

1. Before allowing the beam into the experimental line, a background count was taken with the tungsten target in place.
2. The beam was admitted into the line and its cross section was centered on the quartz viewer and partially focused to a diameter of several millimeters with the quadrupole lens. The carbon foil was out of the beam path for this step.

3. A reading of the current from the Faraday cup and an x-ray count were taken in these conditions.
4. With the carbon foil still out of the beam path, a set of two strong NdFeB magnets was used to deflect the charged-particle beam completely off the target. This was verified with the quartz viewer. However, if the room was darkened it was possible to see a faint bluish glow diffused over the quartz disk. This glow was attributed to particles that had been neutralized by the remnant gas in the experimental line.
5. The Faraday cup current was again measured in these conditions and it was found to be below the limit of detectability. The x-ray count increased slightly over the background value obtained in step 1. Again, this was attributed to the gas-neutralized particles striking the target.
6. The carbon foil was moved into position to intercept the beam.
7. A slight but significant increase in the x-ray count was observed in these conditions.
8. The x-ray count difference between steps 7 and 5 was taken as the net increase due to the neutralizing effect, and it was used to compute its neutralizing efficiency.

The results of two measurements performed according to the procedure just described are given below.

Experiment No. 1

A. Measurements.

Background measurement:

X-ray intensity = 28 counts/600 s

Diffuse beam measurements:

Faraday cup current ≈ 220×10^{-9} A

X-ray intensity = 16,487 counts/600 s

Beam deflected off-target:

Faraday cup current ≈ 3×10^{-10} A

X-ray intensity = 37 counts/600 s

Beam through carbon foil:

X-ray intensity = 47 counts/600 s

B. Computations

Determination of neutralization efficiency

$$\frac{\phi(H^{o})}{\phi(H^{+}{}_{2})} = \frac{47 - 37}{\frac{1}{2}(16{,}487)} = 1.2 \times 10^{-3}$$

where $\phi(H^{o})$ = Number of hydrogen atoms

$\phi(H^{+}{}_{2})$ = Number of singly-ionized hydrogen molecules

Experiment No. 2

A. Measurements.

Background measurement:

The value obtained in Experiment No. 1 was used.

Diffuse beam measurements:

Faraday cup current ≈ 150 x 10^{-9} A

X-ray intensity = 20,149 counts/600 s

Beam deflected off-target:

Faraday cup current ≈ 3 x 10^{-10} A

X-ray intensity = 30 counts/600 s

Beam through carbon foil:

X-ray intensity = 79 counts/600 s

B. Computations

Determination of neutralization efficiency

$$\frac{\phi(H^{o})}{\phi(H^{+}_{2})} = \frac{79 - 30}{\frac{1}{2}(20{,}149)} = 1.6 \times 10^{-3}$$

CHAPTER 7
CALCULATION OF SPECIFIC DETECTED PHOTON YIELDS

As discussed in the previous chapter, experimental values of Y_{sd} determined in conditions closely resembling those in which the probes will actually be used are preferable to values determined from calculations based on independently measured stopping powers and x-ray production cross sections found in the literature. However, as indicated in Chapter 4, it is not always possible to measure Y_{sd} in the required conditions. This is the case, for instance, when it is desirable to know the specific detected photon yield (or at least its approximate value) in experimental conditions that are beyond the range of the available equipment. For example, the measurements of Y_{sd} presented in Chapter 6 were limited to thick laminiform targets and to filiform targets at least 10 μm in diameter. In addition, they were only performed for proton energies in the range 0.25 to 2.5 MeV. The 10 μm limitation in wire size was imposed by the difficulty of obtaining a direct measurement of the number of particles striking wires of smaller diameter, and the energy span limitation was imposed by the minimum and maximum operating energies of the VDG.[1] Therefore, to obtain values of Y_{sd} outside the range where measurements were possible, it was necessary to arrive at them by calculation. In this chapter, calculations of the specific detected photon yield for thick foils and for thin wires are presented, both within and outside the ranges of wire size and particle energy used in the experiments. The calculations of Y_{sd} for targets for which it had already been determined experimentally were performed to compare the values obtained with each method. The calculations for targets not used in the experiments were done to illustrate the general applicability of the calculation procedure.

7.1 Calculation of Specific Detected Photon Yields for Targets Bombarded with Protons in the Energy Range from 0.5 to 2.5 MeV

7.1.1 Calculation of Y_{sd} for Thick Laminiform Targets

In Chapter 4, Equation 4-13, which gives the value of Y_{sd} for thick laminiform targets as a function of all the experimental parameters, was derived. It is reproduced below as Equation 7-1.

As was indicated in Chapter 4, when the plane of a laminiform target or the axis of a filiform target is at 45°

---

[1] As discussed before, when the wire dimensions approach the range of the particles in the target material, correction factors must be applied to the current-integrator indication to account for particles that strike the wire but are not fully stopped by it. These correction factors become exceedingly large for small-diameter wires eventually rendering the measurements meaningless.

$$Y_{sd}(E_o) = \rho_a \left[\int_0^{R(E_o)} \sigma(\langle E(t) \rangle)\, e^{-\mu\tau} dt \right] F_{aj}\, \epsilon\, \frac{1}{4\pi} \qquad (7\text{-}1)$$

with the direction of the particle beam and with the line joining the point of impact with the direction of photon detection, the two distances t (penetration of particles) and τ (distance of x-rays travel in the target) become equal. This was shown in Figure 4-8. This geometry was used in all the measurements reported in Chapter 6, and will be used in all the calculations of this chapter. Therefore, it is not necessary to continue indicating the two variables separately in the equations, and only the variable t will be used from this point on.

Y_{sd} was calculated by approximating the integral by a summation over ten intervals:

$$Y_{sd}(E_o) = \rho_a \left[\sum_1^{10} \sigma(\langle E(t_i) \rangle)\, e^{-\mu t_i} \Delta t_i \right] F_{aj}\, \epsilon\, \frac{1}{4\pi} \qquad (7\text{-}2)$$

To apply this equation to the calculations presented here, it was necessary to choose suitable intervals Δt_i and to use the values of x-ray production cross section for the particle energies at the different target depths. The intervals Δt_i were chosen to yield equal energy loss ($\Delta E = E_o/10$). These intervals can be obtained from the particle range data published in graphic form by Anderson and Ziegler [38]. The method used to obtain the values of Δt_i is illustrated in Figure 7-1. Comparisons of the values of the

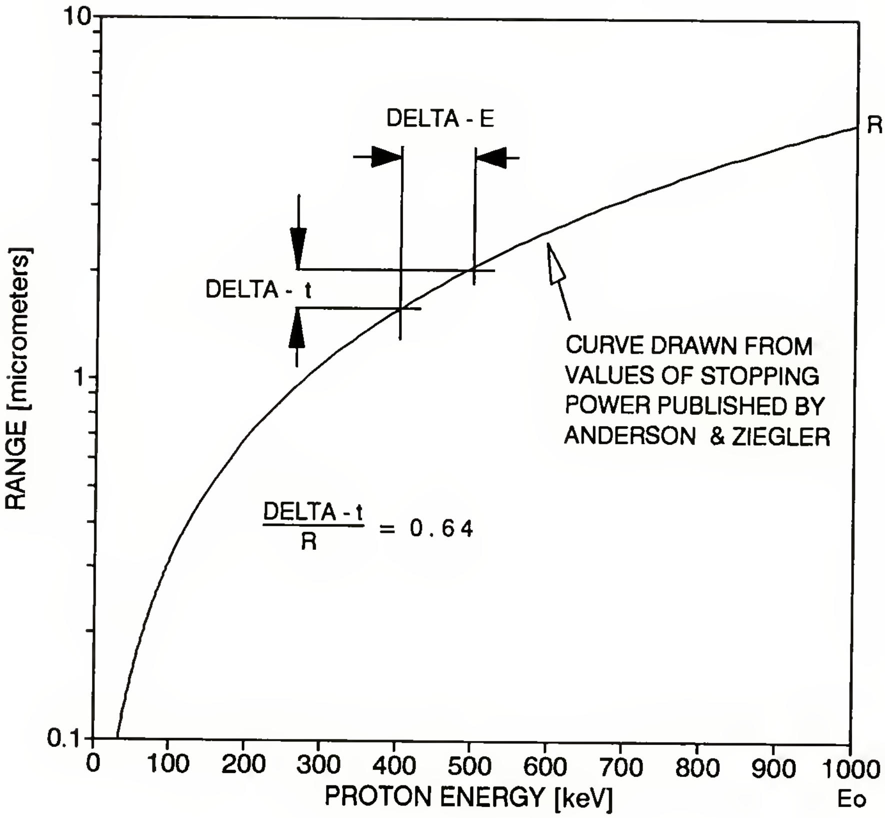

Figure 7-1. Illustration of the method used to determine the values of Δt_i used in Equation 7-2

intervals for different materials and for different values of initial proton energy E_0 showed that if the penetration t is normalized with respect to the range R of the protons and the energy is normalized with respect to E_0, the function t/R vs. E/E_0 is roughly independent of the material and of E_0 (at least within the range of proton energies of interest --0 to 10 MeV-- and for the selected target materials --$41 < Z < 79$--). This is shown in Table 7-1. The last two columns in this table show the mean values of the penetration for the given fraction of initial energy and their standard deviation. The graph of Figure 7-2 is a plot of these mean values vs. the fraction of initial energy. This universal curve can be used for finding the energy of protons at any depth in a material by multiplying the vertical scale by the initial proton energy and the horizontal scale by the range of the protons in the material. For ease of use, the values of t_i and Δt_i obtained from the graph for $0.1E_0$ energy intervals are listed in Table 7-2. Once the proton energy at the different target depths was determined in this manner, the appropriate x-ray production cross sections were found, as indicated below, and assigned to each interval.

For low-Z target materials (Nb, Mo, Pd) the K-series x-ray production cross sections published in the literature [41] or calculated with Equation 4-3 were used.

For high-Z materials (Ta, W, Pt, Au) the published values of L-series x-ray production cross sections are

Table 7-1. Normalized target penetration (t/R) vs. normalized proton energy (E/E_o)

Target	Nb	Nb	Mo	Mo	Pd	Pd	Ta	Ta	W	W	Pt	Pt	Au	Au		
Eo (MeV)	10	1	10	1	10	1	10	1	10	1	10	1	10	1		
Range (µm)	280	7.5	230	6.2	210	6	200	6	170	5.3	150	5.1	180	5.2		
E/Eo															Mean	Std Dev
1.0	0.00	0.00	0.00	0.00	0.00	0.00	0.00	0.00	0.00	0.00	0.00	0.00	0.00	0.00	0.000	0.000
0.9	0.11	0.13	0.11	0.13	0.14	0.14	0.13	0.13	0.11	0.11	0.10	0.16	0.11	0.13	0.125	0.015
0.8	0.30	0.27	0.24	0.31	0.29	0.30	0.32	0.28	0.31	0.26	0.23	0.25	0.31	0.25	0.281	0.029
0.7	0.46	0.44	0.43	0.39	0.43	0.43	0.45	0.37	0.44	0.40	0.38	0.43	0.42	0.40	0.420	0.028
0.6	0.57	0.56	0.54	0.53	0.55	0.52	0.55	0.52	0.57	0.53	0.52	0.57	0.56	0.54	0.544	0.019
0.5	0.68	0.63	0.65	0.65	0.66	0.65	0.66	0.63	0.68	0.64	0.65	0.65	0.66	0.63	0.651	0.015
0.4	0.78	0.76	0.77	0.73	0.76	0.73	0.76	0.72	0.77	0.75	0.74	0.75	0.77	0.75	0.752	0.018
0.3	0.86	0.84	0.86	0.82	0.85	0.82	0.85	0.82	0.84	0.81	0.83	0.82	0.84	0.82	0.835	0.016
0.2	0.92	0.91	0.92	0.90	0.91	0.90	0.92	0.88	0.92	0.88	0.91	0.88	0.91	0.88	0.904	0.015
0.1	0.97	0.97	0.97	0.95	0.97	0.95	0.97	0.95	0.97	0.94	0.97	0.94	0.97	0.94	0.960	0.013
0.0	1.00	1.00	1.00	1.00	1.00	1.00	1.00	1.00	1.00	1.00	1.00	1.00	1.00	1.00	1.000	0.000

Note: Figures printed on shaded background are values of the penetration expressed as a fraction of the range.

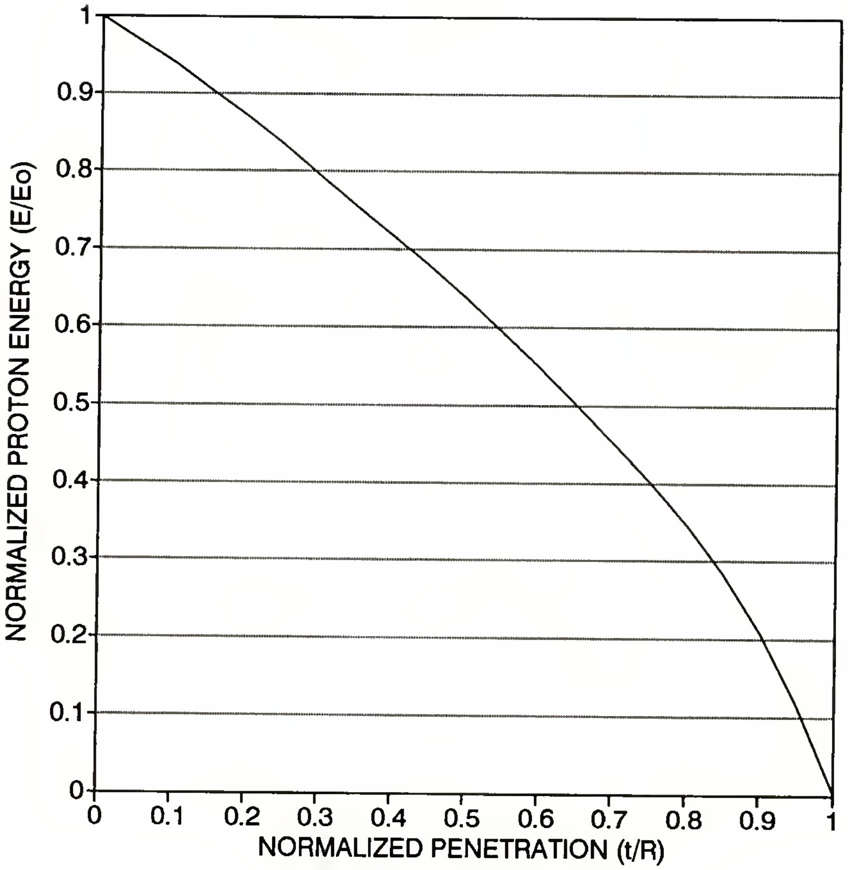

Figure 7-2. Universal graph of proton energy loss vs. target penetration

Table 7-2. Depth intervals and proton energies used in Equation 7-2

i	t_i	Δt_i	$<E(t_i)>$
1	0.125R	0.125R	$1.0E_o$
2	0.281R	0.156R	$0.9E_o$
3	0.420R	0.139R	$0.8E_o$
4	0.544R	0.124R	$0.7E_o$
5	0.651R	0.107R	$0.6E_o$
6	0.752R	0.101R	$0.5E_o$
7	0.835R	0.083R	$0.4E_o$
8	0.904R	0.069R	$0.3E_o$
9	0.960R	0.056R	$0.2E_o$
10	1.000R	0.040R	$0.1E_o$

uneven. There is a fairly complete tabulation for Ta (Z = 73) from 0.2 to 5.0 MeV proton energies and for Au (Z = 79) from 0.2 to 30.0 MeV, but only one value (at 0.441 MeV) for metals with intermediate atomic numbers. Therefore, the following interpolation formula was used to calculate the L-series x-ray production cross sections for W (Z = 74) and Pt (Z = 78):

$$\sigma_L(Z) = \sigma_L(Au) + M_Z[\sigma_L(Ta) - \sigma_L(Au)] \qquad (7\text{-}3)$$

where $\sigma_L(Z)$ = L-series x-ray production cross section of material with atomic number Z.

M_Z = Multiplier for material with atomic number Z (see Table 7-3 for values).

and the other symbols are self-explanatory.

The multipliers that yield the published cross section values for proton energies of 0.441 MeV for all elements within atomic numbers 73 and 79 were calculated and are listed in Table 7-3.

The values of the specific detected photon yield vs. energy for thick laminiform tantalum and tungsten targets were calculated using Equation 7-2. The values of $<E(t_i)>$, t_i, and Δt_i used in the equation are those given in Table 7-2. The values of the x-ray production cross sections are those published in reference [41] for tantalum, or calculated with Equation 7-3 for tungsten. The results of the calculations, and the experimental values reported in Chapter 6, are shown in Figure 7-3.

Table 7-3. Interpolation multipliers

Material	Multiplier (M_Z)
Ta (73)	1.000
W (74)	0.786
Re (75)	0.591
Os (76)	0.415
Ir (77)	0.257
Pt (78)	0.119
Au (79)	0.000

7.1.2 Calculation of Y_{sd} for Filiform Targets

Calculations of specific photon yields for wire targets were also performed using Equation 7-2. As mentioned before, the beam-target-detector geometry assumed for the

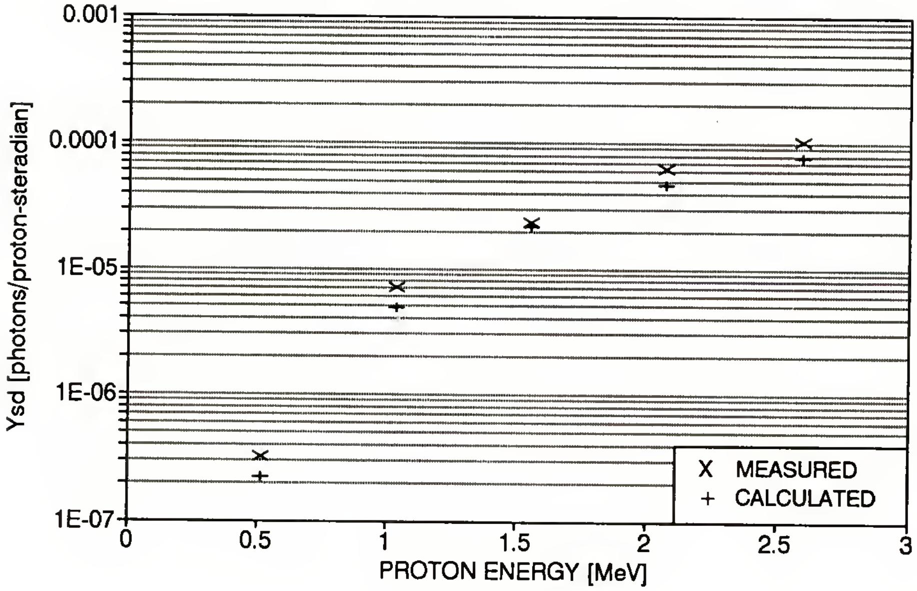

a. Tantalum

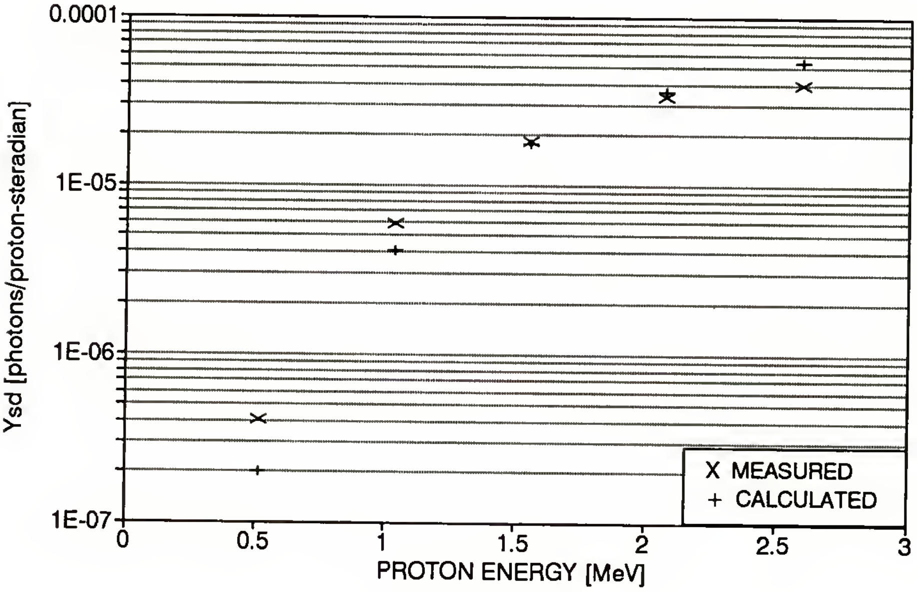

b. Tungsten

Figure 7-3. Specific detected photon yields for thick laminiform targets

calculations is identical to that of the experimental determinations reported in Chapter 6: both the particle beam and the x-ray take-off angle are set at 45°.

Three different cases must be considered in calculating Y_{sd} for filiform targets. If the wires are sufficiently thick (diameter > 0.1 mm) they can be treated as thick laminiform targets without incurring a significant error; in this case Equation 7-2 can be applied directly.

At the other extreme, if the wires are extremely thin (diameter ≈ 0.001 mm --or less) the energy loss of the particles as they traverse the target is very small, and no correction is necessary to allow for the change in particle energy; it is therefore possible to treat the wires as having a uniform thickness equal to their average and to reduce the sum of Equation 7-2 to a single term.

Finally, in the case of wires of intermediate thickness, the summation limits in Equation 7-2 must be modified from chord to chord (see Figure 7-4) to allow for the partial loss of energy of the protons as they traverse different chords of the target.

The geometry that applies to all the cases is shown in Figure 7-4. The considerations stated briefly above are discussed in greater detail in the sections corresponding to each of the three cases.

7.1.2.1 Calculation of Y_{sd} for 0.127 mm filiform targets

As mentioned before, filiform targets with diameters greater than 0.1 mm can be treated as thick laminiform

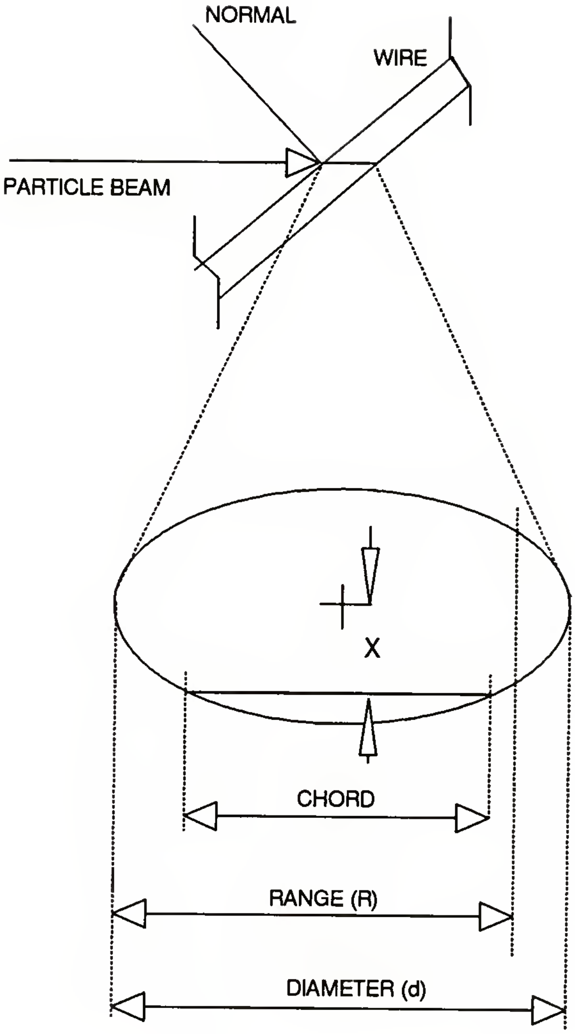

$$CHORD = 2\sqrt{\frac{d^2}{2} - 2x^2}$$

Figure 7-4. Geometry for filiform targets

targets, and Equation 7-2 can be applied directly. This is because when the wire section is divided into ten strips to carry out the summation, even the smallest chord is longer than the range of 2.5 MeV protons in the materials used in the experiments.

Using the procedure of Section 7.1.1, Y_{sd} was calculated for 0.127 mm wires of Mo, Pd, W, and Au, in the range of proton energies from 0.5 to 2.5 MeV. The results of these calculations and the experimental values measured as described in Chapter 6 are shown in Figures 7-5 and 7-6.

7.1.2.2 Calculation of Y_{sd} for filiform targets of intermediate and small diameters

Calculations of Y_{sd} for gold wires with diameters from 0.005 mm (0.5 μm) to 0.127 mm and for a proton energy of 2.5 MeV were performed using Equation 7-2. The upper summation limit was changed when necessary to allow for a chord lengths smaller than the range of the particles. The change in summation limit was necessary for wires with diameters from 0.05 to 0.02 mm. For 0.005 and 0.01 mm wires, the calculations were performed by using the average thickness and reducing the summation to a single term. The results of these calculations are shown in Figure 7-7.

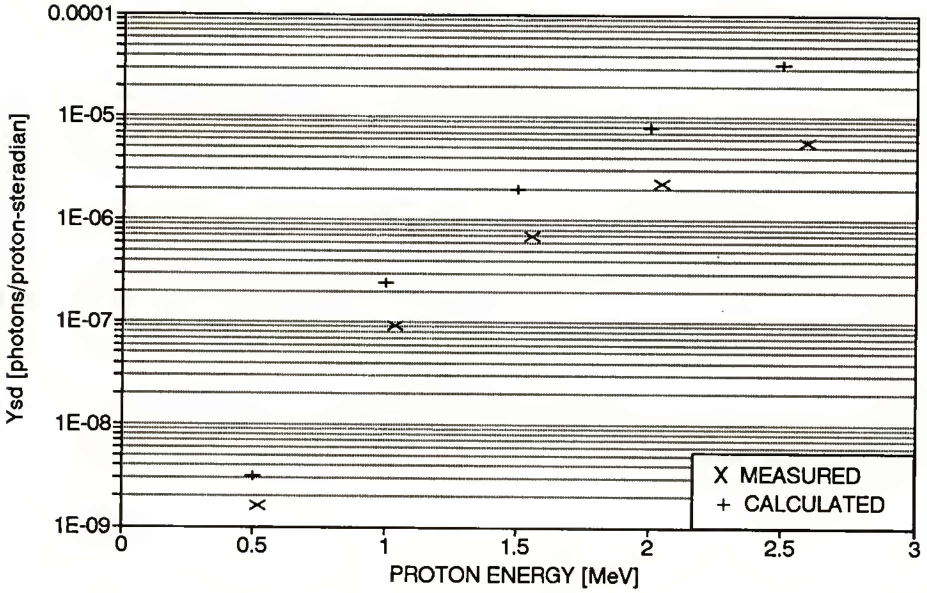

a. Molybdenum

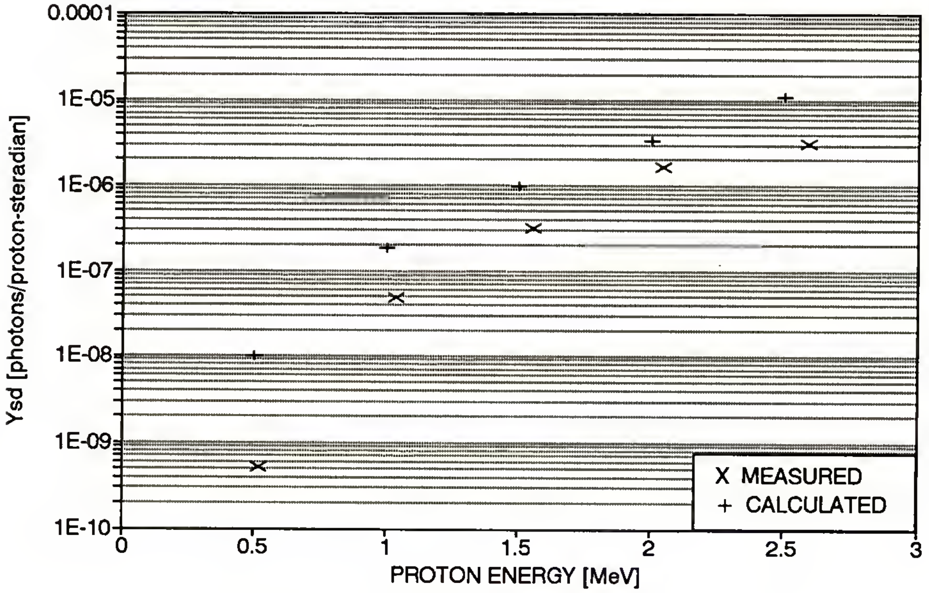

b. Palladium

Figure 7-5. Specific detected photon yields (K-series) for 0.127 mm filiform targets

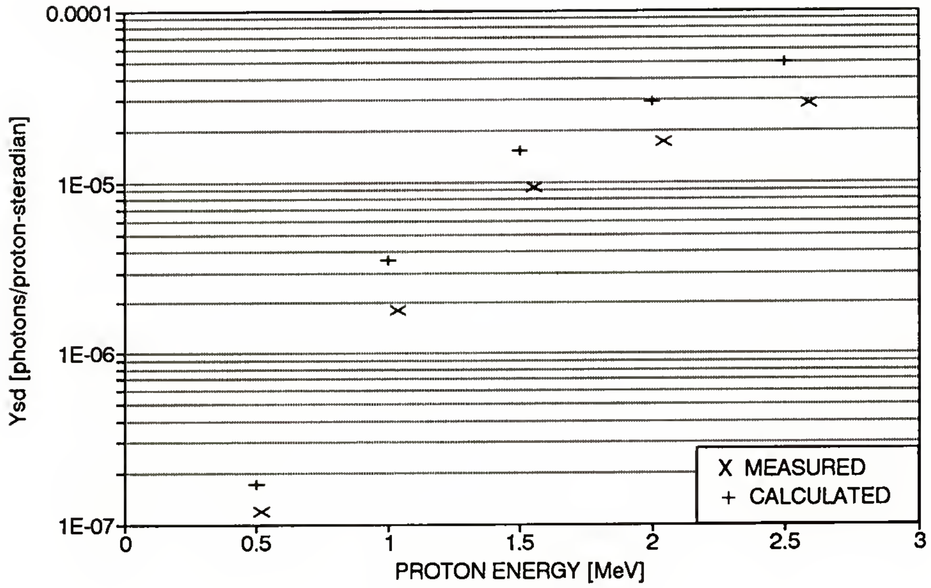

a. Tungsten

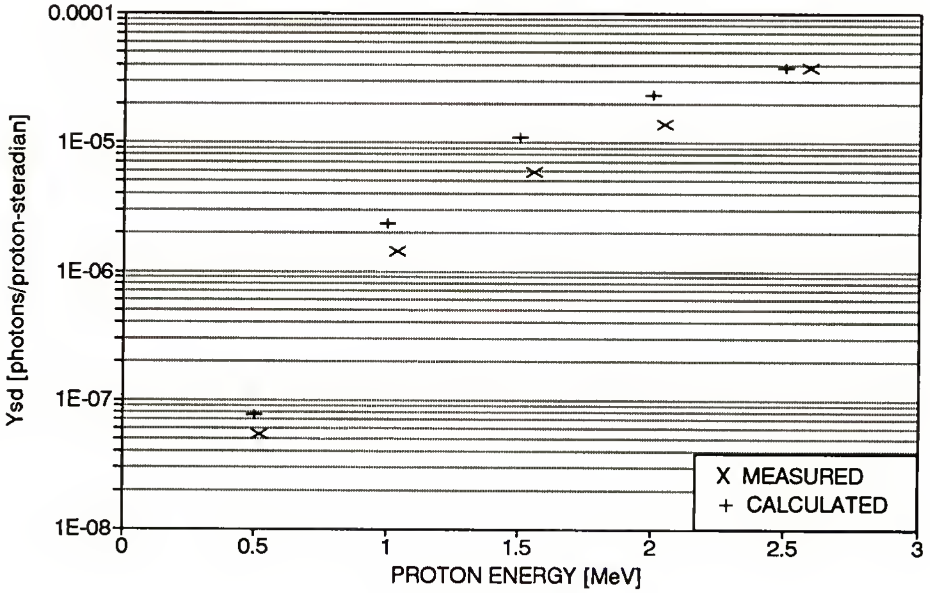

b. Gold

Figure 7-6. Specific detected photon yields (L-series) for 0.127 mm filiform targets

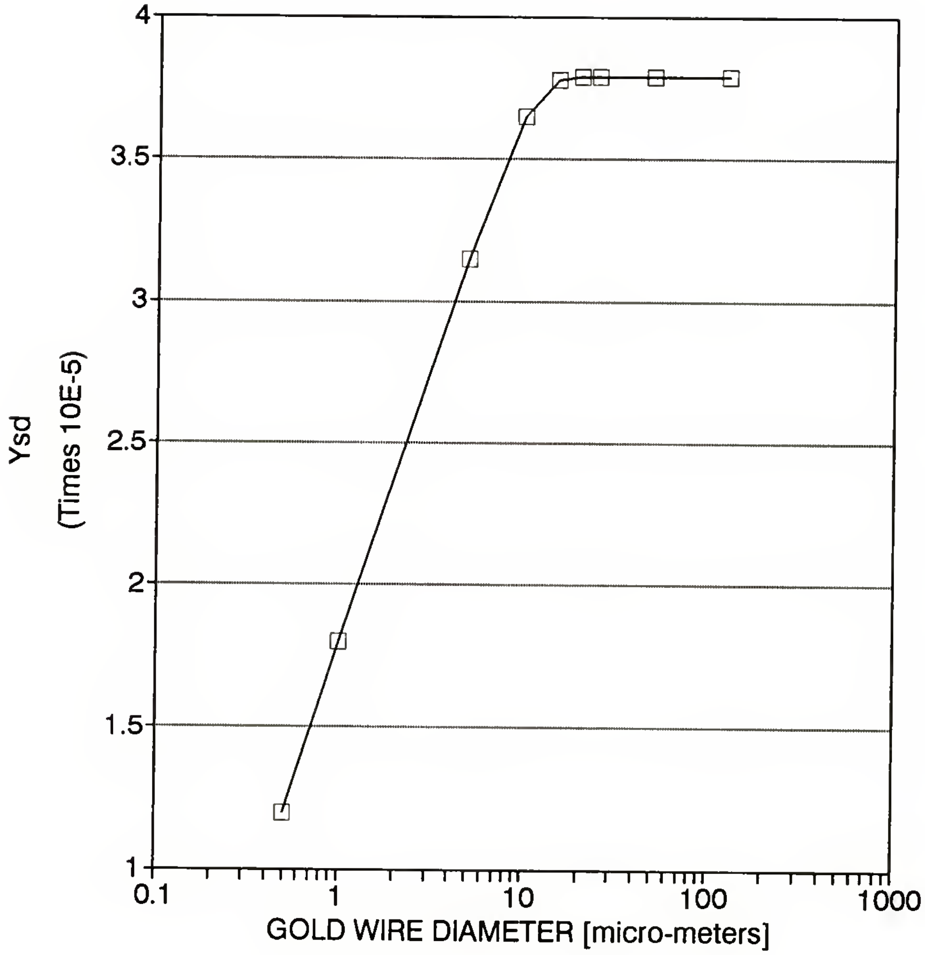

Figure 7-7. Specific detected photon yield as a function of wire diameter

7.2 Calculation of Specific Detected Photon Yields for Thin Gold Wires Excited by High-Energy Protons

One of the potential applications of the multi-element x-ray excitation probe mentioned in Chapter 3, Section 3.4, is as a diagnostic tool in high energy accelerators. If the probe is built with very thin wires, the energy loss of the particles as they interact with it will be a very small percentage of the total energy, particularly for lighter particles. However, because of the high x-ray production cross section of very energetic particles, the value of Y_{sd} will be high. The combination of these characteristics makes the multi-element x-ray excitation probe an attractive diagnostic instrument for this application.

To illustrate this point, specific detected photon yields for 0.001 mm Au wires excited with protons of energies from 8 to 80 MeV were computed. The results are shown in Figure 7-8. The figure also shows the energy lost by the particles expressed as a fraction of E_o.

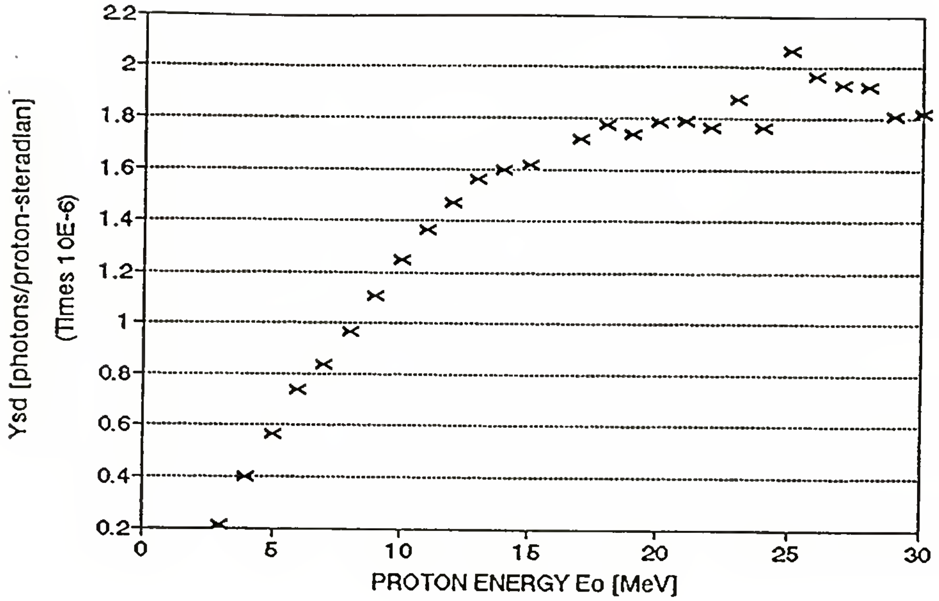

a. Specific detected photon yield vs. proton energy

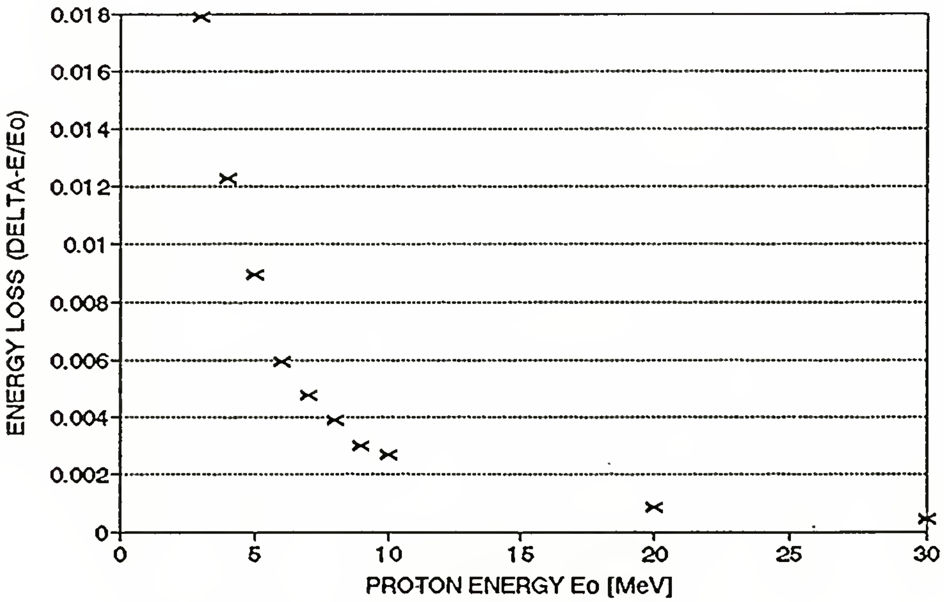

b. Proton energy loss vs. energy

Figure 7-8. Specific detected photon yield and energy loss vs. energy for 0.001 mm gold wires bombarded with high-energy protons

CHAPTER 8
CONCLUSIONS

The characteristic x-ray spectra emitted by pure-element targets excited by energetic particles uniquely identifies the element that radiates them, and the intensity of each of the emitted spectra is directly proportional to the number of particles that strike the targets during a given interval. These two properties are combined in the multi-element x-ray excitation probe method to determine the spatial density distribution of energetic particles. In this method, probes consisting of several pure-element targets are placed in a field of energetic particles--such as the beam of an accelerator--and the emitted radiation is analyzed with a high-resolution x-ray spectrometer. The intensity of each of the characteristic spectra is a measure of the number of particles striking the targets. Usually, only relative measurements are of interest--such as the distribution of particle densities across the beam of an accelerator--but for absolute spatial determinations, the position of each of the targets must be known with respect to a given frame of reference. Similarly, if absolute values of the particle flux or density must be measured, it is necessary to calibrate the probes in experimental conditions closely resembling those of the actual measurement.

The theory of generation of characteristic x-rays by energetic particles is well established. It is based on the theory of interaction of energetic particles with matter, and on the experimental values of ionization and fluorescence yields. The development of the first part of the theory originated in the work of Bohr at the beginning of the century, was significantly advanced by Bethe, and has been further refined in later years by several investigators. A significant body of information on ionization and x-ray production cross-sections exists in the literature; however, there are still substantial gaps in the available data.

Based on this theory, a useful engineering parameter was developed in this work. It is called the intrinsic detected photon yield, and is indicated by the symbol Y_{sd}. This parameter is defined as the number of detected characteristic photons emitted by a target per steradian and per each energetic particle that is intercepted. Y_{sd} relates the number of detected photons X_d (experimentally measured quantity), the number of incident particles P_i (quantity that must be determined), and the solid angle of detection ω according to the expression

$$P_i = \frac{X_d}{Y_{sd}\omega} \qquad (8-1)$$

The determination of P_i consists in measuring X_d with a known solid angle ω and finding the desired value from Equation 8-1. As mentioned above, the value of Y_{sd} used in this equation can be determined experimentally according to the procedure described in Chapter 6, or calculated in the manner discussed in Chapter 7. Y_{sd} is a function of the target material and thickness, of the type and energy of the striking particles, and of the particular physical arrangement (angle between particle beam and target, between target and detector, etc.). Therefore, the values of Y_{sd} determined by calibration of the probes by calculation are specific to the particular set of variables.

Proton, partially ionized molecular hydrogen, and neutralized atomic hydrogen beams were measured using this procedure. A spatial resolution of 10 μm was obtained in some of these measurements. This resolution was limited by the size of the smallest wire that was used in the probes in Chapter 5. The sensitivity of some of the probes was approximately 10^5 protons per square millimeter per second. This sensitivity was limited by the somewhat arbitrary criterion that at least 100 counts had to be accumulated in the spectrometer for a valid measurement. Actually, in some circumstances, even a lower number of counts could yield useful information. Furthermore, in situations in which sensitivity is an important factor, two or three orders of magnitude increase can be attained by a larger solid angle of detection. This can be achieved by using a larger area detector, by using multiple detectors, or by placing the detector(s) closer to the target.

In the experiments described in Chapter 6, the usefulness of the multi-element x-ray excitation probes was demonstrated for the determination of spatial particle distributions. The advantages of the system, such as passivity, remote sensing, low intrusiveness, and relative simplicity of implementation, were also confirmed during the experiments.

The system will be used in the proof-of-principle experiments in the SCFR when the assembly of the array of superconducting magnets has been completed. The manner in which the x-ray probes are intended to be used in the SCFR is discussed in Appendix D.

A logical extension of the measurement performed with the x-ray excitation system is the determination of two dimensional mappings of particle-beam cross sections. One of the possible ways of performing these measurements is to use a probe with multiple parallel filiform targets mounted on a ring that can rotate on a plane perpendicular to the particle beam. The angle of rotation is encoded, and spectra are acquired at a number of angular positions sufficient to generate the data to reconstruct the intensity of the cross section pixels.

Notwithstanding the advantages of the multi-element x-ray excitation probes previously mentioned, the method has the shortcoming of the relatively high cost of the high-resolution x-ray spectrometry necessary for its implementation. Therefore, in cases in which some of the existing methods described in Chapter 2 are adequate no justification may exist to use method developed in this work. On the other hand, when the experimental situation require the measurement of spatial distribution of energetic particles such as those found in the SCFR, or in the profiling of very high energy, low intensity, narrow particle beams, the multi-element x-ray excitation probe may be the required instrument for the application or the instrument of choice because of its unique characteristics.

APPENDIX A
FABRICATION OF THIN SEAMLESS ALUMINUM X-RAY WINDOWS

Introduction

In all the applications of the x-ray probes it will be necessary to place them in hard-vacuum environments (pressures of 10^{-6} Pa or lower). To reach and maintain these vacuum levels, it is necessary to avoid outgassing by the components in the evacuated environment. The standard technique for reaching the required vacuum levels consists in vigorously pumping the system while heating it to several hundred degrees Celsius for several hours until the adsorbed gasses have been released. Therefore, the materials used in the construction of the probe must be capable of withstanding this baking process. The probe frame that will support the wires will be of all-metal construction (aluminum or stainless steel) so no problem is anticipated in this respect. In addition, the window through which the x-rays will escape must be bakeable. Because of this requirement the window must be metallic. Extremely thin windows are necessary because even metals with low x-ray absorption coefficients (beryllium or aluminum) show significant attenuation of low-energy photons.

The lowest attenuation is attained with beryllium.

Percent transmission values of photons by beryllium were computed (Table A-1) using total mass attenuations coefficients from Hubbell [61] and starting from the expression for attenuation of electromagnetic radiation

$$I(t) = I_0 e^{-\frac{\mu_m}{\rho} t} \tag{A-1}$$

where I = radiation intensity after attenuation

t = thickness of attenuating material

I_0 = radiation intensity before attenuation

μ_m = mass attenuation coefficient of material

ρ = density of material

The percent transmitted fraction is found by re-arranging Equation A-1

$$\%\ transmitted = 100 \frac{I}{I_0} = 100\, e^{-\frac{\mu_m}{\rho} t} \tag{A-2}$$

However, the cost of thin beryllium windows is quite high (a 200 mm^2 by 0.127 mm thick window brazed to a stainless steel Conflat® flange costs over two thousand dollars) and they are absolutely necessary only when detecting photons of energies below 6 keV. In most of the applications of the multi-element probe, it is sufficient to detect x-rays of 8 kev (L-lines of tungsten) or higher energy. Therefore, aluminum becomes an acceptable compromise material (see Table A-2 for percent transmission). The cost of brazed thin aluminum windows is not negligible either, amounting to several hundred dollars.

These considerations motivated a search for other solutions to the problem of obtaining bakeable windows with good transmission properties at a reasonable cost.

Table A-1
Percent transmission of photons by beryllium.

X-Ray Energy [keV]	Window Thickness [thousandths of inch]									
	1	2	3	4	5	6	7	8	9	10
1	8	*	*	*	*	*	*	*	*	*
2	73	52	38	27	20	15	10	8	5	4
3	91	83	76	69	63	58	52	48	44	40
4	96	93	89	86	83	80	77	74	71	69
5	98	96	95	93	91	89	87	86	84	83
6	99	98	97	96	95	94	93	92	91	90
8	**	99	99	98	98	97	97	96	96	95
10	**	**	**	99	99	98	98	98	98	97
15	**	**	**	**	**	**	99	99	99	99
	25	51	76	102	127	152	180	203	229	254
	Window Thickness [μm]									

*Less than 1 percent transmission.
**More than 99 percent transmission.

A method for the fabrication of thin aluminum windows consists in compressing aluminum foil between rings of aluminum wire gaskets. This method could be applicable to the SCFR.

However, consideration was given to the possibility of machining seamless thin window/vacuum seal combinations from aluminum discs. Such components would have the inherent advantage of being intrinsically vacuum tight.

Table A-2
Percent transmission of photons by aluminum.

X-Ray Energy [keV]	Window Thickness [thousandths of inch]									
	1	2	3	4	5	6	7	8	9	10
3	1	*	*	*	*	*	*	*	*	*
4	9	1	*	*	*	*	*	*	*	*
5	28	7	2	1	*	*	*	*	*	*
6	47	21	10	5	2	1	*	*	*	*
8	72	51	36	26	18	13	9	7	5	3
10	84	70	59	49	41	35	29	24	20	17
15	95	90	85	81	76	73	68	65	62	58
20	98	95	93	91	89	87	85	83	81	79
30	99	99	98	97	96	96	95	94	93	93
	25	51	76	102	127	152	180	203	229	254
	Window Thickness (μm)									

*Less than 1 percent transmission.

standardized, their cost could be sufficiently reduced to make them disposable.

Here, a fabrication method is described which has been used to machine aluminum windows as thin as 0.005 inch and that has the potential of being used for making even thinner components.

Before describing the method of fabrication of thin aluminum windows, the fabrication of non-bakeable Mylar® windows used in preliminary measurements will be discussed.

Fabrication of Mylar® Windows

The determination of the specific photon yield, $\underline{Y}_{sd}$, for various targets was performed in stainless steel chambers attached to the beam line of the VDG (see Chapters 5 and 6). For these measurements it was not necessary to achieve the low pressures required in the SCFR. Therefore, these experiments were performed at pressures of 10^{-2} to 10^{-4} Pa which could be attained without outgassing the components at high temperature. This allowed the use of x-ray windows made of materials such as Mylar®. The implementation of 0.004" (0.102 mm) Mylar® windows is described here.

Mylar® discs 1.9 inch (48.2 mm) in diameter were cut by hand from overhead transparency stock and sandwiched between two 1.9 inch o.d., 1.45 inch i.d., and 0.09 inch thick (48.2 mm, 36.9 mm, and 2.0 mm, respectively) standard Conflat® copper gaskets; a small amount of high vacuum silicone grease was used to facilitate setting of the parts. This assembly was mounted on the desired port of the vacuum system and compressed between two standard 2.75 inch (69.8 mm) stainless steel Conflat® flanges (Figure A-1).

The assembled x-ray windows were pressure tested with compressed nitrogen and they withstood 110 psig (~7.5 atm.) and several pressurization cycles without catastrophic failure (Figure A-2). However, because a degree of plastic deformation of the Mylar® was observed, the following modification was implemented: the low-pressure side copper gasket was replaced by an aluminum gasket of equal outer

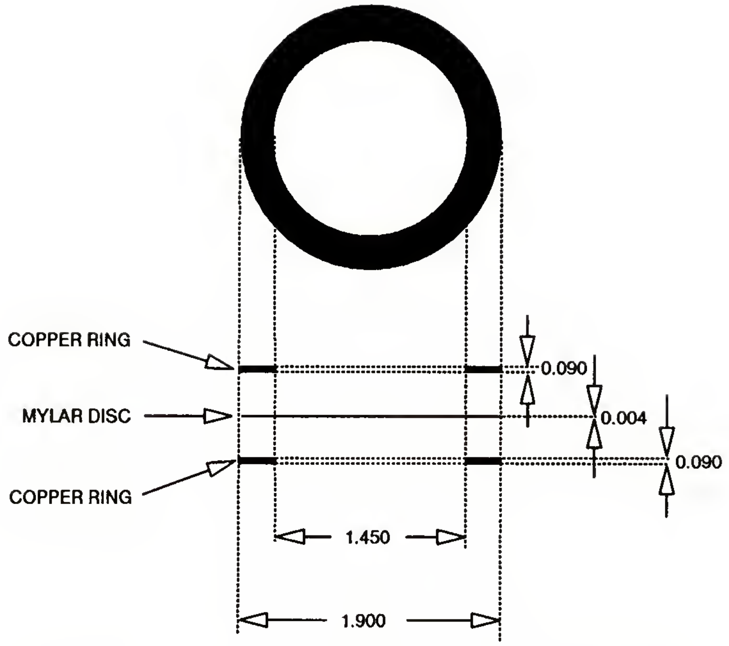

a. Exploded view of main components

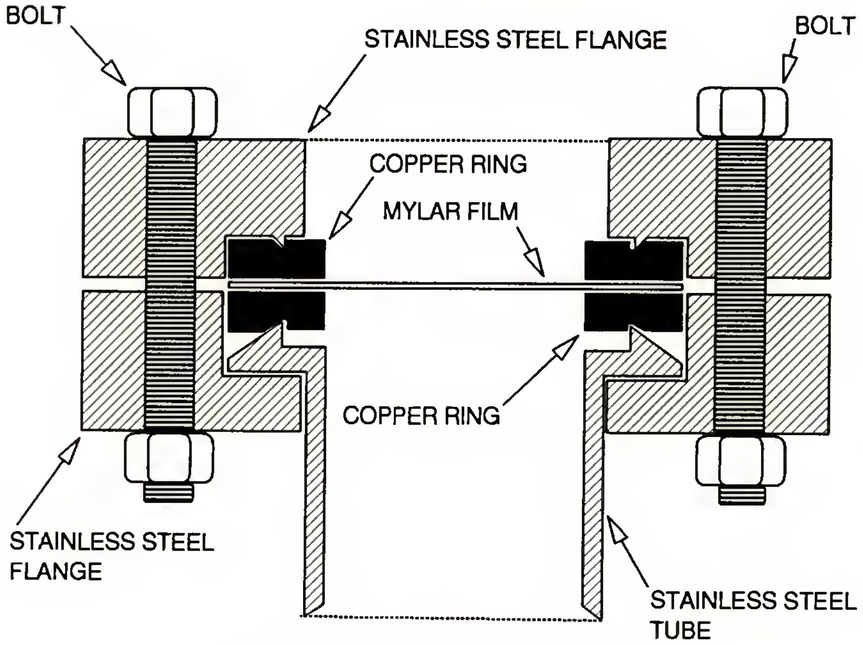

b. Complete window assembly

Figure A-1. Construction of 0.004" Mylar windows

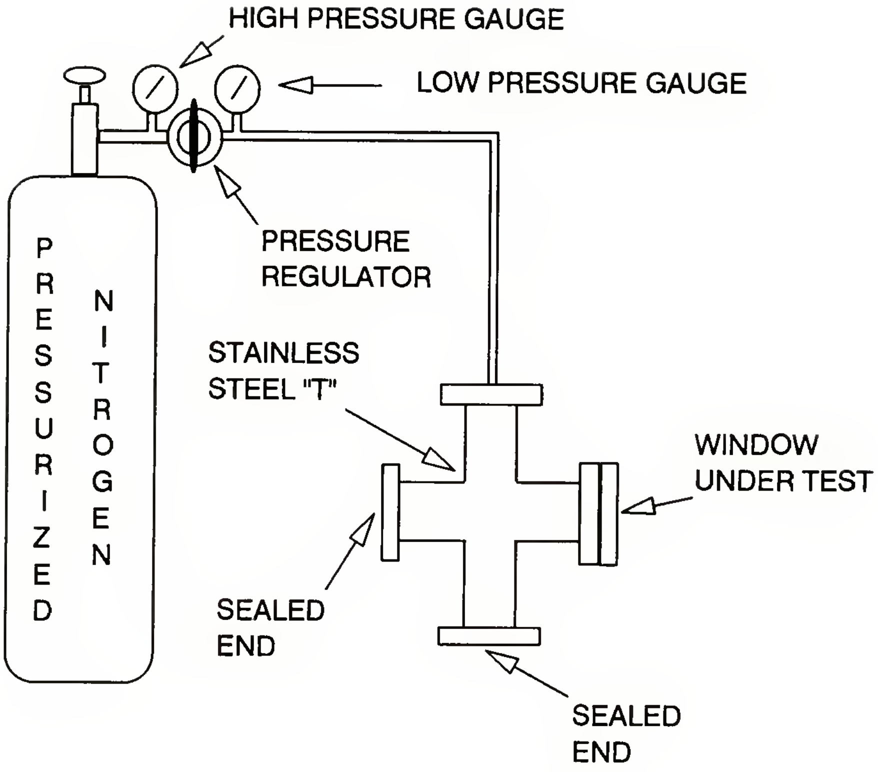

Figure A-2. Setup for pressure-testing of Mylar windows

Table A-3
Percent transmission of photons by Mylar®

X-Ray Energy [keV]	Window Thickness [thousandths of inch]									
	1	2	3	4	5	6	7	8	9	10
1	*	*	*	*	*	*	*	*	*	*
2	29	8	2	1	*	*	*	*	*	*
3	69	46	32	21	15	10	7	5	3	2
4	85	72	61	52	44	38	32	27	23	20
5	92	85	78	72	66	61	56	51	47	44
6	95	91	87	83	79	75	71	68	65	62
8	98	96	94	92	91	89	87	85	84	82
10	99	98	97	96	95	94	93	92	91	90
15	**	99	99	99	98	98	98	98	97	97
20	**	**	**	99	99	99	99	99	98	98
30	**	**	**	**	**	**	**	99	99	99
	25	51	76	102	127	152	180	203	229	254
	Window Thickness [μm]									

*Less than 1 percent transmission.
**Greater than 99 percent transmission.

diameter and equal thickness but with an inner diameter of only 0.5" (12.7 mm). In addition, the edge of the bore was rounded to further reduce concentration of stresses (Figure A-3). Windows of this design were used in the measurements of Y_{sd}.

Fabrication of Aluminum Windows

A procedure for fabricating bakeable thin seamless aluminum window/vacuum gasket combinations is described here.

Aluminum discs larger than the final desired dimension (1.900 inch diameter) were rough cut from sheet metal stock of 1/32 inch nominal thickness. Ten to fifteen discs were compression-chucked between two brass jigs, one held by the jaws of the lathe headstock and the other by a live center inserted in the tailstock (Figure A-4). The resulting discs were the window blanks.

A special jig was built to support the blanks during the machining operations (Figure A-5). The jig was machined from 4-inch diameter cold-rolled round steel stock. The purposes of the jig are:

1. To hold the work firmly with its surface perpendicular to the axis of rotation and parallel to the direction of travel of the cutting tool.
2. To provide a firm supporting surface against the pressure of the cutting tool edge.
3. To allow for quick and reproducible setup.

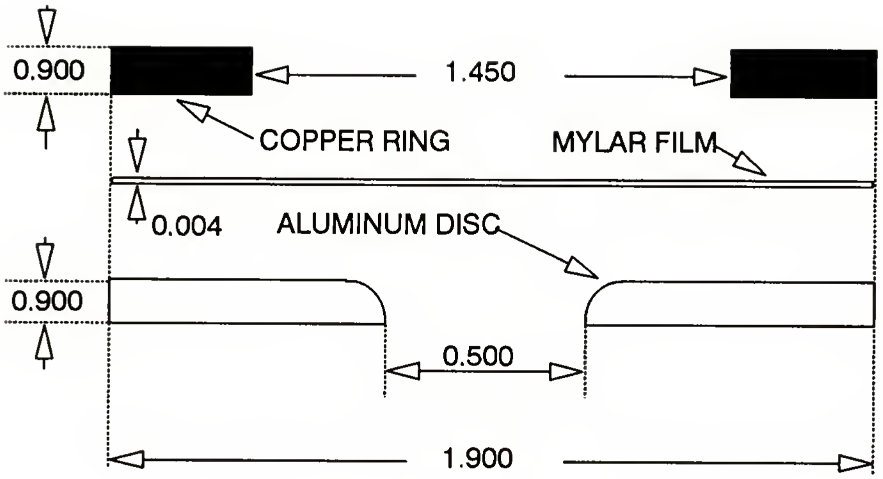

Figure A-3. Exploded view of Mylar window modified with aluminum disc

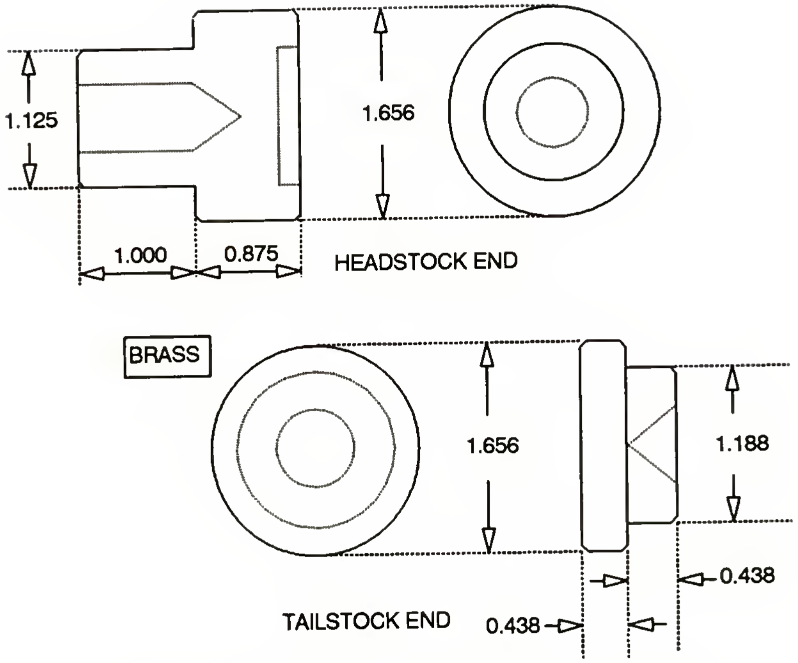

a. Details of compression chuck

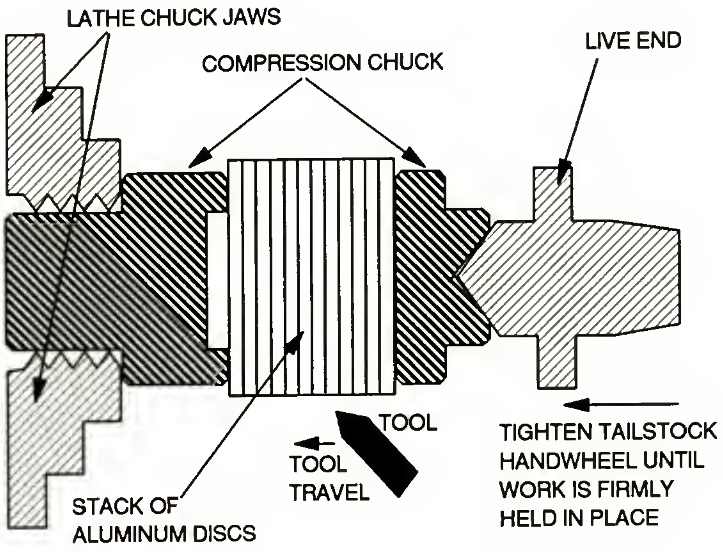

b. Setup for machining blanks

Figure A-4. Fabrication of aluminum blanks

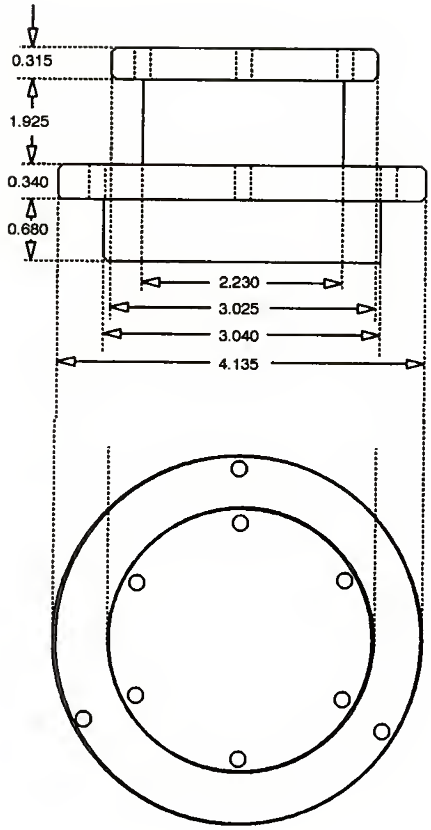

a. Base

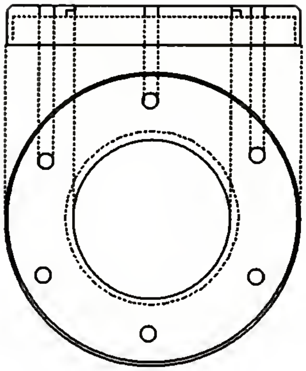

b. Fastening ring

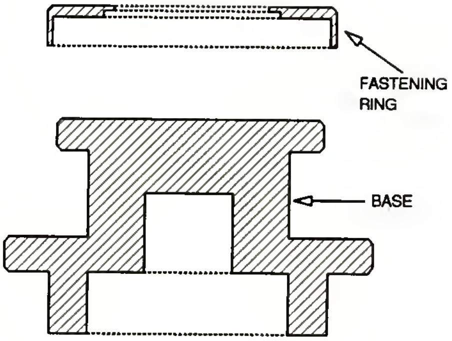

c. Longitudinal section

Figure A-5. Jig for machining thin aluminum windows (material: cold rolled steel)

The working surface of the jig was machined to a ±0.0001 inch tolerance.

The machining of the windows begins by mounting the jig on a three- or six-jaw chuck, with the three alignment screws are approximately centered with the jaws and, fully retracted. Pushing the jig against the front surface of the chuck, the chuck is tightened until it just holds the jig in place. Using a dial gauge mounted on the tool rest and pushing the gauge plunger against the working surface of the jig near its edge, the chuck is turned by hand to verify that the working surface is perpendicular to the axis of rotation; a gauge capable of indicating .0001 inch should be used for this operation. If the surface is found to be out of perpendicularity, it should be checked to ensure that the collar is actually butting the chuck. If a discrepancy is still detected, the alignment screws can be used to correct it. Once the jig is aligned, the chuck is tightened a bit more and the alignment is rechecked. These last operations are repeated as necessary until the jig is firmly held.

The next operation consists in verifying that the direction of travel of the cutting tool is parallel to the working surface. With the dial gauge mounted on the tool rest and the gauge plunger touching the working surface, the cross slide is moved back and forth along the diameter of the working surface (Figure A-6). Since the carriage is factory-aligned and has no means of adjustment, a discrepancy here is probably due to improper leveling of

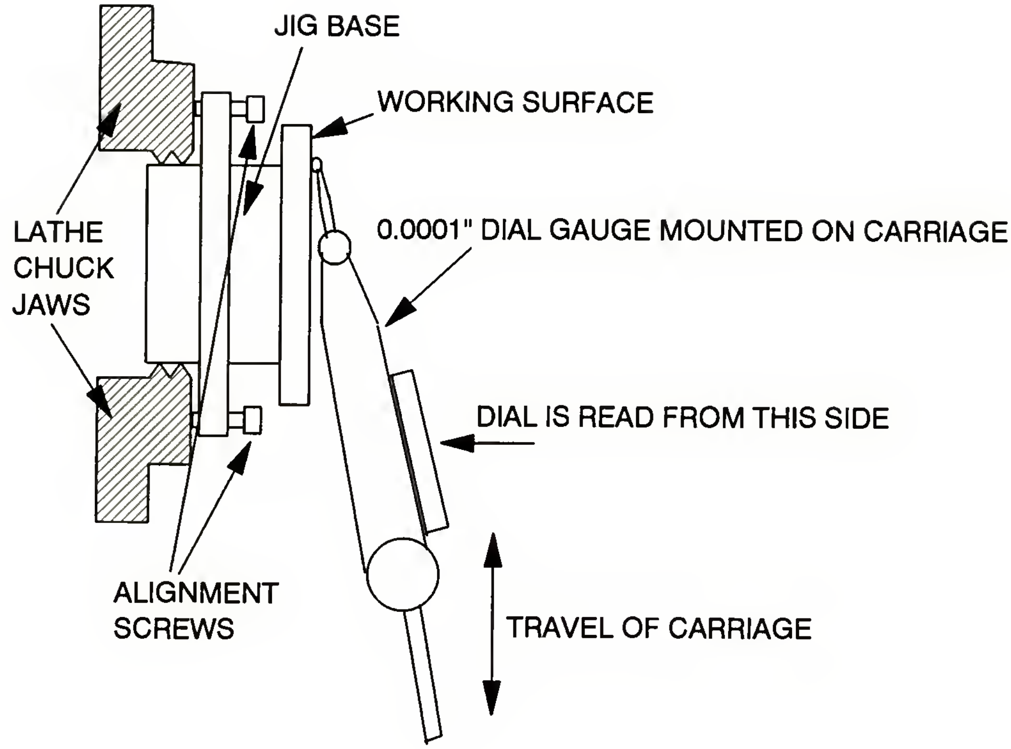

Figure A-6. Alignment of the jig

the lathe.

Next, a blank whose thickness has been accurately measured with a .0001 inch micrometer is mounted on the working surface and held in place with the mounting ring. This is fastened to the jig by six screws tightened in a star pattern (Figure A-7). The blank is now ready to be machined.

Before beginning the cutting operation, it is necessary to make a baseline measurement to know how much material is left after each cut. A depth gauge is placed on a diameter against the outer surface of the mounting ring; this diameter must be marked for future reference. The plunger of the gauge is gently inserted until it touches the outer surface of the blank and the reading is recorded. This initial reading IR corresponds to the initial blank thickness IT. As material is removed from the blank in successive cuts, new readings R of the depth gauge are used to determine how much thickness T is left in the blank (Figure A-8):

$$T = IT - (R - IR) \tag{A-3}$$

A freshly sharpened diameter tool is used to machine the blank. The cutting tool is mounted on the tool rest in the manner shown in Figure A-9. The tip of the tool is placed at a distance from the center of the blank equal to the radius of the window to be fabricated. The compound feed is then used to bring the tip of the tool to a point

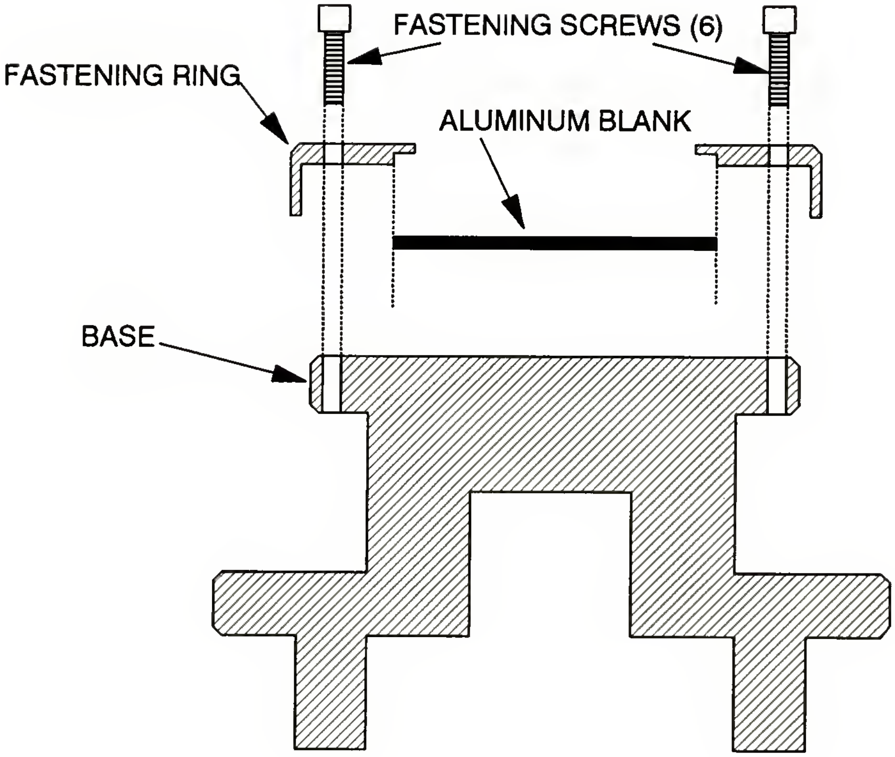

Figure A-7. Mounting the blank on the jig

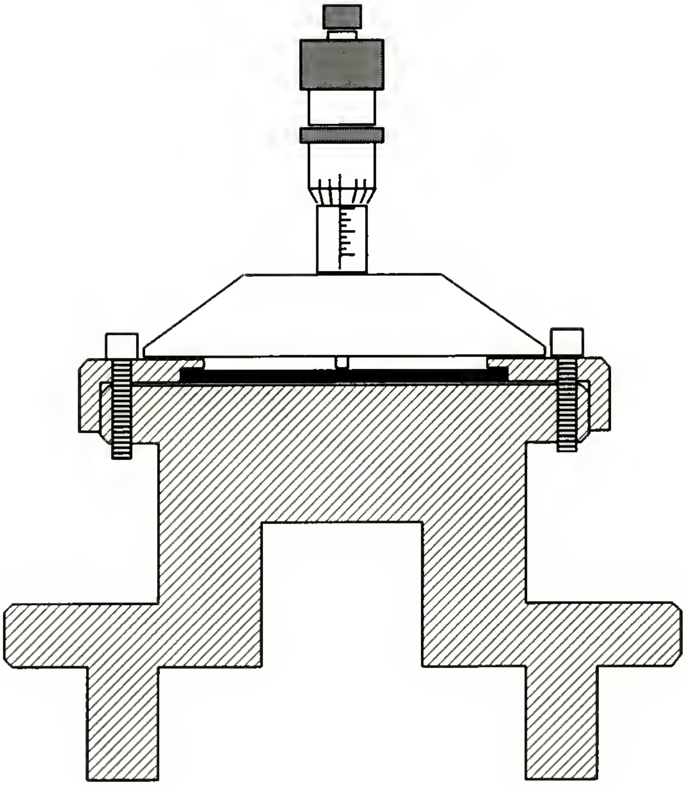

Figure A-8. Measuring the baseline with the depth gauge before beginning the cutting operation

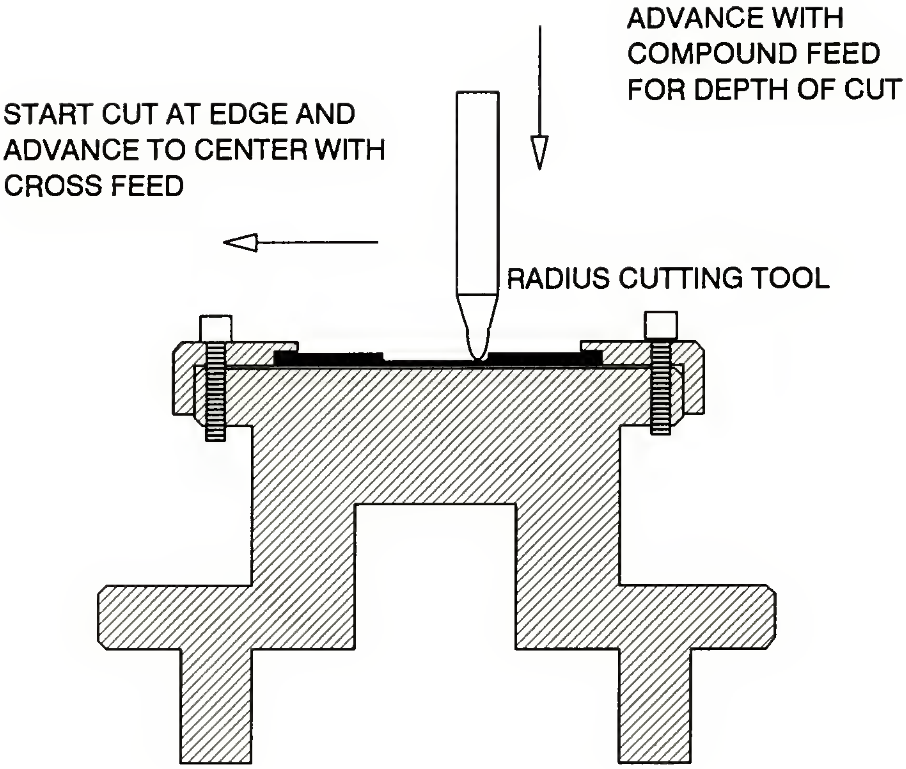

Figure A-9. Window cutting operation

almost in contact with the blank. The lathe is started and the tool is moved in until it just touches the surface of the work. At this point the reading on the dial of the compound feed is recorded. At the beginning, it is possible to make cuts of two or three thousandths of an inch, but as a remaining thickness of 0.010 inch is approached the cuts should be limited to 0.001 inch per pass. After each pass, the remaining thickness is verified by the dial reading on the compound feed and with the depth gauge as indicated above. With this method it is possible to attain a window thickness of ten or even eight thousandths of an inch without great difficulty. Below this thickness, it is necessary to take precautions to avoid ripping the thin film of remaining material. To fabricate windows as thin as 0.005 inch, a well-honed small radius tool and cuts of approximately 0.0005 inch are required. However, with some practice, windows of this thickness can be fabricated.

As indicated in Table A-2, 0.005 inch aluminum windows have an 18 percent transmission for 8 keV photons, so these windows will be adequate for most applications of the multi-element probe.

When it is necessary to detect lower-energy photons, it should be possible to reduce the thickness of the windows by abrasion on a sanding table using successively finer grit paper. A special holder will be required for this operation to ensure that the sanding action is uniform over the whole surface of the aluminum disc.

APPENDIX B
SPECIFICATIONS AND CALIBRATION CERTIFICATE OF THE K485 CURRENT METER

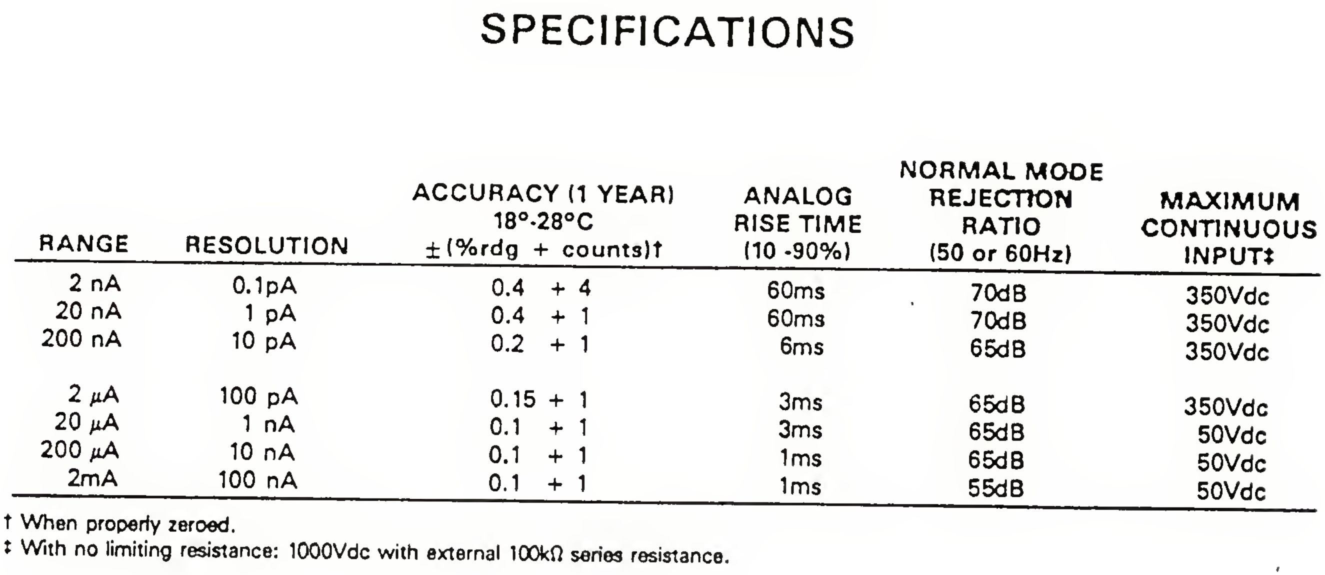

SPECIFICATIONS

RANGE	RESOLUTION	ACCURACY (1 YEAR) 18°-28°C ±(%rdg + counts)†	ANALOG RISE TIME (10 -90%)	NORMAL MODE REJECTION RATIO (50 or 60Hz)	MAXIMUM CONTINUOUS INPUT‡
2 nA	0.1pA	0.4 + 4	60ms	70dB	350Vdc
20 nA	1 pA	0.4 + 1	60ms	70dB	350Vdc
200 nA	10 pA	0.2 + 1	6ms	65dB	350Vdc
2 μA	100 pA	0.15 + 1	3ms	65dB	350Vdc
20 μA	1 nA	0.1 + 1	3ms	65dB	50Vdc
200 μA	10 nA	0.1 + 1	1ms	65dB	50Vdc
2mA	100 nA	0.1 + 1	1ms	55dB	50Vdc

† When properly zeroed.

‡ With no limiting resistance: 1000Vdc with external 100kΩ series resistance.

Figure B-1. Specifications of the K485 current meter

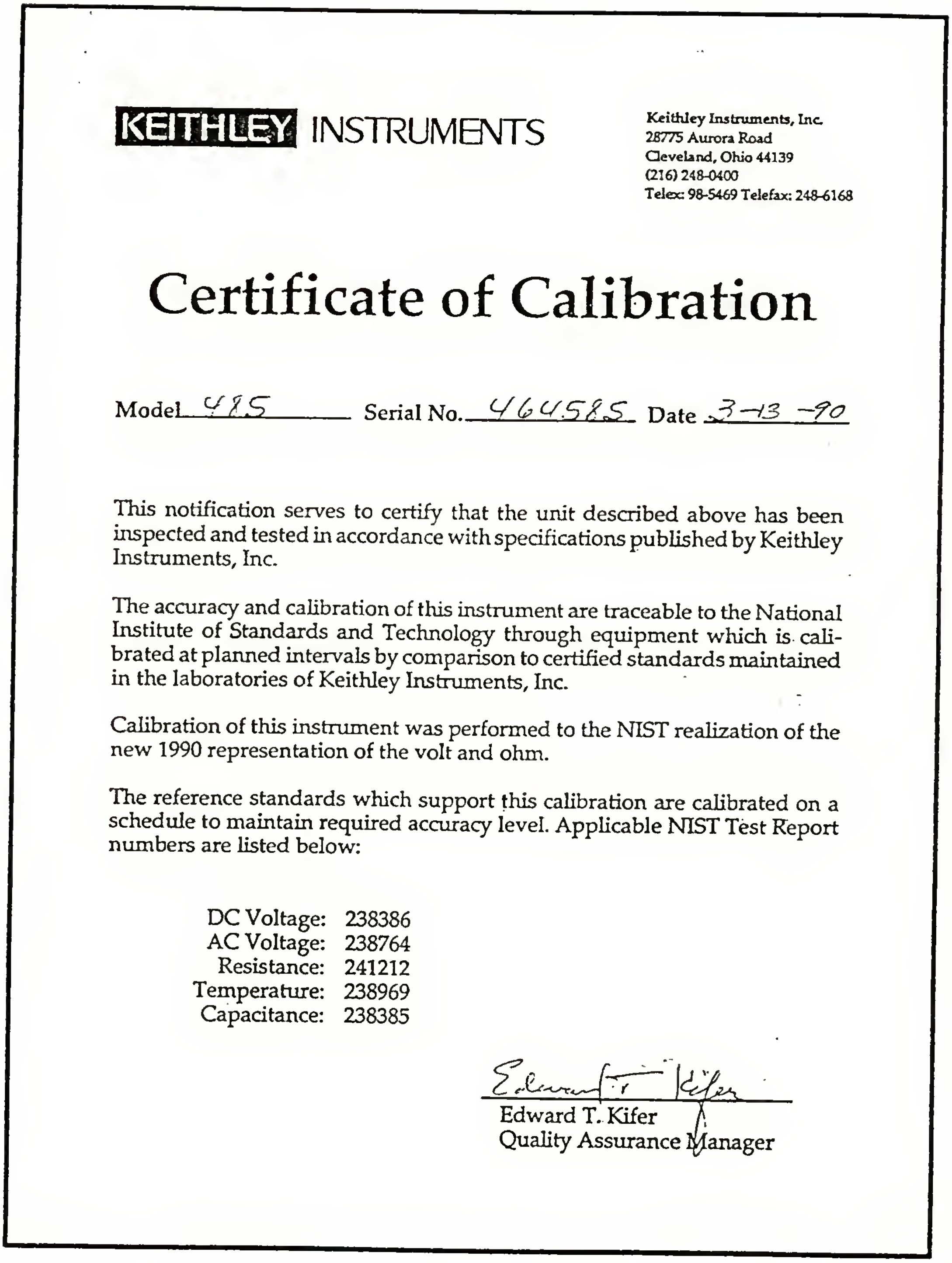

KEITHLEY INSTRUMENTS

Keithley Instruments, Inc.
28775 Aurora Road
Cleveland, Ohio 44139
(216) 248-0400
Telex: 98-5469 Telefax: 248-6168

Certificate of Calibration

Model 485 Serial No. 464585 Date 3-13-90

This notification serves to certify that the unit described above has been inspected and tested in accordance with specifications published by Keithley Instruments, Inc.

The accuracy and calibration of this instrument are traceable to the National Institute of Standards and Technology through equipment which is calibrated at planned intervals by comparison to certified standards maintained in the laboratories of Keithley Instruments, Inc.

Calibration of this instrument was performed to the NIST realization of the new 1990 representation of the volt and ohm.

The reference standards which support this calibration are calibrated on a schedule to maintain required accuracy level. Applicable NIST Test Report numbers are listed below:

DC Voltage:	238386
AC Voltage:	238764
Resistance:	241212
Temperature:	238969
Capacitance:	238385

Edward T. Kifer

Edward T. Kifer
Quality Assurance Manager

Figure B-2. Calibration certificate of the K485 current meter

APPENDIX C
DATALOG FORM

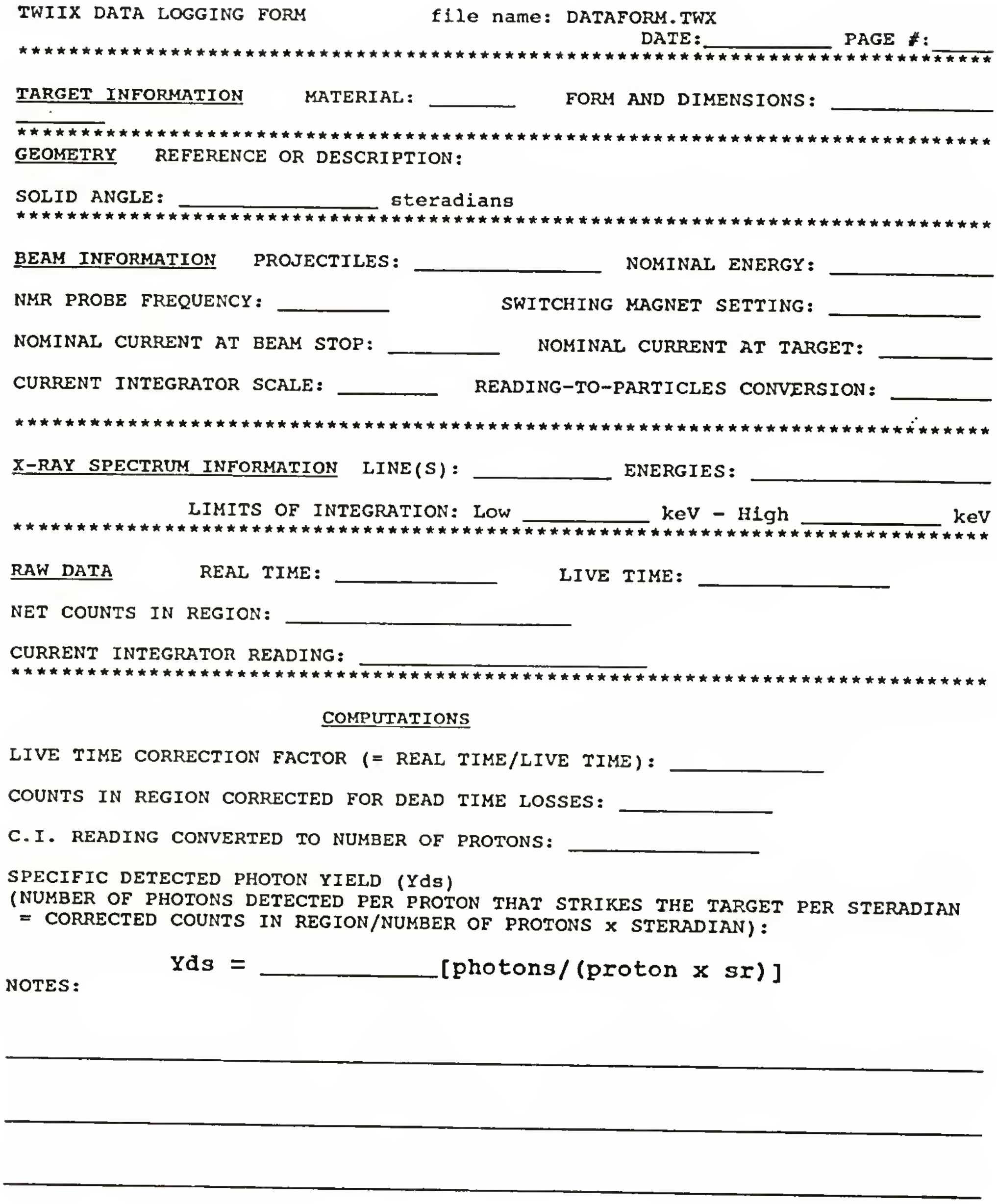

TWIIX DATA LOGGING FORM file name: DATAFORM.TWX

DATE:__________ PAGE #:_____

****

TARGET INFORMATION MATERIAL: _______ FORM AND DIMENSIONS: ______________________

****

GEOMETRY REFERENCE OR DESCRIPTION:

SOLID ANGLE: ________________ steradians

****

BEAM INFORMATION PROJECTILES: _______________ NOMINAL ENERGY: __________

NMR PROBE FREQUENCY: _________ SWITCHING MAGNET SETTING: __________

NOMINAL CURRENT AT BEAM STOP: _________ NOMINAL CURRENT AT TARGET: _________

CURRENT INTEGRATOR SCALE: ________ READING-TO-PARTICLES CONVERSION: ______

****

X-RAY SPECTRUM INFORMATION LINE(S): _________ ENERGIES: ______________

LIMITS OF INTEGRATION: Low __________ keV - High ___________ keV

****

RAW DATA REAL TIME: _____________ LIVE TIME: _______________

NET COUNTS IN REGION: _______________________

CURRENT INTEGRATOR READING: _______________________

****

COMPUTATIONS

LIVE TIME CORRECTION FACTOR (= REAL TIME/LIVE TIME): ____________

COUNTS IN REGION CORRECTED FOR DEAD TIME LOSSES: ____________

C.I. READING CONVERTED TO NUMBER OF PROTONS: _______________

SPECIFIC DETECTED PHOTON YIELD (Yds)
(NUMBER OF PHOTONS DETECTED PER PROTON THAT STRIKES THE TARGET PER STERADIAN
= CORRECTED COUNTS IN REGION/NUMBER OF PROTONS x STERADIAN):

Yds = ______________[photons/(proton x sr)]

NOTES:

____

____

____

Figure C-1. Datalog form

APPENDIX D
USE OF X-RAY EXCITATION PROBES IN SCFR MEASUREMENTS

In this appendix, an example is given of how x-ray excitation probes can be used to perform some of the measurements required in the SCFR. The chosen application is the determination of the optimum settings of the superconducting magnets to obtain the desired radial and axial focusing effects described in Chapter 2. In the following discussion, it will be assumed that the array of superconducting magnets is of the type shown in Figure 2-3, that the desired trajectories of the particles are similar to those illustrated in Figure 2-4 (this implies that the energy of the particles is within the range that allows the magnetic field to contain them within the experimental chamber), and that the method of off-center injection shown in Figure 2-7a is used. Although the magnetic field configuration shown in Figures 2-2 and 2-3 is highly idealized —regions of high-field and regions of zero-field values—, it significantly simplifies the discussion of the process. The basic points of the present application of the probes are not substantially altered by assuming more complex field configurations that resemble more closely those to be expected in the SCFR.

Another assumption that will be made in the section on radial focusing is that the measurements will be made with a single-wire filiform probe parallel to the z-axis. The probe can be placed in any radial position within the chamber.

1. Adjustment of Radially Focusing Magnet

The absolute and relative intensities of the magnetic fields generated by solenoid sets #1 and #3 (Figure 2-2b) determine the shape of the trajectories of the chosen particles on a radial plane. Here, it will be assumed that the current of solenoid set #1 has been set to a given value ——the maximum allowed by the winding, for instance—— and that the current of solenoid set #3 can be changed at will to yield the desired effect of producing center-intersecting trajectories. The effect of increasing this current from zero to a high value on the shape of the trajectories and the corresponding response of the probe will be analyzed,

When field #3 is zero, the overall field configuration is that shown in Figure 2-2a. In this case, the particles are forced to describe tight circular orbits close to the point of entry. A filiform probe parallell to the z-axis introduced in such a distribution, will detect particles only if it intersects these circular orbits. If field #3 is gradually increased, a point is reached when the region where B = 0 (Figure 2-2b) intersects the orbits of the particles. At that point, the particles are able to escape the high-field region and travel on a straight line through the zero-field region until they penetrate again the high-field region and their directions of travel are once more changed. This process is repeated many times causing the particles to describe trajectories contained within a ring around the origin. A probe will detect particles only if placed within the boundaries of this ring. As the value of field #3 continues to be incremented, the width of the ring increases at the expense of decreasing the radius of the central particle-free region. A radial motion of the probe will indicate this effect by detecting particles within the ring but not in the central region. Eventually, field #3 reaches the desired value and the particles travel in center intersecting trajectories. At this point, a probe placed in the vicinity of the of the origin will indicate this condition also. Finally, if field #3 is increased still further, the trajectories revert to a ring configuration —they will not intersect at the center— and the probe will detect no particles if placed near the z-axis. What has just been described is the process of going from an underfocused condition —low value of field #3— through correct focusing and, finally, to an overfocused condition —high value of field #3—.

It is important to notice that when the probe is used in this application, it acts as a sink for all the particles that are injected in the system. That is, if the probe is placed in any point within a region that contains orbiting particles it will reach a steady state in which it will detect all particles that are introduced. Conversely, if placed outside this region, it will detect nothing. Therefore, the adjustment of field #3 can be performed by placing the probe near the center of the distribution and adjusting the current through solenoid set #3 until x-rays from the probe target are detected. By minute radial motions of the probe, it should also be possible to determine where the actual center of the distribution (the z-axis) is located.

2. Adjustment of Axially Focusing Magnet

The magnetic field component necessary to produce axial focusing is created by the introduction of solenoid #2. After solenoid #3 has been adjusted with the previously described procedure, it is therefore necessary to adjust solenoid #2 to attain optimum radial focusing. A special probe consisting of a short wire parallel to the z-axis mounted only at one end can be constructed for this purpose. The probe will be mounted on a micromanipulator with two degrees of fredom: radial and axial. With such a probe, the contour of the concave disk formed by the orbiting particles can be traced. In this manner, the current in solenoid #2 can be adjusted for optimum axial focusing.

REFERENCES

[1] S. Anghaie, R. Coldwell, H. Monkhorst, C. Stodden, A. Velenik, and R. Williams, "Self-Collider Fusion Reactor (SCFR) with Direct Energy Conversion," First ARG Meeting, April 21, 1989, Gainesville, Fla.

[2] H. Monkhorst, S. Anghaie, and R. Coldwell, "The Self-Collider Fusion Reactor: Principles and Performance," (in preparation, 1991).

[3] R.L. Coldwell, Report on Migma Simulations, Department of Physics, University of Florida, Gainesville, Fla., August 10, 1988.

[4] R.L. Williams, Master's Thesis, Nuclear Engineering Sciences Department, University of Florida, Gainesville, Fla., 1991 (in preparation).

[5] R. Stensgaard and T. Korsbjerg, "An automated beam-scanner system," Nuclear Instruments and Methods, 184, p. 197 (1981).

[6] J.H. Meier and F.W. Richter, "Strahlabtastsystem für Teilchenbeschleuniger," Nuclear Instruments and Methods, 134, p. 213 (1976).

[7] J.L. Duport and S. Jaccard, "A compact beam scanner in immediate vicinity of the target," Nuclear Instruments and Methods, 115, p. 233 (1974).

[8] C.D. Bond and S.E. Gordon, "A wide aperture high gain beam profile scanner," Nuclear Instruments and Methods, 98, p. 513 (1972).

[9] H.E. Wegner and I.L. Feigenbaum, "High current beam scanner," IEEE Transactions on Nuclear Science, NS-14, p. 1099 (1967).

[10] J.W. Jagger, J.G. Page, and P.J. Riley, "A simple ion beam scanner," Nuclear Instruments and Methods, 49, p. 121 (1967).

[11] G. Hortig, "A beam scanner for two dimensional scanning with one rotating wire," Nuclear Instruments and Methods, 30, p. 355 (1964).

[12] J. Takacs, "Beam scanner for the Oxford electrostatic tandem accelerator," IEEE Transactions on Nuclear Science, NS-12, p. 980 (1965).

[13] K.O. Nielsen and O. Skilbird, "Continuous scanning in two directions of the ion beam in an electromagnetic isotope separator," Nuclear Instruments and Methods, 1, p. 159 (1957).

[14] G. Stover and K. Fowler, "Operating results for the beam profile monitor system currently in use at Bevalac facility," IEEE Publication CH2387-9/87/0000 -0622, p. 622 (1987), U.S. DOE Contract No. DE-AC03 -76SF00098.

[15] F.W. Martin and R. Golosokie, "Achromatic proton microbeams," Nuclear Instruments and Methods in Physics Research, 197:1, p. 111 (1982).

[16] C. Fields, "Problems in measuring micron size beams," Proceedings of the 1989 IEEE Particle Accelerator Conference, vol. 1, p. 60 (1989).

[17] K.W. Struve, F.W. Chambers, E.J. Lauer, and D.R. Slaughter, "X-ray beam size measurements on the advanced test accelerator," UCRL Preprint No. 93781 (1986).

[18] D.D. Jenson, M.W. Hill, and N.F. Mangelson, "Prediction of particle beam distribution on PIXE targets," Nuclear Instruments and Methods in Physics Research, B10/11, p. 674 (1985).

[19] J. Bosser, J. Camas, L. Evans, G. Ferioli, J. Mann, O. Olsen, and R. Schmidt, "The Micron Wire Scanner at SPS," 1987 IEEE Particle Accelerator Conference, vol. 1, p. 783 (1987).

[20] R.W. Odom, M.D. Strathman, S.E. Butrill, r., and S.M. Baumann, "Nondestructive Imaging Detectors for Energetic Particle Beams," Nuclear Instruments and Methods in Physics Research, B44, p. 465 (1990)

[21] M.C. Ross, "Beam diagnostics and control for SLC," Proceedings of the 1987 IEEE Particle Accelerator Conference, vol. 1, p. 508 (1987).

[22] P. Kuske, K. Derikum, H.G. Hoberg, and H. Lehr, "Beam position and profile measurements at BESSY," Proceedings of the 1987 IEEE Particle Accelerator Conference, vol. 1, p. 535 (1987).

[23] R. Webber, J. Fritz, S. Holmes, W. Marsh, and J. Zagel, "A beam position monitoring system for the Fermilab booster," Proceedings of the 1987 IEEE Particle Accelerator Conference, vol. 1, p. 541 (1987).

[24] R.W. Coombes and D. Neet, "Beam monitors based on light observation for the beam switchyard of the Stanford two-mile linear accelerator," IEEE Transactions in Nuclear Science, vol. 4, No. 3, p. 1111 (1967).

[25] D. Beavis, R. Debbe, M.J. LeVine, J.H. Van Dijk and H.E. Wegner, "A CCD beam profile monitor for 14.6 GeV/amu ^{16}O ions," Proceedings of the 1987 IEEE Particle Accelerator Conference, vol. 1, p. 707.

[26] A.A. Hasan, C.L. Fink and M.G. Rosing, "A beam characterization of H^- particles," Proceedings of the 1989 IEEE Particle Accelerator Conference, vol. 3, p. 1504 (1989).

[27] T.J. Yule, F.O. Bellinger, T.A. Coleman, M.M. Faber, C.L. Fink, and C.T. Roche, "Beam characterization with video imaging systems at the ANL 50 MeV H^- beamline," Proceedings of the 1989 IEEE Particle Accelerator Conference, vol. 3, p. 1571 (1989).

[28] A.M. Ferrari and S. Anghaie, "Particle density measurements in beam-confinment fusion systems," Transactions of the American Nuclear Society Annual Meeting, Orlando, Fla., p. 106 (1991).

[29] H. Geiger and E. Marsden, "On a diffuse reflection of the α-particles," Proceedings of the Royal Society of London, Series A, 82, p. 495 (1909).

[30] H. Geiger, "The scattering of α-particles by matter," Proceedings of the Royal Society of London, Series A, 83, p. 492 (1909).

[31] R.D. Evans, The Atomic Nucleus (McGraw-Hill Book Company, Inc., N.Y., 1955), p. 568.

[32] R.E. Lapp and H.L. Andrews, Nuclear Radiation Physics (Prentice-Hall, Inc., Englewood Cliffs, N.J., 1972), p. 261.

[33] E. Rutherford, "The Scattering of α and β particles by matter and the structure of the atom," Philosophical Magazine and Journal of Science, 6th series, 21, 1911, p. 669.

[34] N. Bohr, "On the theory of the decrease of velocity of moving electrified particles on passing through matter," Philosophical Magazine and Journal of Science, 6th series, 25, 1913, p. 10.

[35] N. Bohr, "On the decrease of velocity of swiftly moving electrified particles in passing through Matter," Philosophical Magazine and Journal of Science, 6th series, 30, 1915, p. 581.

[36] P. Sigmund and K. B. Winterborn, "Energy loss spectrum of swift charged particles penetrating a layer of materials," Nuclear Instruments and Methods in Physics Research, B12, p. 1 (1985).

[37] H. Geissel, W. N. Lennard, H. R. Andrews, D. P. Jackson, I. V. Mitchell, D. Phillips, and D. Ward, "Energy-angle distribution measurements for $0.8\underline{v}_0$ ^{20}Ne and ^{209}Bi ions penetrating thin carbon foils," Nuclear Instruments and Methods in Physics Research, B12, p. 38 (1985).

[38] E. Segre, Nuclei and Particles (W.A. Benjamin, Inc., New York, 1964), p. 44.

[39] H.A. Bethe, "Bremsformel für Elektronen relativistischer Geschwindigkeit", Z. Phyzik, 76 (1932), p. 293.

[40] H.H. Andersen and J.F. Ziegler, The Stopping and Ranges of Ions in Matter (Pergamon Press, N.Y., 1977)

[41] E.P. Bertin, Introduction to X-Ray Spectrometric Analysis (Plenum Press, N.Y., 1978).

[42] R. Jenkins, X-Ray Fluorescence Spectrometry (John Wiley & sOns, Inc., N.Y., 1988).

[43] I.V. Mitchell and J.F. Ziegler, "Ion-induced X-Rays," in Ion Beam Handbook for Material Analysis (J. W. Mayer and E. Rimini, eds., Academic Press, Inc., N.Y., 1977).

[44] E. Eichinger and P.J. O'Reilly, "K-shell x-ray production in vanadium, cobalt, copper, molybdenum and silver by low-velocity protons," Nuclear Instruments and Methods in Physics Research, B47, p. 355 (1990).

[45] A. Bieńkowski, J. Braziewicz, T. Czyżewski, Ł. Głowacka, M. Jaskþła, G. Lapicki and M. Pajek, "M-sell x-ray production in heavy elements by low-energy protons," Nuclear Instruments and Methods in Physics Research, B49, p. 19 (1990).

[46] D.D. Cohen, "K and L shell x-ray cross sections for use in PIXE analysis systems," Nuclear Instruments and Methods in Physics Research, B49, p. 1 (1990).

[47] H. Mohan, P.S. Singh, H.R. Verma and C.S. Khurana, "Proton induced L-shell x-ray production cross sections for Pb in the energy range 225-400 keV," Nuclear Instruments and Methods in Physics Research, B26, p. 507 (1987).

[48] D.K. Marble, J.D. Gressett, E.D. McDaniel, J.L. Duggan and J.F. Culwell, "L-shell x-ray production in copper, germanium, rubidium, strontium and yttrium by 100-225 keV protons," Nuclear Instruments and Methods in Physics Research, B40/41, p. 98 (1989).

[49] J.D. Gressett, D.K. Marble, E.D. McDaniel, J.L. Duggan and J.F. Culwell, "M-shell x-ray production in gold, lead, bismuth, thorium and uranium by 70-200 keV protons," Nuclear Instruments and Methods in Physics Research, B40/41, p. 116 (1989).

[50] H. Paul and J. Muhr, "Review of experimental cross sections for K-shell ionization by light ions," Physics Reprints (a review section of Physics Letters), 135, 2, p. 47 (1986).

[51] A.P. Jesus, T.M. Pinheiro, L.A. Niza, J.P. Ribeiro and J.S. Lopes, "L-shell x-ray production cross sections for PIXE analysis of elements from Ag to U," Nuclear Instruments and Methods in Physics Research, B15, p. 595 (1986).

[52] G. Basbas, W. Brandt, and R. Laubert, "Universal cross sections for K-shell ionization by heavy particles. I. Low particle velocities," Physical Review A, 7:3, p. 983 (1973).

[53] G. Basbas, W. Brandt, and R. Laubert, "Universal cross sections for K-shell ionization by heavy particles. II. Intermediate particle velocities," Physical Review A, 17:5, p. 1655 (1978).

[54] J.D. Garcia, R.J. Fortner, and T.M. Kavanagh, "Inner-shell vacancy production in ion-atom collisions," Reviews of Modern Physics, 45, p. 111 (1973).

[55] Ž. Šmit, "K-shell ECPSSR cross sections for analytical applications," Nuclear Instruments and Methods for Physics Research, B36, p. 254 (1989).

[56] H. Paul, "Test of various theories for K-shell ionization by protons," Zeitschrift für Physik D - Atoms, Molecules and Clusters 4, p. 249 (1987).

[57] M.S. Chen and B. Craseman, "Relativistic cross sections for atomic K- and L-shell ionization by protons, calculated from a Dirac-Hartree-Slater model," Atomic Data and Nuclear Data Tables, 33, p. 217 (1985).

[58] W. Reuter, A. Lurio, F. Cardone, and J. F. Ziegler, "Quantitative analysis of complex target by proton-induced x rays," Journal of Applied Physics, 46, p. 3194 (1975).

[59] I. Reid, Physics Department, University of Florida, private communication (1990).

[60] J.L. Campbell, W.J. Teesdale and J.-X. Wang, "Accuracy of thick-target micro-pixe analysis," Nuclear Instruments and Methods in Physics Research, B50, p. 189 (1989).

[61] J.H. Hubbell, Photon Cross Sections, Attenuation Coefficients and Energy Absorption Coefficients from 10 keV to 100 GeV, United States Department of Commerce Publication NSRD-NBS 29 (1969).

[62] A.M. Ferrari and E. Fairstein, "Nuclear preamplifiers and the pulse pile-up problem," Nuclear Instruments and Methods, 63, p. 218 (1968).

[63] C.H. Nowlin and J.L. Blankenship, "Elimination of undesirable undershoot in the operation and testing of nuclear pulse amplifiers," Review of Scientific Instruments, 36, p. 1830 (1965).

[64] J.B. Johnson, "Thermal agitation of electricity in conductors," Physical Review, Vol. 32, No. 1, p. 97 (1928).

[65] A.B. Gillespie, Signal, Noise and Resolution in Nuclear Counter Amplifiers, (McGraw-Hill Book Co., Inc., N.Y.), (1953).

[66] IEEE Std 301-1988, "IEEE Standard Test Procedure for Amplifiers and Preamplifiers used with Detectors of Ionizing Radiation."

[67] E. Fairstein, TC-200 Instruction Manual, Tennelec Instrument Company, Inc., Oak Rudge, Tenn. (1965).

[68] L.B. Robinson, "Reduction of baseline shift in pulse amplitude measurements," Review of Scientific Instruments, 32, p. 1057 (1961).

[69] J.W. Maas, "Investigation of ^{27}Al and ^{28}Si level schemes," Ph.D. Dissertation, Rijksuniverteit te Utrecht (1976).

[70] P.M. Endt and C. Van der Leun, "Energy levels of A = 21-44 nuclei (V)," Nuclear Physics, vol., A214, p. 202, (1973).

[71] I. Reid, University of Florida, Department of Physics, private communication (1990).

BIOGRAPHICAL SKETCH

Angelo M. Ferrari was born on August 30, 1934, in Gualeguaychú, province of Entre Ríos, Argentina. In March 1952, he began civil engineering studies at the National University of Buenos Aires. These studies were temporarily interrupted by military service and political instability which disrupted the normal functioning of the university for approximately one year. In 1956, he returned briefly to the National University of Buenos Aires, and in August of that year he was selected from a significant number of applicants to receive one of thirteen fully paid scholarships awarded by the Argentine National Atomic Energy Commission (CNEA) to pursue studies of physics at the recently organized Institute of Physics of San Carlos de Bariloche (now Balseiro Institute of Physics) in the province of Río Negro. This institute is a school of the National University of Cuyo and is fully funded by the CNEA. In June 1959, Ferrari completed the program at the institute and received a MS degree in physics.

In December 1959, he was awarded an International Atomic Energy Agency (IAEA) scholarship and a supplemental scholarship from the Argentine National Research Council to continue his training in the United States.

Ferrari spent two years in the United States during which he specialized in nuclear radiation detection and analysis instrumentation. He worked under Dr. D. Morken on instrumentation for detection of low-energy gamma-rays at the University of Rochester, Rochester, New York; under Dr. A.P. Sanders on instrumentation for calibration of radiation therapy systems at Duke University; Durham, North Carolina; under H. Lamond on design of analog-to-digital converters at North Carolina State College in Raleigh, North Carolina; and under C. Borkowski on air proportional counter technology at Oak Ridge National Laboratory, Oak Ridge, Tennessee. An air proportional counter insensitive to atmospheric humidity was developed during this period, for which Ferrari was awarded U.S. Patent No. 3,288,999.

In December 1961, Ferrari returned to Argentina and was appointed investigator at the Bariloche Atomic Center (a CNEA research installation) and instructor of nuclear instrumentation at the Balseiro Institute of Physics.

In January 1964, he was offered and accepted a position as a design engineer with the Tennelec Instrument Company of Oak Ridge, Tennessee, and returned to the United States as a permanent resident. In 1969, he became a citizen of the United States.

During the period of his employment with Tennelec, Ferrari designed the power supply for the TC200 linear amplifier. This was one of the first compact, high-efficiency, fully transistorized switching power supplies on the market. The TC200, designed by E. Fairstein, was the first commercially available nuclear research amplifier with gaussian pulse shaping. It was introduced in 1965 and was extremely successful commercially, with many thousand units sold world wide. Also in 1965, Ferrari designed the TC130 preamplifier. This was the first fully transistorized nuclear research preamplifier suitable for use with the large range of germanium detector sizes rapidly being introduced at the time. The TC130 introduced some design techniques that are still in use today in many low-noise pulse preamplifiers.

In 1968, after being promoted to vice president of engineering, Ferrari initiated the development of a full line of NIM instrumentation, which was completed in approximately one and a half years. This line included linear amplifiers, power supplies, biased amplifiers, single channel analyzers, analog-to-digital converters, etc.

Ferrari left Tennelec in 1971 to become a consulting engineer for Combustion Engineering. In 1973, he moved to Jacksonville, Florida as an independent manufacturer sales representative in the areas of nuclear and medical instrumentation.

In 1987, he decided to obtain a degree from a U.S. university and pursue an academic career. He was accepted to the graduate school of the University of Florida in the summer term of 1988. He expects to receive a Doctor of Philosophy degree in December 1991.

Ferrari is married to the former Raquel Santillán and has three children, Lucia, Mario, and Pablo.

I certify that I have read this study and that in my opinion it conforms to acceptable standards of scholarly presentation and is fully adequate, in scope and quality, as a dissertation for the degree of Doctor of Philosophy.

Samim Anghaie

Samim Anghaie, Chairman
Associate Professor of Nuclear
Engineering Sciences

I certify that I have read this study and that in my opinion it conforms to acceptable standards of scholarly presentation and is fully adequate, in scope and quality, as a dissertation for the degree of Doctor of Philosophy.

Reza

Reza Abbaschian
Professor of Materials Science
and Engineering

I certify that I have read this study and that in my opinion it conforms to acceptable standards of scholarly presentation and is fully adequate, in scope and quality, as a dissertation for the degree of Doctor of Philosophy.

William H. Ellis

William H. Ellis
Associate Professor of Nuclear
Engineering Sciences

I certify that I have read this study and that in my opinion it conforms to acceptable standards of scholarly presentation and is fully adequate, in scope and quality, as a dissertation for the degree of Doctor of Philosophy.

Alan M. Jacobs

Alan M. Jacobs
Professor of Nuclear Engineering
Sciences

I certify that I have read this study and that in my opinion it conforms to acceptable standards of scholarly presentation and is fully adequate, in scope and quality, as a dissertation for the degree of Doctor of Philosophy.

Hendrik J. Monkhorst
Professor of Physics

I certify that I have read this study and that in my opinion it conforms to acceptable standards of scholarly presentation and is fully adequate, in scope and quality, as a dissertation for the degree of Doctor of Philosophy.

M Luis Muga

M. Luis Muga
Professor of Chemistry

This dissertation was submitted to the Graduate Faculty of the College of Engineering and to the the Graduate School and was accepted as partial fulfillment of the requirements for the degree of Doctor of Philosophy.

December 1991

Hubert A. Bevis

for Winfred M. Phillips
Dean, College of Engineering

Madelyn M. Lockhart
Dean, Graduate School

UNIVERSITY OF FLORIDA
3 1262 08285 457 0